



Attribution–NoDerivs 2.0 KOREA

You are free to :

- **Share** — copy and redistribute the material in any medium or format
- for any purpose, even commercially.

Under the following terms :



Attribution — You must give [appropriate credit](#), provide a link to the license, and [indicate if changes were made](#). You may do so in any reasonable manner, but not in any way that suggests the licensor endorses you or your use.



NoDerivatives — If you [remix, transform, or build upon](#) the material, you may not distribute the modified material.

You do not have to comply with the license for elements of the material in the public domain or where your use is permitted by an applicable exception or limitation.

This is a human-readable summary of (and not a substitute for) the [license](#).

[Disclaimer](#) 

공학석사학위논문

Transient Flow Analysis and Static Bench Measurements for an Active Trailing-Edge Flap

회전익기 진동제어를 위한 능동뒷전 플랩의

비정상 유동해석과 테스트 벤치를 이용한

시험

2016년 2월

서울대학교 대학원

기계항공공학부

Umberto Visconti

Transient Flow Analysis and Static Bench Measurements for an Active Trailing-Edge Flap

회전익기 진동제어를 위한 능동뒷전 플랩의 비정상 유동해석과 테스트 벤치를 이용한 시험

지도교수 신 상 준

이 논문을 공학석사 학위논문으로 제출함

2016년 2월

서울대학교 대학원

기계항공공학부

Umberto Visconti

Umberto Visconti의 석사학위논문을 인준함

2016년 2월

위원장 이수근 (인)
부위원장 신상준 (인)
위원 이관홍 (인)

Abstract

In this dissertation, several analyses over SNUF (Seoul National University Flap), a small-scaled prototype equipped with an active trailing edge flap, were conducted in order to achieve vibratory load reduction in the rotor system. The device consists of a piezoelectric actuator driven flap which generates secondary vibrations aimed at dampening the primary disturbances. Predictions of the hinge moment coefficient were retrieved through CFD (computational fluid dynamics) analyses in order to verify the capability of the chosen actuator to ensure a smooth and efficient displacement of the flap and therefore the achievement of the designated objective. The results showed good compromises between the actuator characteristics and the loads generated over the flap surface. Furthermore, a multibody dynamic analysis was implemented with DYMORE to obtain a holistic view of the forces and the displacements acting within the device when external aerodynamic loads and centrifugal force occur. Outcomes from the code were validated with theory formulation and thus are considered a reliable description of the dynamics of the system. In addition to that, a pulling test was conducted so as to observe any likely decrease in the deflection range once the centrifugal force acts in a direction perpendicular to the flap angular displacement. Although the ultimate load applied does not coincide with final objective, the limited shrinkage of the deflection span suggests a definitive result still satisfying the requirements.

Keywords: Active Trailing-edge Flap (ATF), piezoelectric actuator,
vibration control, active rotor blade

Student number: 2014-22147

Table of contents

List of figures	IV
List of tables	VII
I. Introduction	1
1.1 Backgrounds and motivation	1
1.2 Vibrations suppression methods	2
1.3 Previous studies	6
1.4 Objectives and overview of the dissertation	7
II. Theoretical background	10
2.1 Present research review	10
2.2 Computational domain meshing	11
2.3 Solver	15
2.4 Steady case	17

2.5 Transient case	20
2.6 DYMORE model	22
2.7 Micromechanics to estimate the properties of the composite materials used	25
2.8 Model features	27
2.9 Pulling test implementation	31
III. Numerical and experimental results	33
3.1 Steady state results	33
3.2 Transient state results	43
3.3 DYMORE centrifugal load analysis	51
3.4 DYMORE flap deflection analysis	54
3.5 DYMORE aerodynamic loads analysis	56

3.6 Pulling test results	62
IV. Conclusion and future works	65
4.1 Conclusion	65
4.2 Future works	66
Reference	68
국문초록	71

List of Figures

Figure 1. 1 Aerodynamic issues in forward flight-----	2
Figure 1. 2 SARIB system -----	3
Figure 1. 3 ACSR application to Agusta-Westland-----	4
Figure 1. 4 Individual blade control-----	5
Figure 1. 5 Active trailing edge flap -----	6
Figure 1. 6 Previous version of the mesh in use -----	9
Figure 2. 1 Mechanism in use. -----	11
Figure 2. 2 Mesh used by Li et al. (2011)-----	13
Figure 2. 3 Detail of the used mesh. -----	14
Figure 2. 4 Drawing of the mechanism-----	24
Figure 2. 5 DYMORE schematic model -----	24
Figure 2. 6 Relationship among the block force, input voltage, and stroke -----	28
Figure 2. 7 Hinge moment evolution -----	30
Figure 2. 8 Pulling test test-bed-----	32
Figure 3.1 Drag coefficient with no flap deflection-----	34
Figure 3.2 Lift coefficient with no flap deflection -----	34
Figure 3.3 Moment coefficient with no flap deflection. -----	35
Figure 3.4 Drag coefficient comparison-----	36
Figure 3.5 Lift coefficient comparison -----	37

Figure 3.6 Moment coefficient comparison -----	37
Figure 3.7 Refined mesh-coarse mesh comparison for drag -----	39
Figure 3.8 Refined mesh-coarse mesh comparison for lift -----	39
Figure 3.9 Refined mesh-coarse mesh comparison for moment-----	40
Figure 3.10 Absolute difference between the coarse and refined mesh---	41
Figure 3.11 Hinge moment trend according to Walz and Chopra-----	42
Figure 3.12 Hinge moment comparison with 10° flap deflection -----	43
Figure 3.13 Drag coefficient at 2 Hz flap actuation-----	44
Figure 3.14 Lift coefficient at 2 Hz flap actuation -----	44
Figure 3.15 Moment coefficient at 2 Hz flap actuation -----	45
Figure 3.16 Drag coefficient at 20 Hz flap actuation -----	45
Figure 3.17 Lift coefficient at 20 Hz flap actuation-----	46
Figure 3.18 Moment coefficient at 20 Hz flap actuation.-----	46
Figure 3.19 Drag coefficient at 65 Hz flap actuation -----	47
Figure 3.20 Lift coefficient at 65 Hz flap actuation.-----	47
Figure 3.21 Moment coefficient at 65 Hz flap actuation-----	48
Figure 3.22 Hinge moment coefficient at 2 Hz flap actuation -----	49
Figure 3.23 Hinge moment coefficient at 20 Hz flap actuation.-----	50
Figure 3.24 Hinge moment coefficient at 65 Hz flap actuation -----	50
Figure 3.25 Flap deflection as a function of the moment arm length (predicted) -----	51

Figure 3.26 Internal forces at the blade root.-----	53
Figure 3.27 Internal forces at the blade tip -----	54
Figure 3.28 Flap deflection at 2 Hz actuation-----	55
Figure 3.29 Flap deflection at 20 Hz actuation. -----	55
Figure 3.30 Flap deflection at 65 Hz actuation. -----	56
Figure 3.31 Total airloads over a single blade -----	57
Figure 3.32 Airloads at the blade root -----	58
Figure 3.33 Airloads at the blade tip. -----	59
Figure 3.34 Flap deflection at 2 Hz with airloads -----	60
Figure 3.35 Flap deflection at 20 Hz with airloads -----	60
Figure 3.36 Flap deflection at 65 Hz with airloads -----	61
Figure 3.37. Internal forces at the blade root in aerodynamic conditions -----	62
Figure 3.38 Flap deflection under the dead loads -----	63
Figure 3.39 Flap deflection under the dead loads [detail] -----	64

List of Tables

Table 2.1 Material properties-----	27
Table 2.2 Chebyshev coefficients -----	31
Table 3.1 Aerodynamic analysis conditions-----	33

I. INTRODUCTION

1.1 Backgrounds and motivation

Helicopters constitute a versatile means of transportation able to achieve tasks otherwise difficult to accomplish with fixed-wing vehicles such as vertical take-off and hovering. In spite of these unique capabilities, they also encounter different issues, especially in fast forward and descent flight conditions. Among the different causes, the absence of a symmetry axis results in a different flow speed between the advancing and the retreating side of the rotor, as in Fig. 1.1, whereas the perturbations which arise due to the interference among the overlapping blade wakes generate a relevant amount of noise and vibrations [1]. As a consequence, anytime comfort is a major aspect of the mission being conducted, such as VIP flights or non-urgent medical transportation, the proximity of the passengers to the vibrations source and the coincidence of the frequency span generated with human perceivable range negatively affect the flight experience. [2]

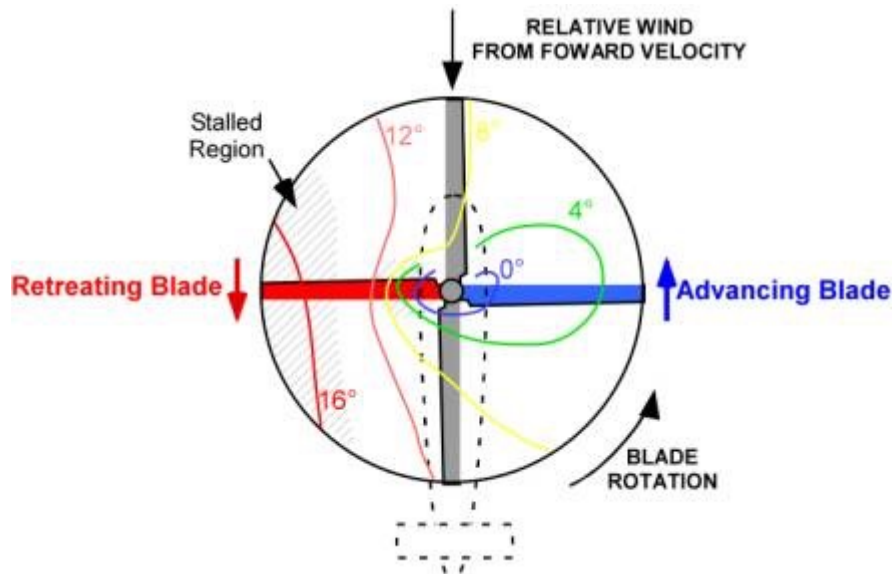


Figure 1.1 Aerodynamic issues in forward flight

1.2 Vibrations suppression methods

The rotor induced vibrations, other than being a nuisance, also pose a harm to structural integrity of the components which may have their lifespan shortened due to the continuous stress they endure [3]. So far, the traditional approach to the issue was represented by several devices placed on the hub and aimed at dampening the transmission of vibrations from the rotor to the fuselage. The most common concept, denominated DAVI, consists of a mass, added to the shaft, whose oscillating movement is amplified thanks to interconnected pins [4] so as to be able to counteract and eliminate external excitations. Further developments include ARIS system and SARIB[®] [2], depicted in Fig. 1.2, which still exploit, in a different way, hydraulic or mechanical system to implement vibration load dampening. All the above solutions, despite succeeding in their goals, showed major disadvantages

such as increased drag, due to the system bulkiness and weight, and single frequency tuning which implies that all the other vibrations flow untouched. In fact, aside from 1/rev frequency, the remaining pN/rev harmonics, where N is the number of blades and p an integer, are not cancelled out but transmitted undampened to the fuselage [5].



Figure 1.2 SARIB system

On the other hand, due to above mentioned limitations, the concept of an active control is increasing its popularity due to a higher adaptability and greater efficiency in reducing the vibrations generated. Active methods are usually classified into two groups: one aims at attenuating the vibration directly in the fuselage while the second attempts to prevent it at the origin.

The former, represented in Fig. 1.3, is denominated Active Control of Structural Response (ACSR) and it is enacted placing vibration sensors in key locations of the fuselage [6]. Once the amount of vibration is sensed, the device will instruct actuators located throughout the structure to generate a specifically designed vibration necessary to alleviate the primary disturbance.



Figure 1.3 ACSR application to Agusta-Westland

The latter instead, focuses its attention on the rotor and it is further divided in two categories. The Higher Harmonic Control (HHC) still takes advantage of sensors distributed on the frame to register the vibrations encountered but then makes use of the non-rotating swashplate to input higher harmonics on the rotor blades; despite proving to be successful, widespread use of this solution is not possible due to weight penalties and the high actuation power required.

On the other hand, Individual Blade Control (IBC), shown in Fig. 1.4, implementation proved to be more successful. The idea still consists of secondary loads generated on purpose to compensate the primary source of vibration; while originally electro-hydraulic systems were exploited, the use of piezo-electric actuators [7] has become more and more common. The major advantage is the possibility to excite the blade at any frequency and thus, be able to erase any vibration, regardless its mode. At first, pitch actuation was applied at the blade root (off-blade actuation) as a substitution of the conventional control rods connected to the swashplate.

After that, thanks to further developments of piezoelectric materials, fibers of the latter were embedded in the blade itself so as to create a morphing structure, denominated Active Twist Rotor (ATR), able to twist along the blade span. Despite the good results achieved during experimentation, the high power required for its implementation plunged its diffusion. Finally, a third solution with low energy requirements and good outputs was conceived: the Active Controlled trailing-edge Flap (ACF). This implementation case consists of a stiff blade equipped with a moving flap driven by a piezoelectric actuator which modifies the aerodynamic of the blade and showed effective vibrations reduction, as portrayed in Fig. 1.5.

Generally, the system includes data acquisition along power transmission; once the sensors report the state of rotor blade, the incoming values are analyzed and a signal is transmitted to the actuators driving the flap which will react in the best possible way to eliminate the produced vibration.

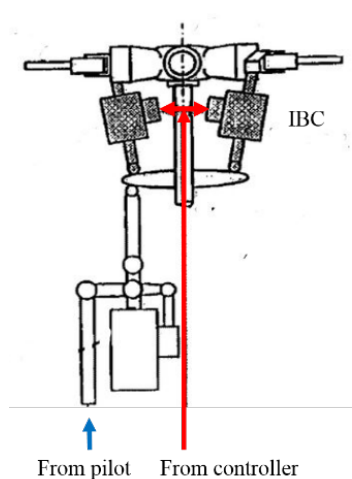


Figure 1.4 Individual blade control

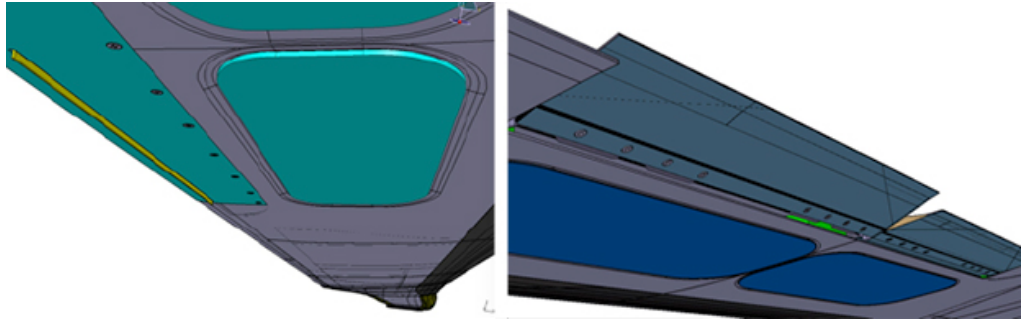


Figure 1.5 Active trailing edge flap (Agusta-Westland)

1.3 Previous studies

ACF is so far one of the most successful solutions adopted for vibrations suppression; a number of different researches have already been conducted, both on small and full scale, and the results obtained proved to be satisfactory. Walz and Chopra [8] conceived a bimorph flap actuation system to be placed within the fixed frame which would deflect and thus move the flap it is connected to. Although no rotating test was conducted, the mechanism in use shows great versatility and, what is more, room for improvement once design is perfected. Konstanzer, Enenkl, Aubourg and Cranga [2] instead applied the active trailing edge flap to a full scale rotor and measured the reduction in vibration caused by 4/rev hub loads. Three identical flap units, driven by two piezo-ceramic actuator each, were installed on all the rotor four blades and sensors were placed to monitor different parameters; actuation of the device on an experimental flight contributed to an overall reduction of vibrations which amounts to 90% of its original value. In conclusion, ACF is a promising technology which already demonstrated its

capabilities and versatility and it is apt to be adopted for a wider range of applications in future.

1.4 Objectives and overview of the dissertation

In spite of the different efforts to dampen the vibrations generated during flight, we are still far from a complete reduction of the disturbances which occur due to the complex dynamics which characterize helicopters. This happened due to the incapability of passive methods to adapt to the different flight conditions which may raise during operations and, as far as active methods are concerned, to the intrinsic difficulties typical of a closed loop actuation which requires perfect feedback to customize the response. On the other hand, the introduction of piezo electric actuators outstandingly improved the results obtained; in fact, the reduced weight coupled with high power density proved to be extremely useful in components such as rotors, whose stability is very sensitive to any additional load. What is more, these devices enable a simplification of the layout of the whole system, whose complexity is still one of the major drawbacks in the full exploitation of active methods.

As consequence, the development of a small-scaled blade equipped with a trailing edge active flap, denominated SNUF, driven by a piezoceramic actuator was conducted in order to be able to dampen the vibratory load. The final implementation will consist of a two blade rotor, each of those equipped with a movable surface placed at 75% of the whole length blade and driven by a CEDRAT actuator.

This dissertation concerning the design improvements is articulated in three fundamental points:

- hinge moment estimation
- implementation of a multibody analysis
- conduction of a pulling test

CFD analysis consists of meshing the chosen NACA 0015 airfoil surroundings in order to simulate the airflow the blade would encounter and to estimate the airloads generated on the surfaces. Unlike the previous design shown in Fig. 1.6, the flap is kept detached from the airfoil main body. Specifically, hinge moment coefficient is the value we mostly focus on so as to evaluate the amount of the pressure distribution over the flap which could obstacle a smooth actuation of the flap.

Multibody dynamic analysis is implemented thanks to the capabilities of DYMORE which couples the structural properties of blade and mechanism link with the external solicitations being the centrifugal force and the aerodynamic loads

Pulling test includes the design and manufacturing of a specifically conceived test bed aimed at the actuation of the flap in a vertical position. This, allows the application on the flap of different sets of weights which simulate the loads generated when the blade rotates; once the flap is actuated, the resulting deflection are measured in order to observe the decrease in deflection range compared to the unloaded situation.

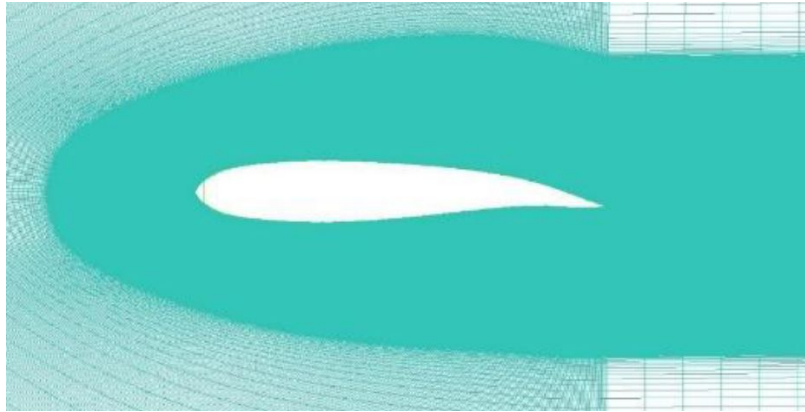


Figure 1.6 Previous version of the mesh in use

II. THEORETICAL BACKGROUND

2.1 Present research review

In the design of the active trailing edge flap, static bench test was thought to be the most important step to be completed during the analysis process of the mechanism but once the first version of the test bed was manufactured, the flap deflection could not meet the requirements [9] probably due to unexpected friction in the link mechanism. The issue was approached increasing the number of actuators which would drive the flap in order to provide the flap with a higher force. Unfortunately, the accumulation of actuators did not concur to a more efficient motion as other factors such as interaction between the actuators and misalignment came into play and reduced the overall capability of the actuators. As a consequence, instead of stacking a higher number of actuators which would affect the overall weight without wreaking benefits on the deflection requirements, the APA 200L piezoelectric actuator in use was substituted.

More importantly, whereas previously blade structural analysis had been completed before choosing the actuator, thus restraining the choice for actuators selection and layout, the implementation flow was inverted and an actuator which could deflect the flap in the whole range required was selected first and then the encompassing blade design, as visible in Fig. 2.1, was conducted.

As a consequence, a new actuator was selected [10], specifically APA 1000L, in order to obtain a sufficient deflection during non-rotating test which would be inevitably reduced [11] once aerodynamics in the whirl tower is added. Also, static load analyses were implemented on the actuator to verify whether it could withstand centrifugal forces and blade design was renewed. Increased size of the newly-selected actuator meant

an increase in length and width of the blade and built-in twist was applied throughout the whole length to enhance structural integrity.

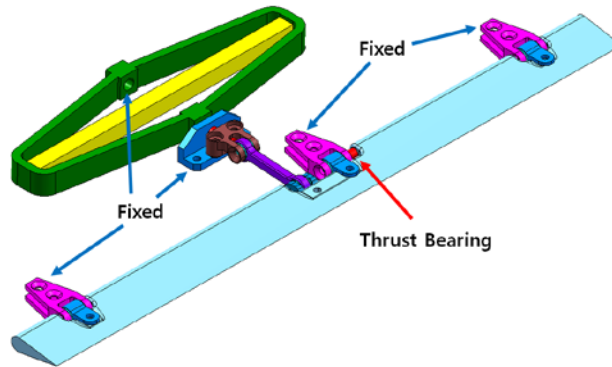


Figure 2.1 Mechanism in use

2.2 Computational domain meshing

A momentous aspect in the design of the ATF is the estimation of the hinge moment generated by external forces. In fact, during the blade rotation a distributed load generates on the flap surface and obstacles the smooth oscillation of the device; thus, the vibrations suppression will only achieved once the mechanism is able to counteract and overcome the aerodynamic load insisting on the flap.

The NACA 0015 airfoil geometry was split into two blocks, as already achieved by Li et al. [12] in Fig. 2.2, to adjust to the requirements for calculation in transient mode; a main block, constituting 80% of the whole length, is kept still and a detached flap, represented in Fig. 2.3, instead deflects according to the imposed function. Slotted flaps, as the configuration is denominated [13] when a gap exists between the main portion and the deflected flap, increase the effectiveness of the airfoil thanks to an increase in camber and chord. Nonetheless, in spite of the

relevant gain in aerodynamic performance, the complex geometry of the layout does not allow a reliable prediction of pressure loads and aerodynamic coefficients are either retrieved experimentally or through CFD simulation.

As in our case experimental measurements were not available, estimation of the load acting on the airfoil was implemented through a computational fluid dynamics analysis: ICEM was chosen as the meshing software and ANSYS FLUENT as the solver. The above analysis was articulated in two different stages: first, static measurements were conducted on the flap deflected by 10° , an angle higher than the expected operating range, to include a safety factor in the sizing of the mechanism link. Secondly, a transient analysis, where the flap actuation frequency spanned from 0 Hz to 65 Hz (2/rev), was enacted to retrieve realistic values of the aerodynamics coefficients occurring during the ATF utilization.

C-shaped computational domain was chosen over O-shaped domain as the sharp trailing edge would force the adjacent triangular elements to have $180 - \frac{\alpha}{2}$ angles, α being the flap internal angle; in such case the enclosed edge is preferred to run parallel to the wall, as it would happen with a C-shaped domain, rather than perpendicular, as in the O-shaped case [14]. What is more, C-shape inherent ability to capture wake makes it a preferential choice when aerodynamic coefficients are needed; still for wake issues, the domain size was set roughly 20 times the airfoil chord to prevent boundaries from influencing the flow in the vicinity of the airfoil [15]. Although the simple geometry does not require a complex meshing layout, triangular unstructured mesh was selected as the most flexible and suitable in case of dynamic mesh, where remeshing and smoothing processes are applied during the computation to maintain high cell quality [16]. In addition to that, hexahedral elements were placed along the airfoil

to better capture and define the boundary layer and to constitute a medium between the physical walls and the triangular mesh. The latter aspect is also the reason why hexahedral cells are present along the outer walls of the domain; also, without this precaution, negative volume issues are bound to occur during the flap actuation. Given that accuracy is only required in the surroundings of the airfoil, a coarse mesh was drawn in the majority of the domain and only refined in proximity of the walls. The total number of elements comprises 8506 triangular cells and 1810 hexahedral prisms arranged in 5 layers; in fact, a higher number of layers would have filled the gap between the airfoil main block and the flap, thus decreasing the quality of computation in a fundamental region for the objectives of the analysis.

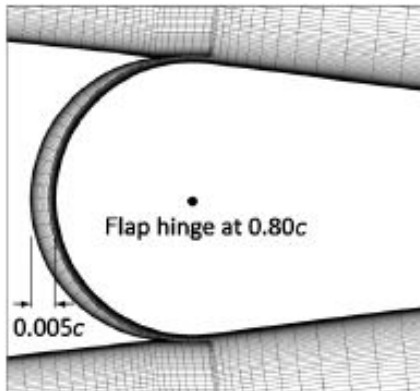


Figure 2.2 Mesh used by Li et al. (2011)

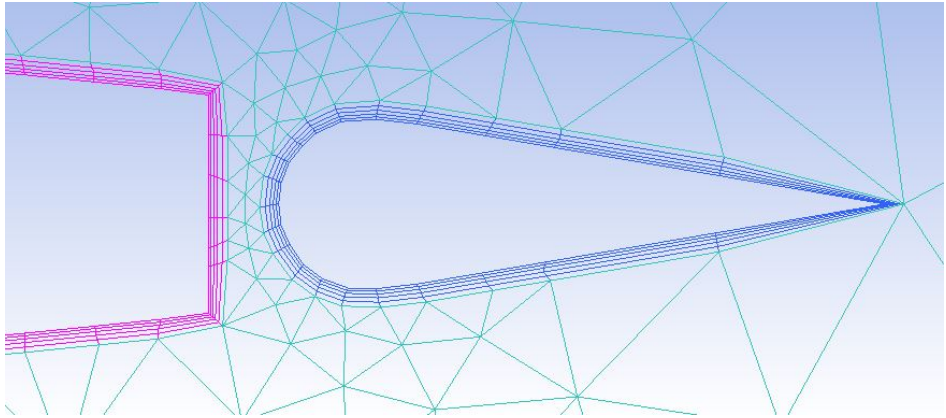


Figure 2.3 Detail of the used mesh

The selected meshing approach, denominated Patch Independent, takes advantage of the Octree method, a top-down approach where the mesh is first generated and then made conformal to the present geometry. This choice allows to start from an extremely coarse web and gradually refine the grid only in the regions requiring a more detailed definition, in our case the flap area and the gap between the latter and the main block of the airfoil [17]. On the contrary, the other available approaches such as Autoblock or Patch Dependent, with the same amount of refinement in the areas of interest, would have generated an excessive number of elements in the whole computational domain. To obtain even and smooth hexahedral elements layers, the quality of the overall mesh has to be improved through alternate cycles of simple and Laplace smoothing, the latter computing the average position of the surrounding nodes to generate a new position of the node of interest. A further step to increase quality of triangular mesh takes advantage of Delaunay circle test: when two cells share a face and the circumcircle of one of the two also encompasses the unshared vertex of the other cell, then faces are swapped [18].

2.3 Solver

ANSYS FLUENT is the solver selected to extract hinge moment and other data from the considered model. Mass, momentum and energy equations are the conservation equations solved by ANSYS FLUENT and involved in the flow which characterizes our model.

Continuity equation in integral form is defined as

$$\frac{\partial}{\partial t} \int_V \rho dV + \oint \rho \mathbf{v} \cdot d\mathbf{A} = 0 \quad (1)$$

Given that no mass is added to the continuous phase, the right term is set to 0.

Momentum equation in integral form is instead defined as

$$\begin{aligned} \frac{\partial}{\partial t} \int_V \rho u dV + \oint [\rho \mathbf{v} u + p \hat{i} - \tau_{xi}] \cdot d\mathbf{A} &= 0 \\ \frac{\partial}{\partial t} \int_V \rho v dV + \oint [\rho \mathbf{v} v + p \hat{j} - \tau_{yi}] \cdot d\mathbf{A} &= 0 \end{aligned} \quad (2)$$

As gravity does not contribute significantly and no external force is applied to our model, no term on the right side of the equation is considered in the computation. On the other hand, due to viscosity, shear stress is part of the flow physics and it is described through the stress tensor as follows

$$\bar{\bar{\tau}} = \mu \left[(\nabla \bar{\mathbf{v}} + \nabla \bar{\mathbf{v}}^T) - \frac{2}{3} \nabla \cdot \bar{\mathbf{v}} \mathbf{I} \right] \quad (3)$$

The choice of ideal compressible fluid case implies the addition of density as a further variable in the model, which means an additional equation, energy conservation equation, is added to the model description:

$$\frac{\partial}{\partial t} \int_V \rho E dV + \oint [\rho \mathbf{v} E + p \mathbf{v} - \tau_{ij} v_j] \cdot d\mathbf{A} = 0 \quad (4)$$

where no heat flux or work done by body forces is considered.

The viscosity model which best fits the situation is the Spalart-Allmaras model [19] which derives from the Boussinesq approach and does not require a burdensome computation when turbulent viscosity is investigated.

$$\begin{aligned} \frac{\partial}{\partial t}(\rho\tilde{\nu}) + \frac{\partial}{\partial x_i}(\rho\tilde{\nu}u_i) = G_\nu + \dots \\ \dots + \frac{1}{\sigma_{\tilde{\nu}}} \left[\frac{\partial}{\partial x_j} \left\{ (\mu + \rho\tilde{\nu}) \frac{\partial \tilde{\nu}}{\partial x_j} \right\} + C_{b2\rho} \left(\frac{\partial \tilde{\nu}}{\partial x_j} \right)^2 \right] - Y_\nu + S_{\tilde{\nu}} \end{aligned} \quad (5)$$

This model, usually exploited for low Reynolds numbers, consists of a single equation describing the transport of kinematic viscosity and it is defined by eight constants.

As mentioned, the flow is described as compressible and therefore it is characterized by total pressure and total temperature as follows

$$\begin{aligned} \frac{p_0}{p} &= \left(1 + \frac{\gamma-1}{2} M^2 \right)^{\frac{\gamma}{\gamma-1}} \\ \frac{T_0}{T} &= 1 + \frac{\gamma-1}{2} M^2 \end{aligned} \quad (6)$$

where pressure specific heat is assumed constant given that the model does not encounter notable temperature variations.

Density is thus computed:

$$\rho = \frac{P_{op} + P}{\frac{R}{M_w} T} \quad (7)$$

The external boundary of the C shaped computational domain is divided in a forward facing half and in a rear facing half. Both are characterized by pressure far field boundary conditions, where the stream is modeled at infinity and the flow direction is changed according to the angle of attack desired for the airfoil. While gauge pressure and temperature are kept at standard conditions, the Mach number is modified to simulate the velocity

of the airfoil section where the active flap is placed. The airfoil main block and the flap are instead considered as wall, which implies non penetrability of mass, momentum and energy flow

$$\mathbf{u} \cdot \mathbf{n} = \nu^B \cdot \mathbf{n} \quad (8)$$

Also, due to viscosity, no-slip condition is implemented and thus, the fluid sticks to the wall.

2.4 Steady case

One of the most important aspects of Navier-Stokes equations is the non-linearity which obstacles any possibility to solve them analytically and forces the application of a computational scheme to the discretized form of the equations into account. During the solution of the problem, the default ANSYS FLUENT process consists of computation of a scalar per each cell and storage of the cell center value; nonetheless, convective terms require the presence of cell face values. As a consequence the generic value at cell face is computed as follows

$$\Phi_f = \Phi + \nabla \Phi \cdot \vec{r} \quad (9)$$

starting from the generic value at cell center.

This approach is especially useful as our computation requires at least second order accuracy for both diffusive and convective terms; while the former does not pose any problem, the latter requires a specific approach which makes use of Taylor series expansion of cell centered value about the cell centroid. Second order accuracy is not strictly necessary in situations where the flow is aligned with the mesh, as a hexahedral mesh, but the choice of a triangular grid makes the use of second order upwind necessary. Its general formulation is as stated

$$\Phi_{f,SOU} = \Phi + \nabla \Phi \cdot \vec{r} \quad (10)$$

Gradient is computed using the Least Squares Cell-Based Gradient evaluation [20] which assumes the solution varies linearly between two cell centers

$$(\nabla\Phi)_{cell0} \cdot \Delta r_1 = (\Phi_{cell1} - \Phi_{cell0}) \quad (11)$$

The overdetermined system which arises from writing an equation for each cell surrounding the first cell is then solved exploiting the Gram-Schmidt process; the resulting weights are then applied to the scalar difference vector.

Discretization of momentum exploits the procedure applied to the generic scalar transport equation, where velocity components u and v , respectively along x and y direction, as we are in a 2D geometry, substitute the generic quantity.

$$\begin{aligned} a_p u &= \sum_{nb} a_{nb} u_{nb} + \sum p_f A \cdot \hat{i} + S \\ a_p v &= \sum_{nb} a_{nb} v_{nb} + \sum p_f A \cdot \hat{j} + S \end{aligned} \quad (12)$$

Discretization of continuity equation is accomplished using the mass flux through the cell face

$$\sum_f^{N_{faces}} J_f A_f = 0 \quad (13)$$

A combination between continuity equation and definition of mass flux is also exploited as a further condition exploited to describe and solve the flow problem into account. The SIMPLE-Consistent scheme (SIMPLEC) [21] applied calculates the new mass flux with a correction applied

$$J_f = J_f^* + d_f (p'_{c0} - p'_{c1}) \quad (14)$$

where coefficient d_f is defined as a function of momentum equation linearized coefficients

$$d_f = \sqrt{a_p - \sum_{nb} a_{nb}} \quad (15)$$

to improve convergence.

A further method to improve convergence during the problem solving is the use of the under relaxation factor which aims at reducing the variation of the generic scalar between one iteration and the following.

$$\Phi = \Phi_{old} + \alpha \Delta \Phi \quad (16)$$

The adjusted value will be then between $\Phi_{i,j}^k$ and $\Phi_{i,j}^{k+1}$.

Although Navier-Stokes equations do not present analytical solution, we can exploit theory to obtain an estimation of the values we will retrieve. This especially happens with hinge moment, where, along with CFD analysis, the algorithm formulated by Walz and Chopra [8] proves to be helpful: nonetheless, as it was originally conceived for a three-dimensional case, we had to simplify it to our two-dimensional model where no loss is considered.

Section hinge moment was defined as:

$$h = \frac{1}{2} \rho (\Omega r)^2 c_f^2 C_h \quad (17)$$

If integrated spanwise it results:

$$H = \int_{R_1}^{R_2} h dr = \int_{R_1}^{R_2} \frac{1}{2} (\Omega r)^2 c_f^2 C_h dr = \frac{1}{2} \rho (\Omega c_f)^2 C_h \frac{1}{3} (R_2^3 - R_1^3) \quad (18)$$

The variables present in the latter equation only depend on geometrical data or environmental conditions; hinge moment coefficient instead has to be defined as the linear combination of lift coefficient and flap deflection variations:

$$C_h = C_l \frac{\partial C_h}{\partial C_l} + \delta \frac{\partial C_h}{\partial C_\delta} = C_{l_\alpha} \alpha_{eff} \frac{\partial C_h}{\partial C_l} + \delta \frac{\partial C_h}{\partial C_\delta} \quad (19)$$

The variation of hinge moment coefficient with respect of the lift

coefficient and the deflection angle can be extracted, as a function of the ratio between airfoil chord and flap chord, as in Abbot and Doenhoff [12].

$$\begin{aligned}
\frac{\partial C_h}{\partial C_l} &= -0.01018 - 0.5494 \left(\frac{c_f}{c} \right) + 1.028 \left(\frac{c_f}{c} \right)^2 + \dots \\
&\dots - 0.9934 \left(\frac{c_f}{c} \right)^3 + 0.2270 \left(\frac{c_f}{c} \right)^4 \\
\frac{\partial C_h}{\partial \delta} &= -0.8469 + 0.9833 \left(\frac{c_f}{c} \right) - 0.07663 \left(\frac{c_f}{c} \right)^2 + \dots \\
&\dots + 0.2567 \left(\frac{c_f}{c} \right)^3 - 0.3205 \left(\frac{c_f}{c} \right)^4
\end{aligned} \tag{20}$$

As a consequence, the hinge moment coefficient can be plotted choosing the angle of attack and the flap deflection angle as parameters.

2.5 Transient case

Along with steady case, a transient simulation was also formulated. This consists of the flap oscillation according to an imposed sinusoidal function where frequency and deflection angle are specified by the user; with respect to the static phase, two major differences can be identified: dynamic mesh and choice of the solver.

As mentioned, during the simulation the flap moves symmetrically in the computational domain and, as a consequence, the surrounding cells warp and nodes move. This process, which may create high instabilities in the computation and unrealistic results [22], only involves triangular elements whereas hexahedral cells will only move without any modification in their shape.

Smoothing action contributes to re-establish the mesh equilibrium state which existed before the motion; specifically, the chosen spring-based

smoothing method works as the node displacement due to the imposed motion created a proportional Hook force

$$\vec{F}_i = \sum_j^{n_i} k_{ij} (\Delta \vec{x}_j - \Delta \vec{x}_i) \quad (21)$$

where the terms in the parentheses refer to the displacement of node i and j respectively. The equilibrium is reached once the net force over a node is null; the iterative equation which represents the summation of all the forces acting on the node results as follows:

$$\Delta \vec{x}_i^{m+1} = \frac{\sum_j^{n_i} k_{ij} \Delta \vec{x}_j^m}{\sum_j^{n_i} k_{ij}} \quad (22)$$

The retrieved displacement indicates the new position of the node.

Along with smoothing process, ANSYS FLUENT also includes a remeshing method which is applied anytime the smoothing iteration deteriorates the original mesh in terms of skewness and quality. This is likely especially when the imposed movement is big compared to grid size as our case where flap trailing edge displacement amounts to 0.041 m while triangular mesh size is as small as 0.0008 m. As a matter of fact, once this option is selected, the user is able to define the maximum and minimum value within which the remeshed elements have to fit in order to be accepted.

Both smoothing and remeshing processes are applied to the fluid region of our domain and the chosen “zone parameters” replicate similar values to the original ones, specifically: 0.0008 m as the minimum length scale, 0.1 m as the maximum length scale and 0.7 as the maximum skewness. A rigid body movement is instead selected for flap and surrounding hexahedral elements, where a sinusoidal function whose gravity center is located at the flap hinge (0.11442 m), is chosen as the user defined function to impose.

Along with dynamic meshes, the other major discrepancy between transient analysis steady state one is the algorithm used in the solver. Pressure-Implicit with Splitting of Operators (PISO) [23] still belongs to the SIMPLE family of algorithms exploited in the steady case but performs two further corrections every time new velocities are calculated. Neighbor correction is also defined as a momentum correction given that the calculations required for SIMPLEC algorithm are executed in the pressure-correction equation so that in few loops the velocity values obtained will better satisfy the continuity and momentum equation. The skewness correction instead, enables easier convergence for highly distorted meshes where the relationship between correction of mass flux and pressure difference correction is not accurate and thus requires more iterative cycles to compute the pressure-correction gradient to be used to calculate mass flux.

2.6 DYMORE model

The fluid dynamics analysis is not sufficient to confirm that the whole mechanism, represented in Fig. 2.4, would work properly instead, aerodynamic loads have to be coupled with structural properties and the layout to verify no major displacements or distortions would occur in the rotating environment.

DYMORE is an open-source finite element analysis tool for non-linear elastic multibody systems developed by Prof. O. Bachau at Georgia Institute of Technology. The elements available in the program include, among the others, beams, rigid bodies and a variety of joints and constraints. In the code, static analysis is first applied in order to solve all the motion equation relative to the system in the case where time derivatives are set to zero, once this stage is completed, the deformed

configuration is computed considering the static load applied. The eigenvalues and eigenvectors which result from the analysis constitute the product of the linearization of the dynamic equations of motion.

The joints exploited in the analysis include the revolute joint, where the two elements connected are only allowed to rotate about a specific axis and forbidden to displace in any direction, and prismatic joint where no rotation is allowed and relative displacement only proceeds along a given axis. Revolute joints are included in the push rod mechanism where the linear motion of the actuator has to be converted in the angular displacement of the flap; the prismatic joint, instead, simulates the contraction and dilation of the piezostack actuator at the base of the link mechanism. Two constraints per each blade are used in the model: one is a zero degree of freedom constraint applied at the root of a beam while the second constraint does not have a direct correspondence in the real model but it is only used to grant a 90 degrees intersection between two rigid bodies in the link mechanism. The blade is composed of four different beams: the first and last section will host the fiberglass roving which runs in the front part, chord-wise, of the blade, the second and third block will instead encompass the titanium block designed to hold the actuator. An associated rigid body is exploited to link the blade with the driving mechanism; the said body is connected on the other side with the prismatic joint pushing a set of two beams interconnected thanks to a revolute joint. The components are linked, through a further revolute joint, to a combination of two rigid bodies the latter of which is connected to the flap. The flap, shown in Fig. 2.5, parallel to the blade and for the time being considered as a rigid body, intersects the mechanism link at half of its length.

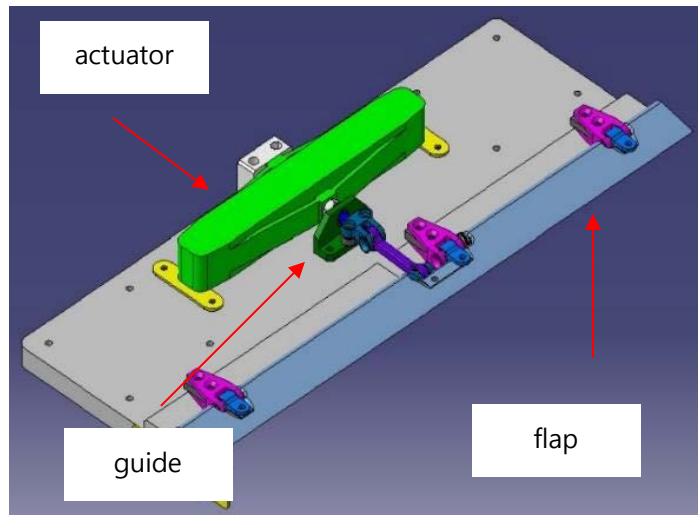


Figure 2.4 Drawing of the mechanism

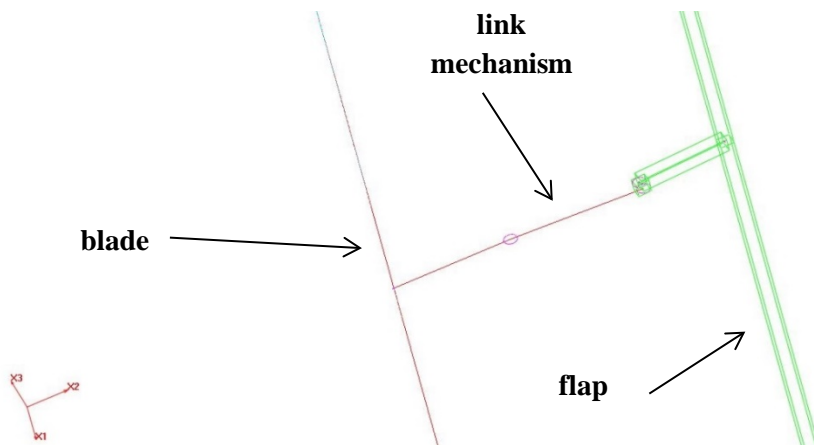


Figure 2.5 DYMORE schematic model

The hub where the two blades connect consists of a revolute joint linked with a vertical shaft clamped to the ground. The said revolute joint is where a rigid rotation is prescribed in order to evaluate the centrifugal load acting on the system.

As already mentioned, within the blade frame we can identify two

different areas: the main one consists of fiber glass roving while the part of the beam parallel to the flap holds within its blade skin a titanium bar placed in the front section chordwise. This means that the structural properties used in the DYMORE model differ whether we consider the roving section or the titanium one.

2.7 Micromechanics to estimate the properties of the composite materials used

While titanium properties, due to its homogeneous nature, are widely available, the same cannot be said for glass roving. Being a composite material, where the glass fibers are reinforced due to the action of a resin matrix, physical properties exhibit different behavior according to the direction the material is tested. As a consequence, the structural properties needed in the following computations have to be purposely calculated based on the percentage amount and the individual properties of the two components.

Micromechanics is a helpful tool which allows to retrieve the final properties taking into account the nature of the composite material constituents and the direction of the loads applied [24]. Once the material geometry is known, we are able to retrieve structural properties of the whole composite material simply exploiting the mechanics of materials approach.

Provided the composite is considered

- macroscopically homogenous
- linear elastic
- initially stress free

The longitudinal modulus results as

$$E_l = V_f E_f + V_m E_m \quad (23)$$

Where E_l is the longitudinal modulus of the composite material whereas V_f and V_m and E_f and E_m are respectively the volume fraction and the longitudinal modulus of the fiber and the matrix.

A similar approach can be exploited when computing the transversal modulus

$$\frac{1}{E_t} = \frac{V_f}{E_{tf}} + \frac{V_m}{E_m} \quad (24)$$

Where E_t is the transversal modulus of the composite material whereas V_f and V_m and E_{tf} and E_{tm} are respectively the volume fraction and the transversal modulus of the fiber and the matrix.

Finally, shear modulus is computed as

$$G = \frac{1}{\frac{V_m}{G_m} + \frac{V_f}{G_f}} \quad (25)$$

Where G_t is the shear modulus of the composite material whereas V_f and V_m and G_f and G_m are respectively the volume fraction and the shear modulus of the fiber and the matrix.

Results from the above computations are described in Table 2.1.

Table 2.1 Material properties

Properties	Titanium	Glass roving
EA (N)	1.978×10^7	8.459×10^6
EI_{flap} (Nm²)	1.876×10^4	8.339×10^3
EI_{lag} (Nm²)	5.292×10^2	4.042×10^2
GJ (Nm²)	7.476×10^2	5.456×10^2
Mass per unit span (kg/m)	9.280×10^{-1}	5.256×10^{-1}

2.8 Model features

The designed model will be equipped with different features able to provide a deeper insight in the behavior of the rotor. In the static analysis, when a prescribed rigid rotation is applied at the rotor hub, blades start rotating about the shaft which is instead rigidly clamped. Such motion will highlight the centrifugal forces acting along the blade and the axial load born at the root will be computed.

Another degree of motion considered in the DYMORE model is the oscillation of flap driven by an external force imposed in the proximity of the prismatic joint. This element allows the displacement of the whole link mechanism without any major influence to the blade; as the prismatic joint dilates and contracts the other components within the flap mechanism will

move accordingly.

The function which is imposed to the flap mechanism is related with the actual movement of the actuator and the input voltage provided to it. Whereas previously [10] no connection was taken into account between the input voltage and block force-stroke relationship which characterizes the actuator, a new revision instead a more detailed connection among the quantities, as displayed in Fig. 2.6.

Variation in the supplied voltage directly affects the actuator performances according to the formula

$$\frac{F}{F_{\max}} + \frac{x}{x_{\max}} = \frac{V}{V_{\max}} \quad (26)$$

Where F is block force, x is the stroke and V is the input voltage.

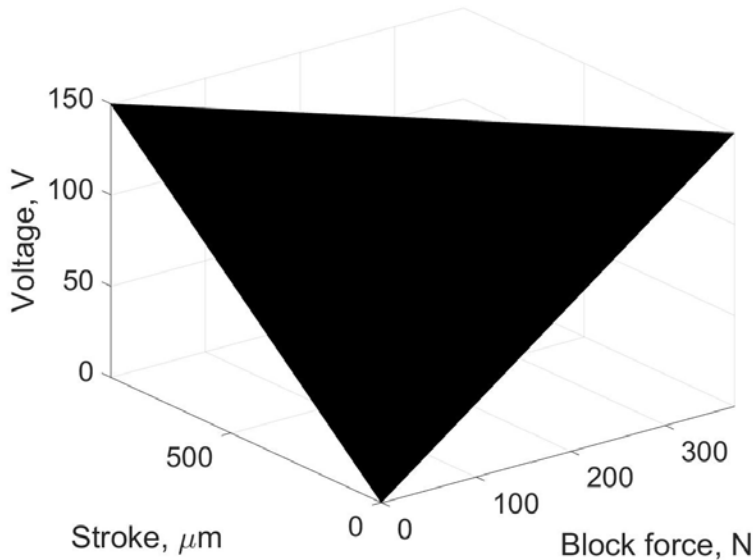


Figure 2.6 Relationship among the block force, input voltage, and stroke

Also, a kinematic equation is formulated in order to describe the flap motion during its actuation.

$$M = -k\vartheta \quad (27)$$

$$F = -\frac{k}{L_2}\vartheta \quad (28)$$

$$x = L_2(\vartheta_0 - \vartheta) \quad (29)$$

Where M and F are respectively the moment and force applied at the flap hinge, ϑ is the angular displacement, L_2 is the moment arm and k the torsional spring stiffness.

The torsional spring applied at the revolute joint aims at simulating the aerodynamic load over the flap. In fact, it works as if a pressure distribution was present over the flap and contrasted the surface movement once the aerodynamic environment is recreated. To determine the stiffness of the torsional spring and thus, the load to apply, ANSYS FLUENT calculations were exploited. The hinge moment coefficient previously extracted was plotted in Fig. 2.7 versus the deflection angle and a hysteresis-like distribution was retrieved.

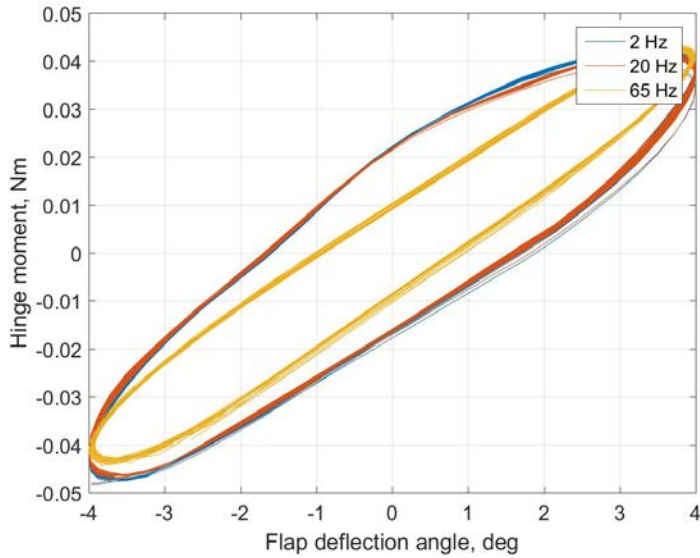


Figure 2.7 Hinge moment evolution

The data distribution can be summarized through a regression line per each of the frequencies considered; as the angle of the attack of the airfoil was 0 degrees for all the measurements, the plot shows a perfect symmetry around the chart origin. Once the analytical formula of the regression line is obtained, slope and y-intercept are first transformed into Chebyshev coefficients [25] and then used to define the stiffness of the torsional spring. Nonetheless, as the hinge moment coefficient does not vary significantly as the actuation frequency grows, springs features visible in Table 2.2, will not differ much one another.

Table 2.2 Chebyshev coefficients

Frequency [Hz]	Zero grade coefficient	First grade coefficient
2	$-3 \cdot 10^{-4}$	0.5815
20	$-2 \cdot 10^{-4}$	0.5734
65	$9 \cdot 10^{-6}$	0.5962

Being all the parameters defined, the final formulation which connects input voltage, block force and stroke results from the combination of eqs. (27) and (30).

$$V = -V_{\max} \left(\frac{k}{L_2 F_{\max}} + \frac{L_2}{x_{\max}} \right) \mathcal{G} + \frac{L_2 V_{\max}}{x_{\max}} \mathcal{G}_0 \quad (30)$$

Other than the prescribed rotations, within DYMORE capabilities, aerodynamic influence can also be observed. As a consequence, a further analysis implemented model focuses on the aerodynamic conditions. Each blade is provided spanwise with a lifting line which is a collection of points, called airstations, measuring different parameters of the incoming flow; for the current analysis a number of 81 equally spaced airstations were exploited.

2.9 Pulling test implementation

The use of the ATF in a rotating environment implies the ability of the whole device to cope with the centrifugal force which springs from the blade rotation. A structural analysis of the actuator by NASTRAN has already been conducted [26] and a strain which amounted to 33.5% of the

allowable was obtained when distance from the rotation center was 1.125 m. Now instead, the designed and manufactured pulling test, displayed in Fig. 2.8, focused on the whole device axial strength as well as the flap deflection in a non-static context. In fact, other than the blade stiffness [27], the outcomes of the described experiment will give an estimation of the flap displacement reduction compared to a static case.

The intrinsic dynamics of the rotor and the friction between the flap and the static section of the blade are two of the elements which contribute to a decrease of the displacement once the rotating conditions are considered. Consequently, the deflection aimed at in the static case should be high enough to guarantee a successful operation of the device and thus an efficient dampening of the vibrations in the final conditions.

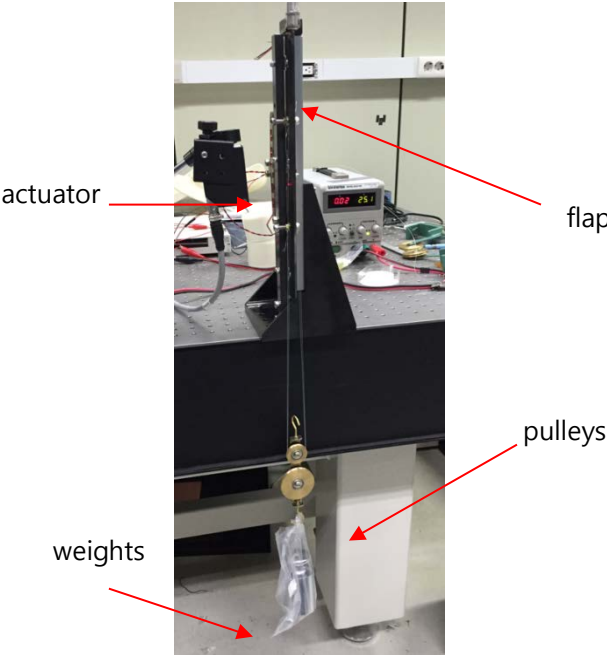


Figure 2.8 Pulling test test-bed

III. NUMERICAL AND EXPERIMENTAL RESULTS

3.1 Steady state results

Once all the parameters listed in Table 3.1 are set, the solution can be thus initialized using the flow values at inlet as the initial guess.

Before implementing the proper analysis, evaluation of lift, drag and moment coefficient were performed for the airfoil without any flap deflection. Data were collected for $[-10^\circ, 10^\circ]$ span and the correspondent curves first constructed as shown in Figs. 3.1, 3.2 and 3.3.

Table 3.1 Aerodynamic analysis conditions

Flap location [m]	1.125
Flap length [m]	0.300
Flap chord [m]	0.023
Mach number	0.45
Fluid density [kg/m^3]	1.125
Temperature [K]	300
Flow condition	Viscous, compressible

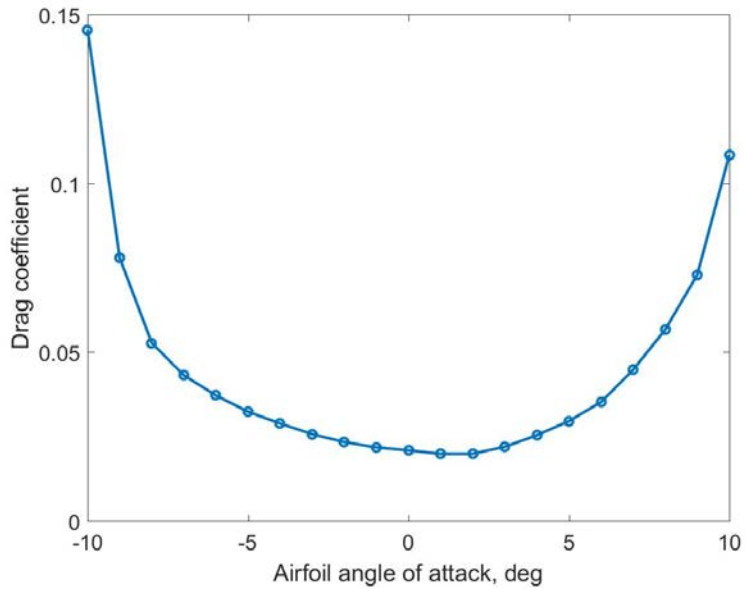


Figure 3.1 Drag coefficient with no flap deflection

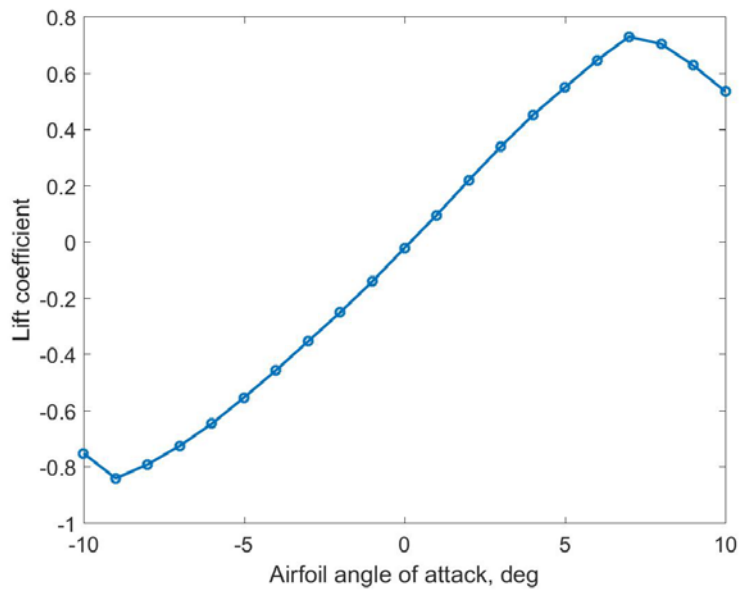


Figure 3.2 Lift coefficient with no flap deflection

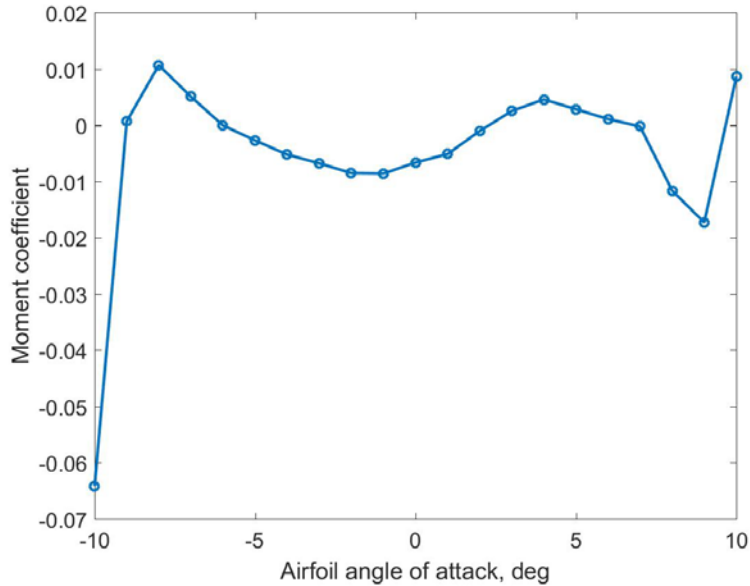


Figure 3.3 Moment coefficient with no flap deflection

As expectable [13], drag coefficient is characterized by symmetrical aspect about the axis passing through 0° , and 10° and -10° are the highest peaks. Lift, instead shows a gradually increasing trend where the stalling point at 9° and -9° are easily visible. Finally, moment coefficient does not have remarkable variation in the range considered although in correspondence of 10° and -10° absolute values start growing.

In the final analysis, the aerodynamic coefficients will not be constant but change as the flap oscillates between 4° and -4° and the resulting pressure distribution will directly act on the linking rod and generate internal forces within the beams constituting the mechanism link. To verify whether the actuator and the device have the necessary strength to sustain and overcome the external forces, a static analysis simulates the flap deflected by 10° and extracts the values of aerodynamic coefficients

visible in Figs. 3.4, 3.5 and 3.6.

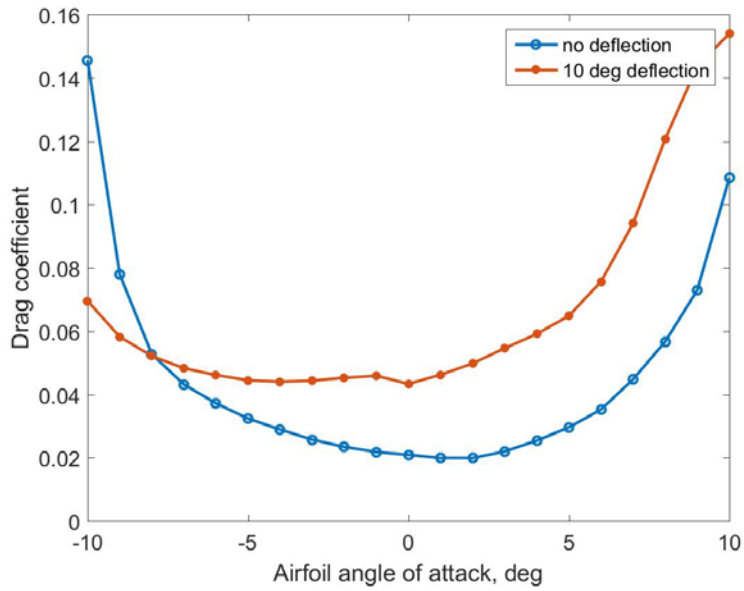


Figure 3.4 Drag coefficient comparison

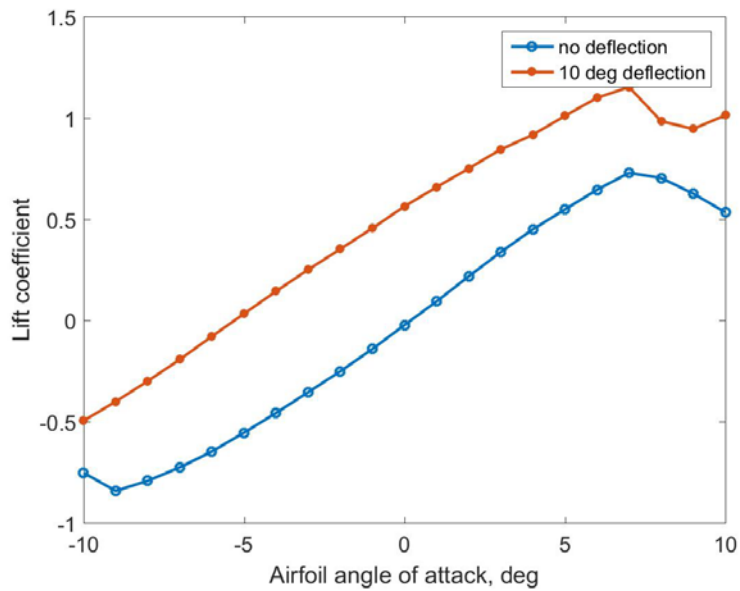


Figure 3.5 Lift coefficient comparison

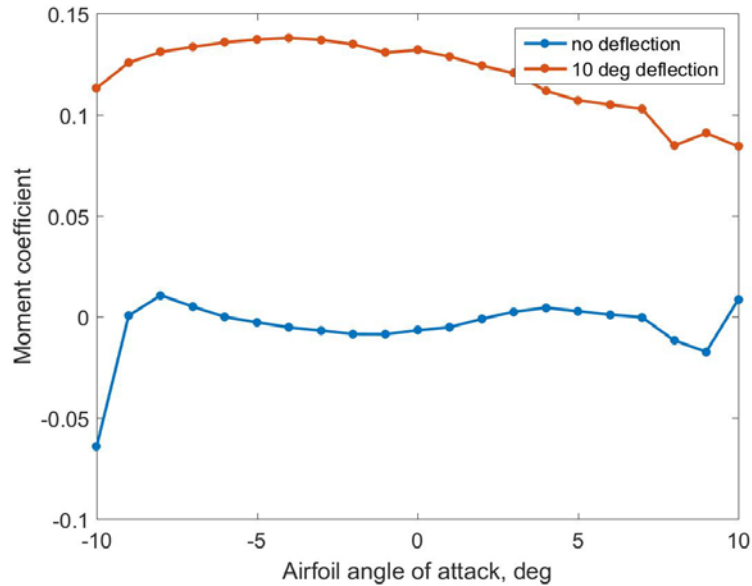


Figure 3.6 Moment coefficient comparison

The comparison between the case with no flap deflection and the case where the flap is deflected by 10° shows a general increase in drag coefficient. This result is due to the fact that the normal surface hit by the flow, with the exception of the -10° configuration, is broader. In that specific case only the main body is hit by the flow while the deflected flap is parallel to the streamlines and does not contribute in terms of frontal area. Results coming from lift coefficient analysis show why moving surface are widely employed: the constant offset visible in the comparison with the non-deflected flap case occurs when the flap deflects and the airfoil chord gets longer resulting in the increase of the lift coefficient. Moment coefficient as well has a positive offset.

The accuracy of the current mesh was questioned comparing the extracted aerodynamic coefficients with results from a similar analysis

where a more refined mesh (2990 hexahedral and 14212 triangular elements) was in use.

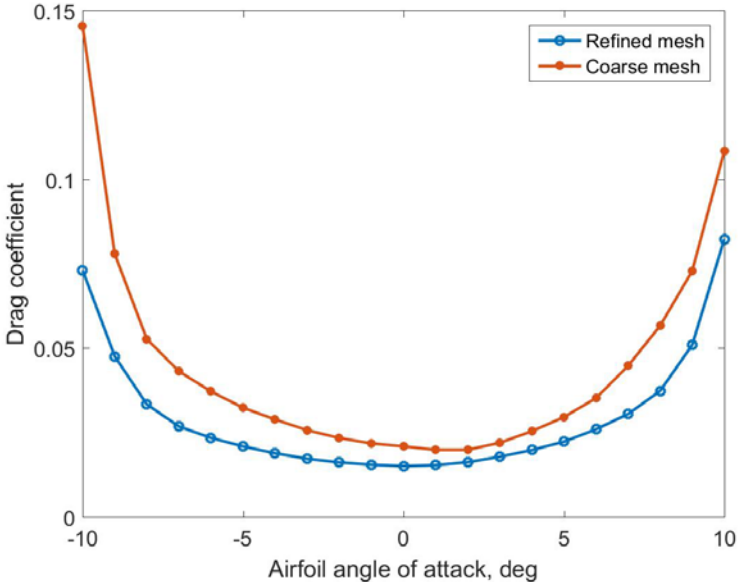


Figure 3.7 Refined mesh-coarse mesh comparison for drag

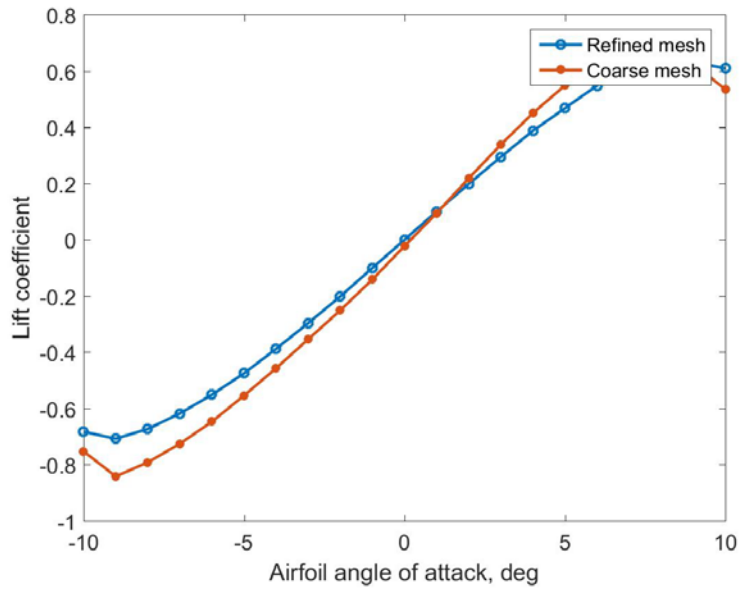


Figure 3.8 Refined mesh-coarse mesh comparison for lift

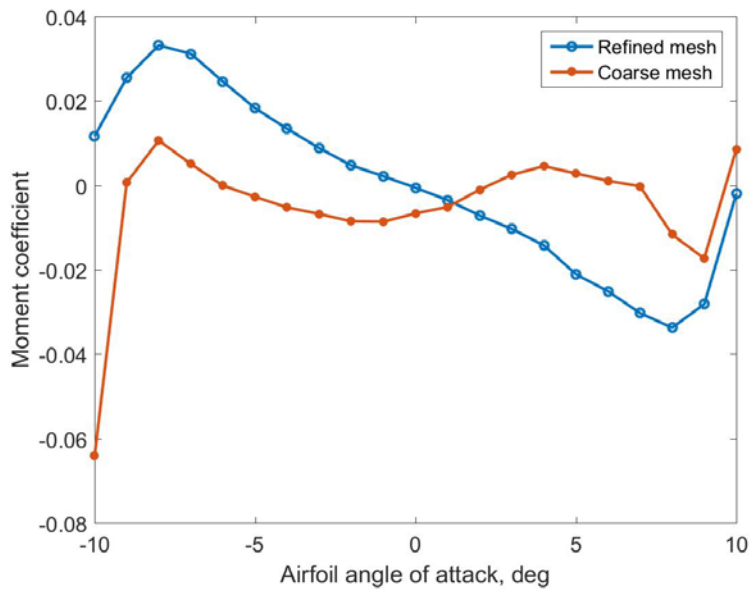


Figure 3.9 Refined mesh-coarse mesh comparison for moment

Although results from both analyses, represented in Figs. 3.7, 3.8 and 3.9, have a strong similarity, refined mesh shows smoother and perfectly symmetric, in drag coefficient case, and antisymmetric, in the case of moment and lift coefficients, trend. As far as values are concerned, the widest gap between the two data sets is seen in the lift coefficient in correspondence of both stalling angles, as also depicted in Fig. 3.9, where flow instability is at its peak.

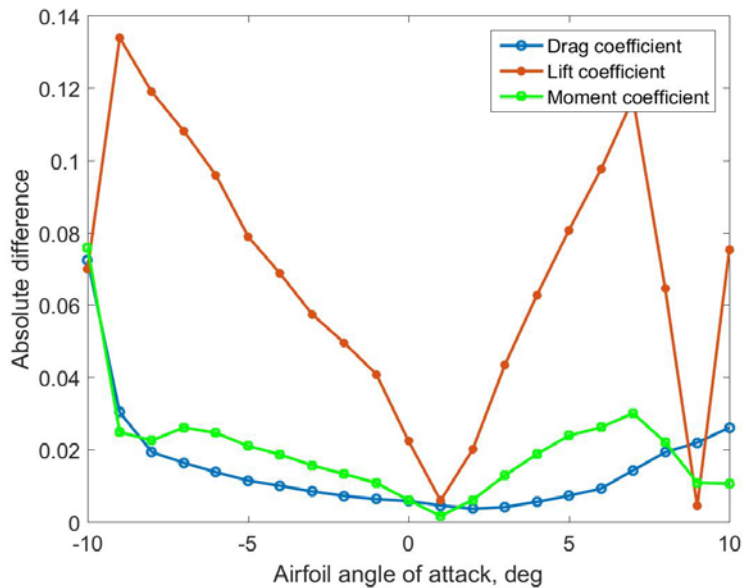


Figure 3.10 Absolute difference between the coarse and refined mesh

Nevertheless, the highest reliability of the results coming from the refined mesh does not justify its use in the actual computation; as a matter of fact, the transient analysis, ultimate goal of our research, already requires a relevant computational cost which would be further aggravated by the increase in the number of nodes.

Static analysis was also exploited to retrieve values for the hinge

moment coefficient so as to compare it with the ideal fluid formulation and evaluate the possible discrepancies.

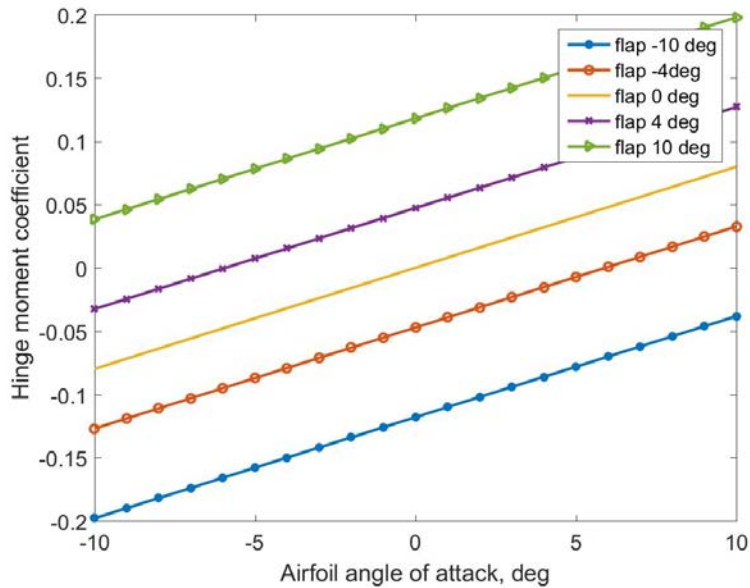


Figure 3.11 Hinge moment trend according to Walz and Chopra [8]

Ideal fluid formulation in Fig. 3.11 shows that as the angle of attack of the airfoil increases, hinge moment coefficient grows due the pressure distribution on the lower surface of the flap which results in a counterclockwise rotation. Moreover, higher flap deflection angles (angles are measured positive when flap deflects downward) imply a further increase in the value of hinge moment coefficient

Specifically, when the prediction of the hinge moment coefficient for 0 degrees of angle of attack is compared with the results extracted from ANSYS FLUENT analysis, a relatively ample discrepancy is observed in Fig. 3.12; this is mostly due to the specific layout of the airfoil considered in the CFD analysis where the single slot is responsible for phenomena

extremely difficult to model. Nevertheless, as the static analysis is conducted at a deflection angle outside the expected range simply to estimate the highest values which could be encountered, the results obtained in ANSYS FLUENT are chosen in light of a more conservative approach.

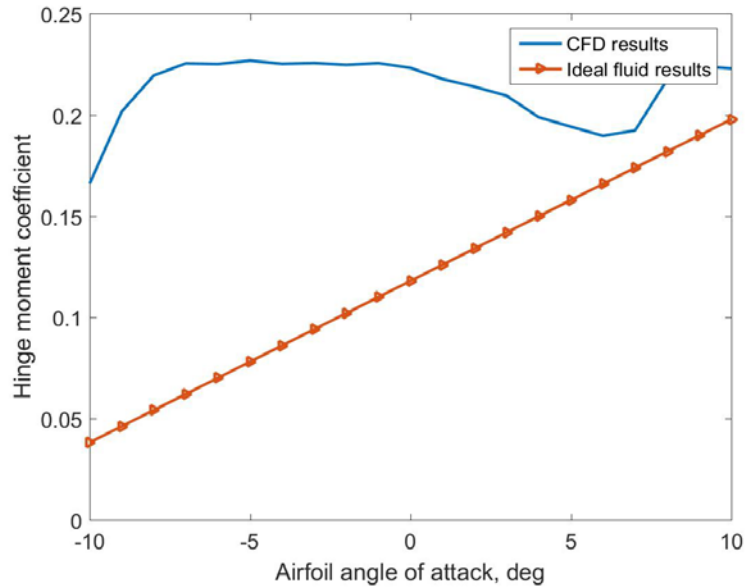


Figure 3.12 Hinge moment comparison with 10° flap deflection

3.2 Transient state results

In transient analysis aerodynamic coefficients are measured for different angles of attack, to observe the range of oscillation, and for different frequencies of actuation of the flap. The outcomes are plotted in Figs. 3.13-3.21.

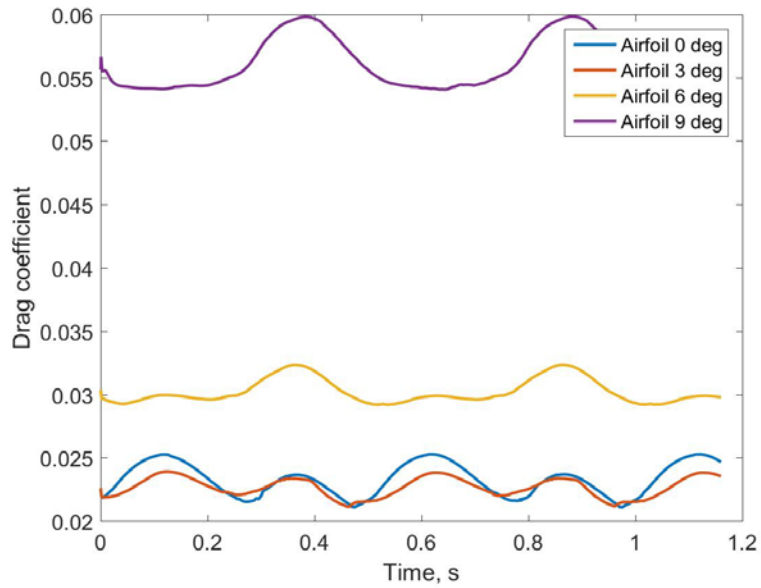


Figure 3.13 Drag coefficient at 2 Hz flap actuation

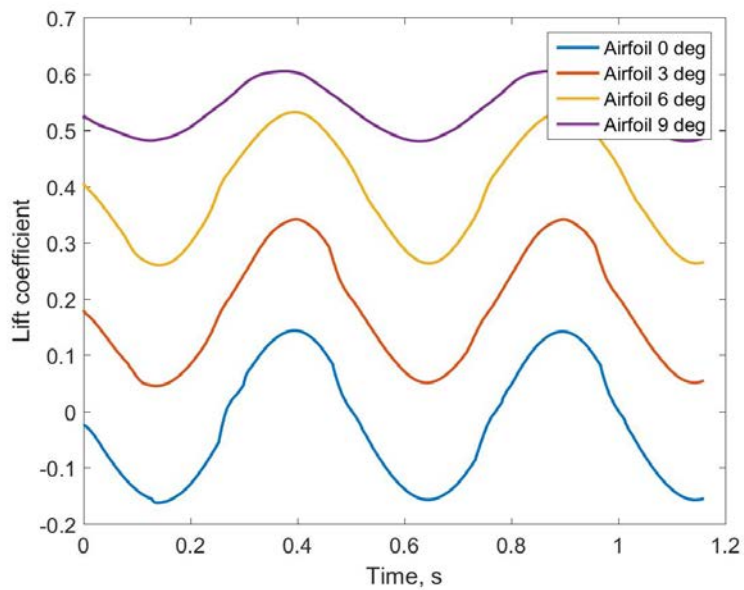


Figure 3.14 Lift coefficient at 2 Hz flap actuation

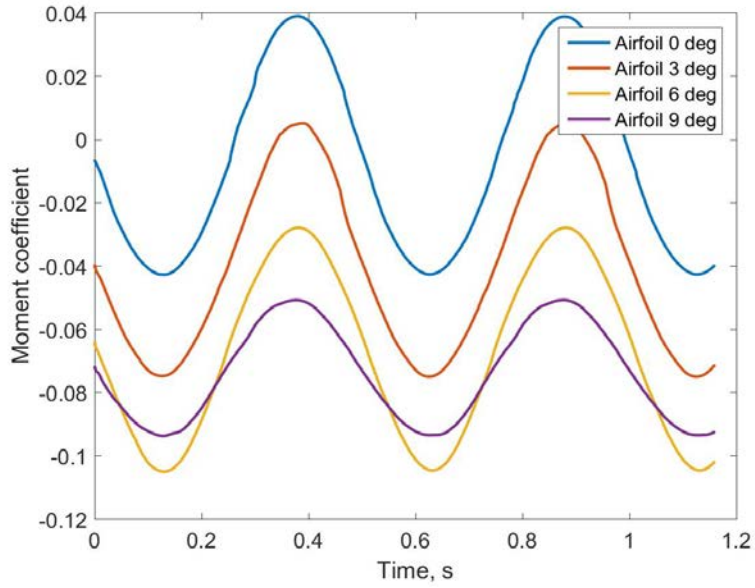


Figure 3.15 Moment coefficient at 2 Hz flap actuation

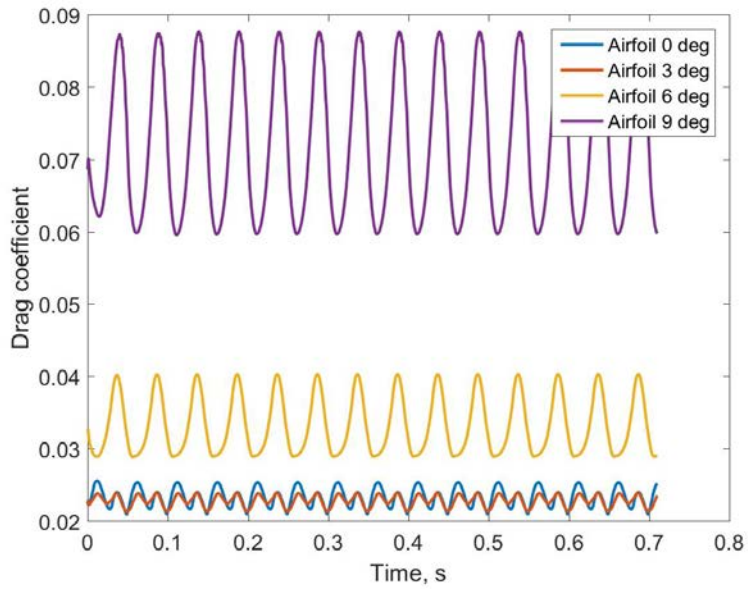


Figure 3.16 Drag coefficient at 20 Hz flap actuation

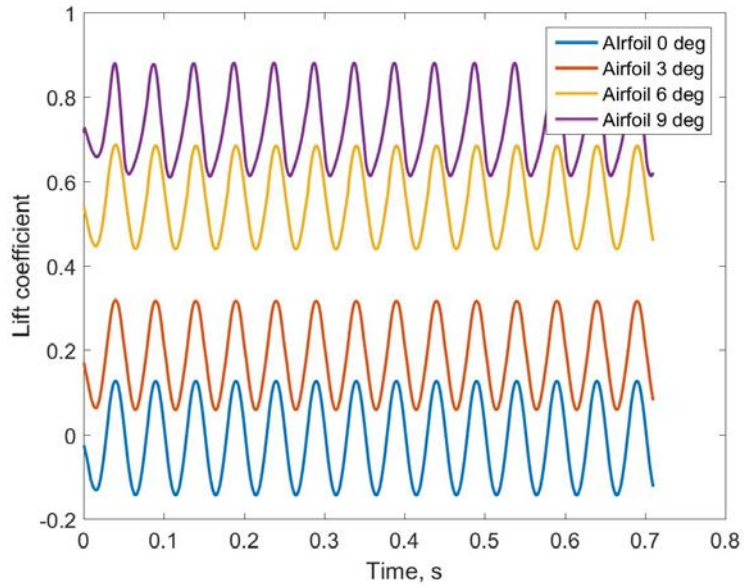


Figure 3.17 Lift coefficient at 20 Hz flap actuation

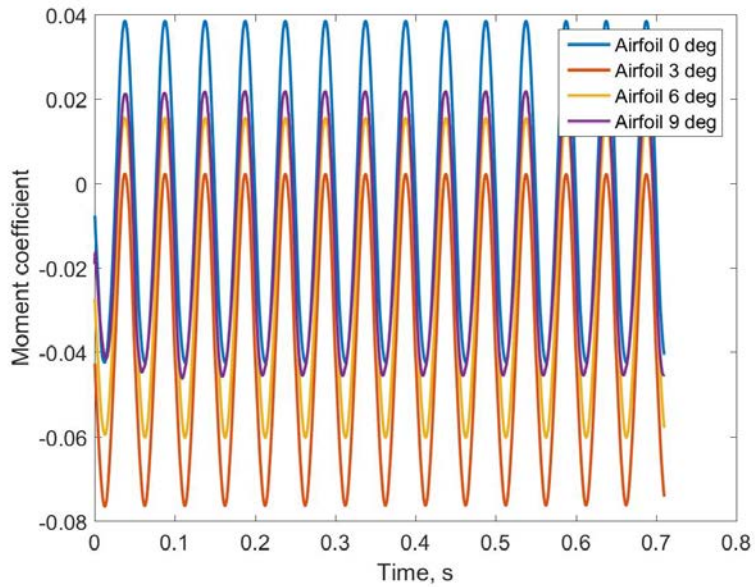


Figure 3.18 Moment coefficient at 20 Hz flap actuation

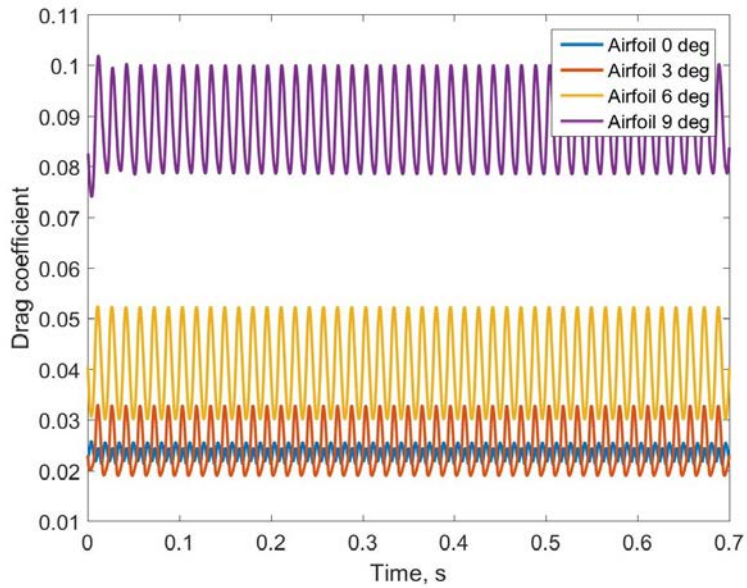


Figure 3.19 Drag coefficient at 65 Hz flap actuation

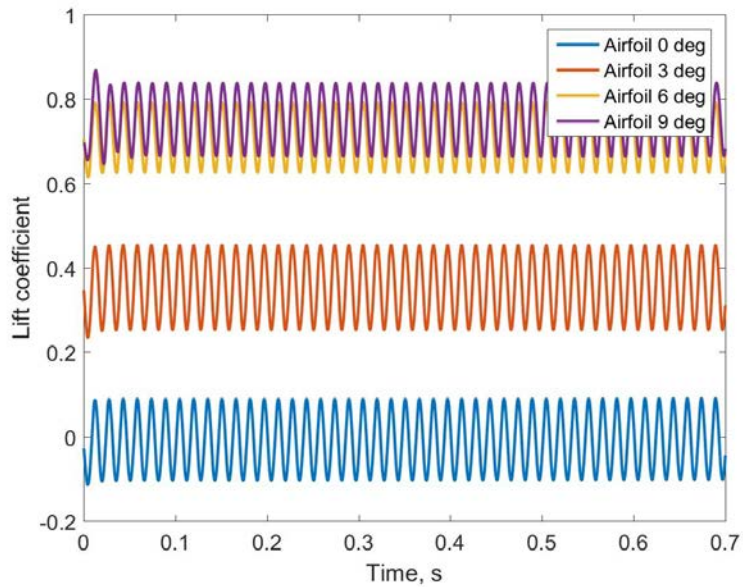


Figure 3.20 Lift coefficient at 65 Hz flap actuation

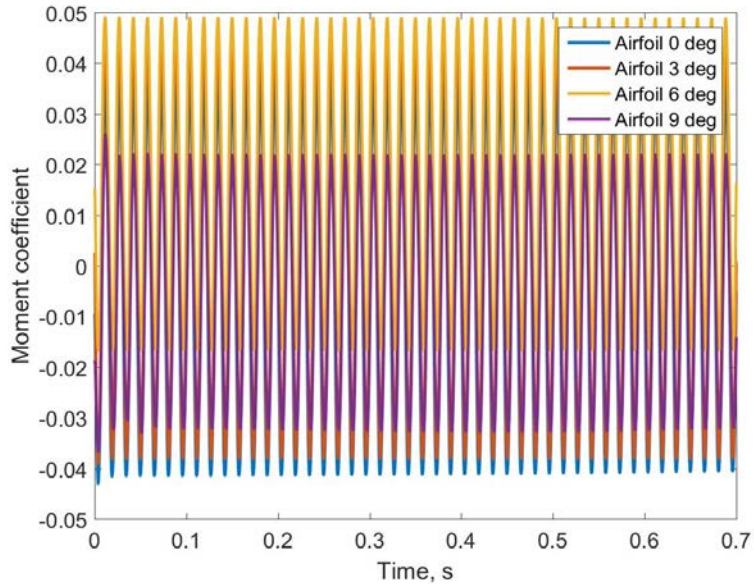


Figure 3.21 Moment coefficient at 65 Hz flap actuation

As visible in the different figures, while the frequency changes, aerodynamic coefficients do not encounter any radical modification. This result should be expected given that the lift, moment and drag coefficient values do not have any connection with the frequency of actuation of the flap and no significant loss due to fluid movement occurs. Nonetheless, discrepancies are observed between analyses where the angle of attack was equal but a different frequency of actuation was imposed: this is probably due to numerical mistakes which originate from the coarse mesh and critical areas such as the trailing edge and the slot.

Lift coefficient increases regularly as the angle of attack grows although overlapping between the graphs is visible in the surroundings of the stall angle. On the contrary, drag coefficient values overlap for smaller angles of attack and steeply grows up to 0.09 when deflection reaches 9 degrees; drag coefficient is also characterized by the increase of oscillation range

due to the projection of the flap with respect to relative wind: the growing angle of attack sums up to the deflection angle and this results in a broader spectrum of drag coefficient value.

Finally, moment coefficient does not show any remarkable trend and, regardless of the angle of attack, oscillates within a limited range.

At last, the main objective of the CFD analysis, the hinge moment, is retrieved in Figs. 3.22, 3.23, and 3.24 simply considering the moment balance about the flap hinge placed at 0.11442 m from the leading edge. As observed with pitch moment, there no definite connection between the hinge moment values and the angle of attack growth, at least in the range examined. Nonetheless, given that the range of oscillation for all the frequencies remains constant, we can conclude that no major energy losses occur during flap actuation despite the viscosity of the fluid.

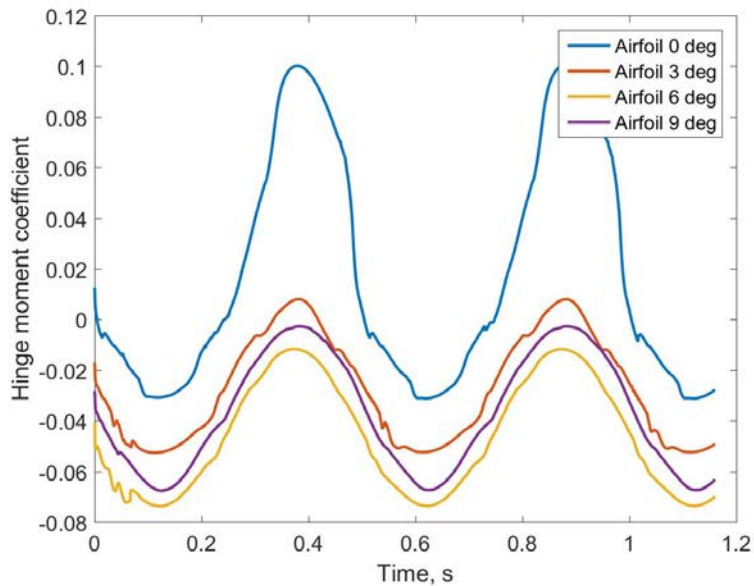


Figure 3.22 Hinge moment coefficient at 2 Hz flap actuation

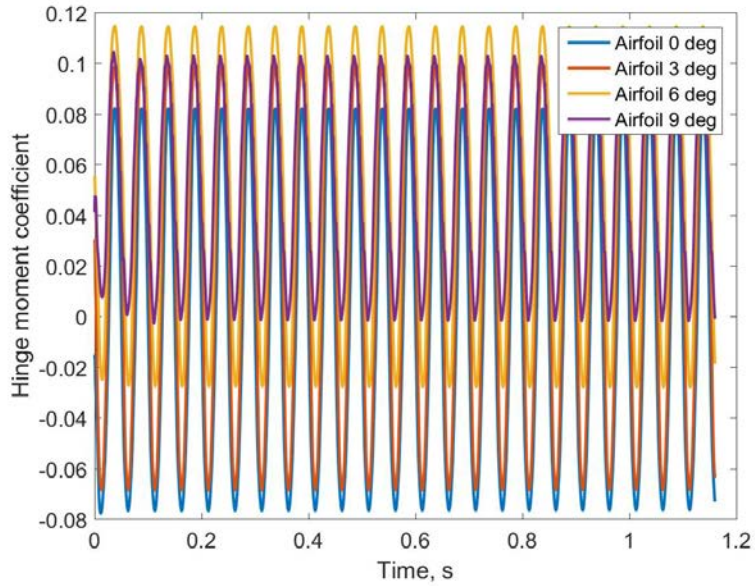


Figure 3.23 Hinge moment coefficient at 20 Hz flap actuation

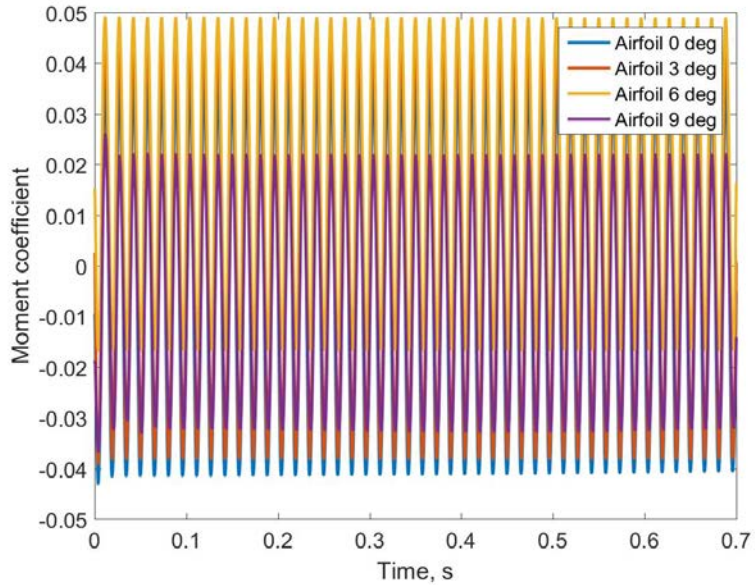


Figure 3.24 Hinge moment coefficient at 65 Hz flap actuation

In the light of the hinge moment acting on the flap during the transient

analysis, in Fig. 3.25 the deflection angle was evaluated in terms of the available moment arm length was evaluated and showed that when aerodynamic conditions are applied, despite the hinge moment acting over the flap which moves at 20 Hz, the minimum requirement of 4° flap deflection is still achievable.

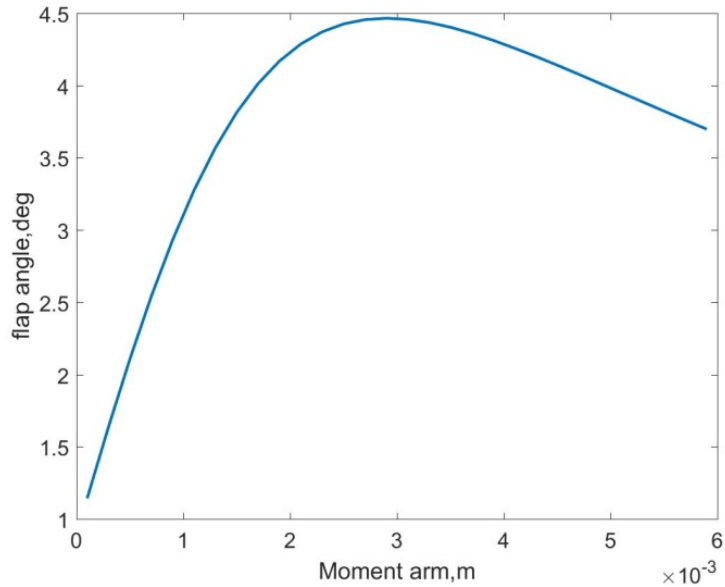


Figure 3.25 Flap deflection as a function of the moment arm length (predicted)

3.3 DYMORE centrifugal load analysis

The first analysis conducted focuses on the centrifugal acceleration which will occur once the system starts rotating. In order to validate the model accuracy, theory formulations is also considered using the following data: blade length of 1.5 m and specific mass which is 0.928 kg/m for the titanium bar and 0.527 kg/m for the glass roving. When the rotor moves at 172 rad/s the total force at blade root is:

$$\begin{aligned}
\int_{root}^{tip} dF &= m_{glass} \int_{section1} da + m_{glass} \int_{section2} da + \dots \\
&\dots + m_{titanium} \int_{section3} da + m_{titanium} \int_{section4} da = \\
m_{glass} \omega^2 \int_{section1} dr &+ m_{glass} \omega^2 \int_{section2} dr + \dots \\
&\dots + m_{titanium} \omega^2 \int_{section3} dr + m_{titanium} \omega^2 \int_{section4} dr \approx 13,000N
\end{aligned}
\tag{31}$$

As visible in Fig. 3.26, once the rotor reaches the full speed, the axial force acting along the blade registered by DYMORE model accounts only for slightly more than 15,000 N; the discrepancy with the theory formulation is justifiable by the beam elasticity which subtracts part of the axial solicitation. Also, the part of the link mechanism designed as rigid body is not accounted by DYMORE given that only beams are considered as objects with mass. Once both aspects are taken into account, the discrepancy between DYMORE model and theory application will be reduced considerably.

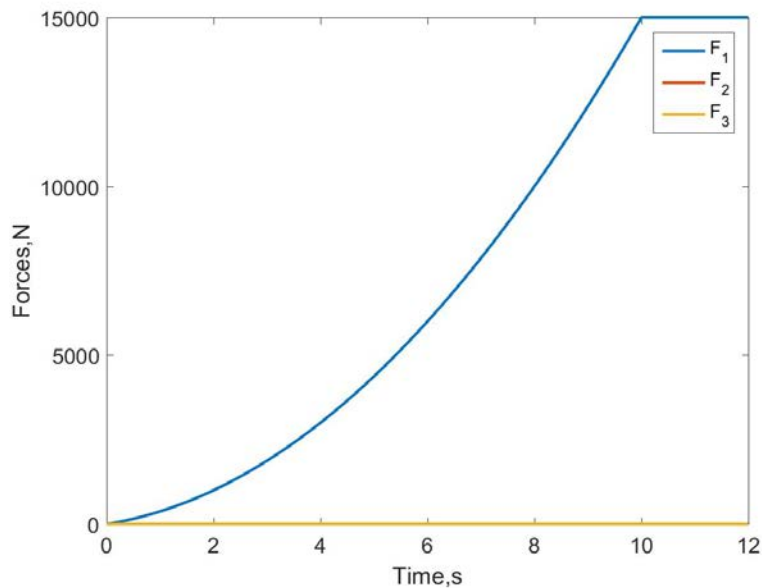


Figure 3.26 Internal forces at the blade root

Confirmation of the DYMORE model is guaranteed when the same analysis is conducted instead at the blade tip in Fig. 3.27 Due to the fact that no constraints are applied on this extremity, no internal forces should be registered when the only external solicitation consists of the prescribed rigid rotation.

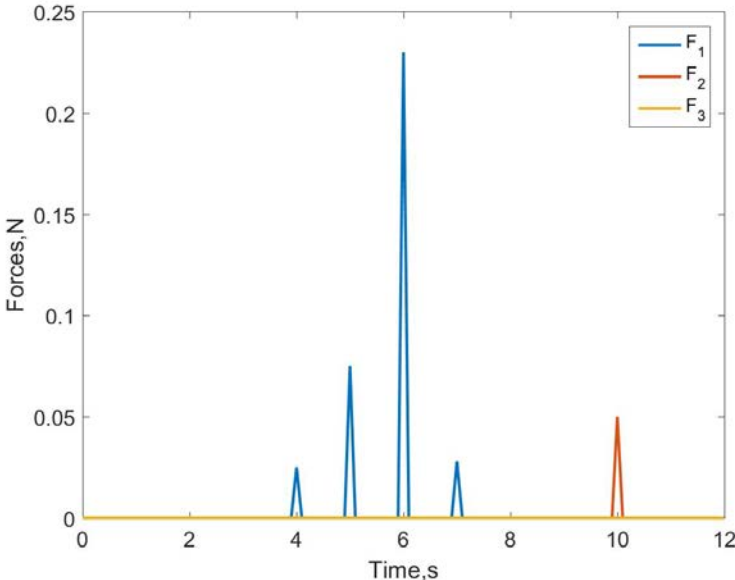


Figure 3.27 Internal forces at the blade tip

As a consequence, the only forces sensed at the blade tip, whose values are infinitely smaller than what registered at the blade root, derive from numerical inaccuracies and do not have any physical origin.

3.4 DYMORE flap deflection analysis

Given that the relationship among block-force, actuator stroke and input voltage has already been defined, the function corresponding to the desired output is then inserted in DYMORE static model as results in Figs. 3.28, 3.29 and 3.30.

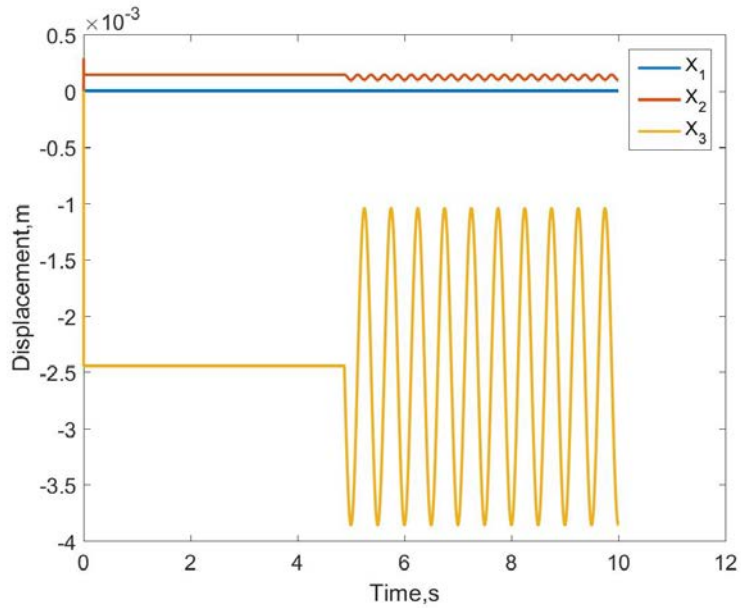


Figure 3.28 Flap deflection at 2 Hz actuation

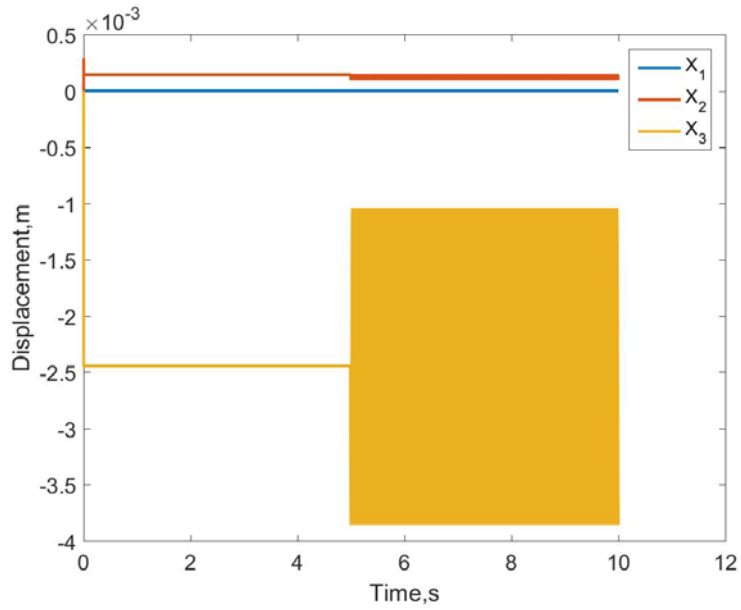


Figure 3.29 Flap deflection at 20 Hz actuation

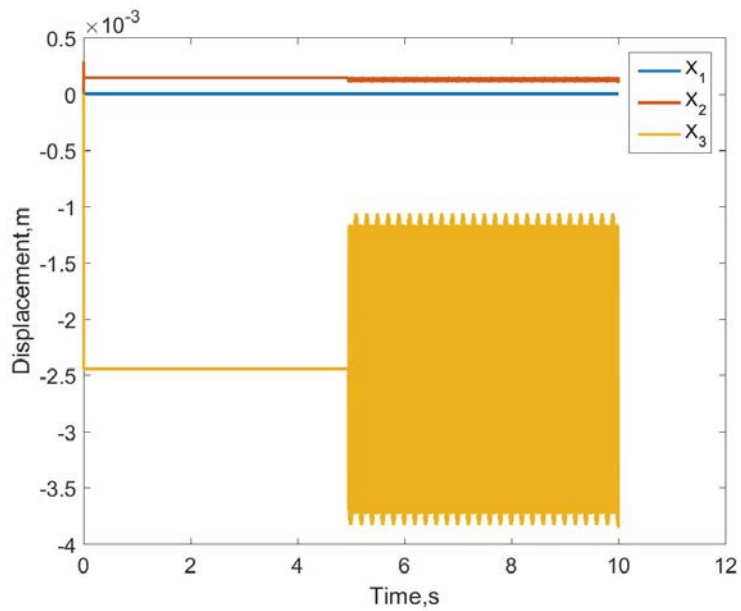


Figure 3.30 Flap deflection at 65 Hz actuation

From the geometry configuration we know that the flap chord length is 0.0203 m and observing the results from DYMORE we can determine that, despite the elasticity of the beams within the mechanism link, the vertical displacement of the flap corresponds to an angular rotation of $\pm 4^\circ$.

3.5 DYMORE aerodynamic loads analysis

Aerodynamic conditions have to be evaluated so as to complement what extracted from ANSYS FLUENT and, at the same time, obtain a more global description of the fluid flow all over the blade. A first analysis is conducted in hover conditions and with no flap displacement. The aerodynamic data considered consist of 272 rad/s rotation and 81 stations equally spaced along the single lifting line which spans from the blade root at 7.62×10^{-2} m from the hub to the blade tip at 1.5 m distance from the rotating center.

The total airloads acting on the single blade are shown in Fig. 3.31.

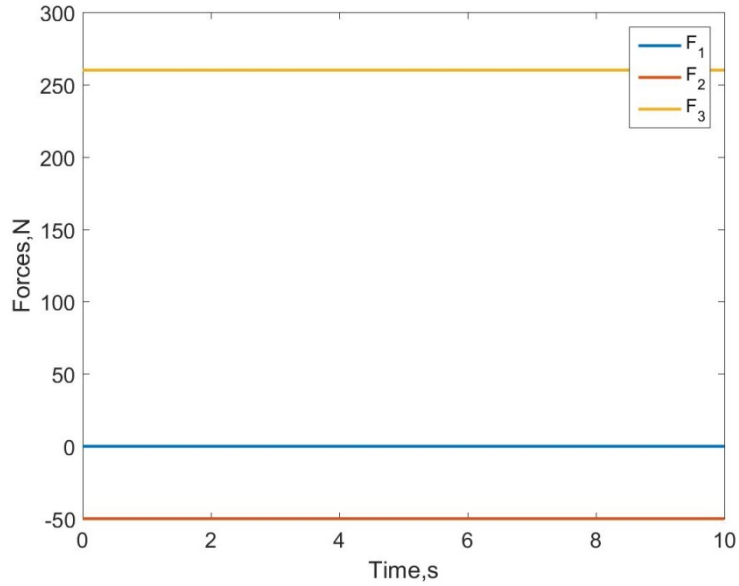


Figure 3.31 Total airloads over a single blade

While no axial load due to aerodynamic forces is observed, the effects of the lift and the drag are visible. In order to validate the results, theoretical approach is exploited.

If we consider the infinitesimal lift as

$$dL = \frac{1}{2} \rho v^2 c c_L dr = \frac{1}{2} \rho \omega^2 c c_L r^2 dr \quad (32)$$

And standard air density at 1.225 kg/m^3 and lift coefficient at 0.1, we obtain:

$$L = \frac{1}{2} \rho \omega^2 c c_L \frac{r^3}{3} = 275 \text{ N} \quad (33)$$

If reference frame is taken into account, same validation is possible for drag force.

$$dD = \frac{1}{2} \rho v^2 c c_D dr = \frac{1}{2} \rho \omega^2 c c_D r^2 dr \quad (34)$$

$$D = \frac{1}{2} \rho \omega^2 c c_D \frac{r^3}{3} = 50N \quad (35)$$

Values of the airloads at the single airstation can be retrieved as well; in the case of the airstation placed at the blade root results are as portrayed in Fig. 3.32.

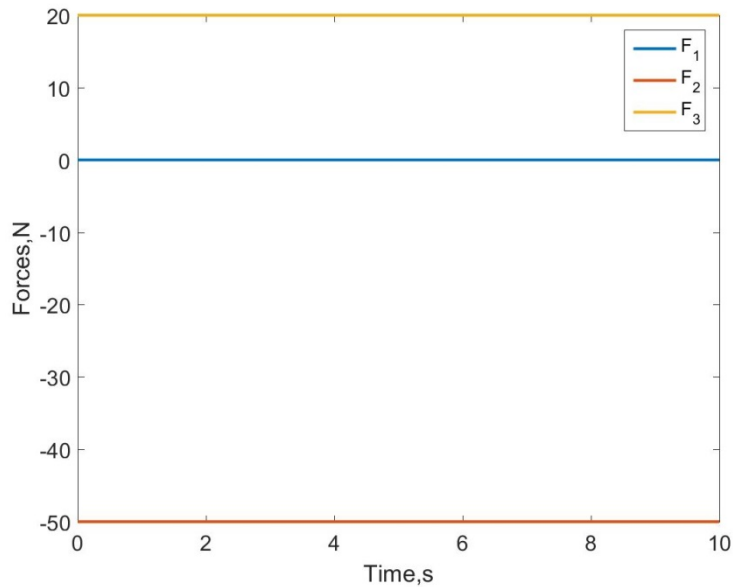


Figure 3.32 Airloads at the blade root

If instead, data from the airstation at the blade tip are observed, we notice in Fig. 3.33 a relevant increase in sectional lift and null values of drag.

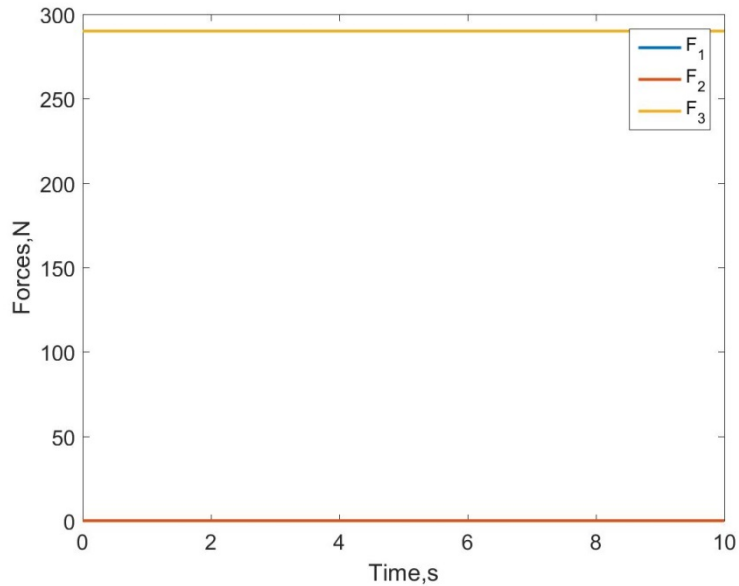


Figure 3.33 Airloads at the blade tip

The final analysis aerodynamic conditions are superimposed over the flap deflection movement imposed and the resulting outcomes are obtained. Centrifugal force instead, is not considered given that in dynamic analysis, implemented to observe aerodynamic loads, it is ignored [25].

Among the different results, the focus was on the flap displacement so as to verify whether any particular event would occur due to the influence of the aerodynamic loads. The actuation frequency imposed, as in the previous static case, amounted to 2 Hz, 20 Hz and 65 Hz.

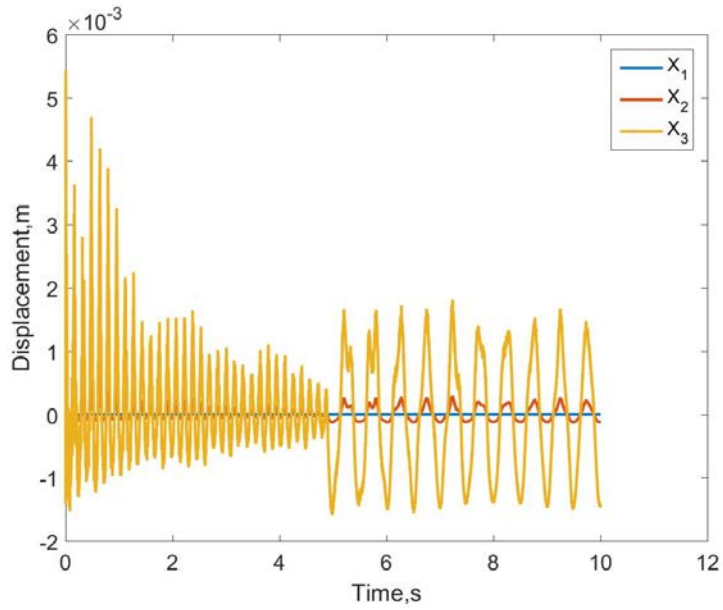


Figure 3.34 Flap deflection at 2 Hz with airloads

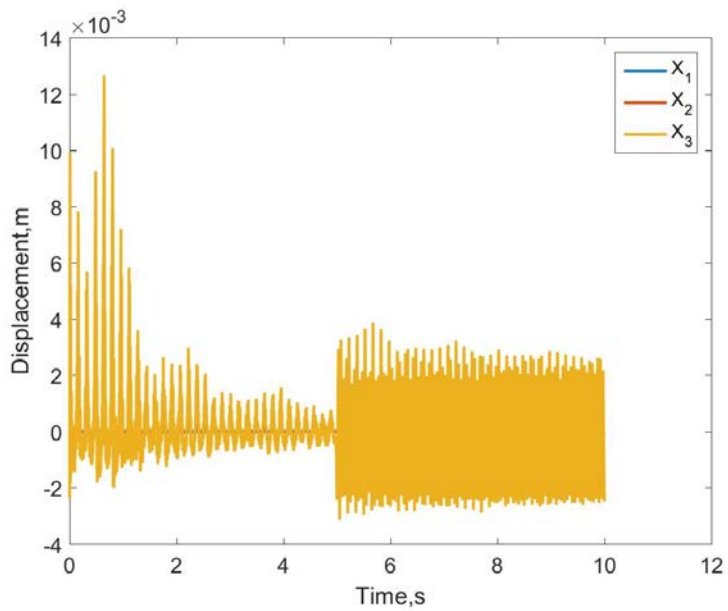


Figure 3.35 Flap deflection at 20 Hz with airloads

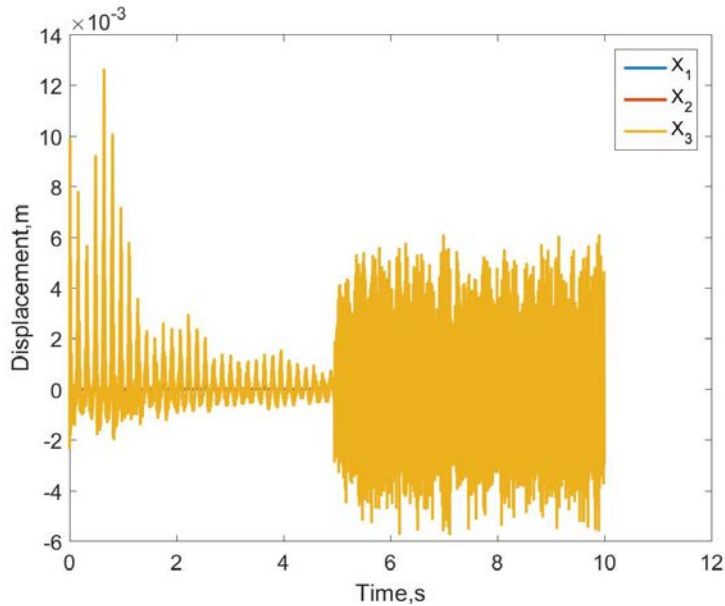


Figure 3.36 Flap deflection at 65 Hz with airloads

As visible in Figs. 3.34, 3.35 and 3.36, dynamic conditions along with the influence of aerodynamic loads, although not directly on the flap as it lacks of any airstation, worsen the definition of a smooth trend in the oscillation. Nonetheless, throughout the actuation period the range remains constant and no obvious divergence is visible. The angular displacement measured in the case where only flap oscillation occurred showed a rotation of $\pm 4^\circ$; when the same approach is repeated we observe that for 2 Hz actuation the deflection angle amounts to $\pm 4,2^\circ$ but at 65 Hz actuation the value skyrockets to $\pm 12^\circ$. Therefore, aerodynamic conditions play a major role in the definition and smoothness of the flap movement. On the other hand, disturbances occurring in this situation have a decreasing evolution and we can expect they will shrink to negligible values in a relatively short period of time. As an example, we observe in Fig. 3.37 the

converging evolution to which the internal forces at the blade root are subjected.

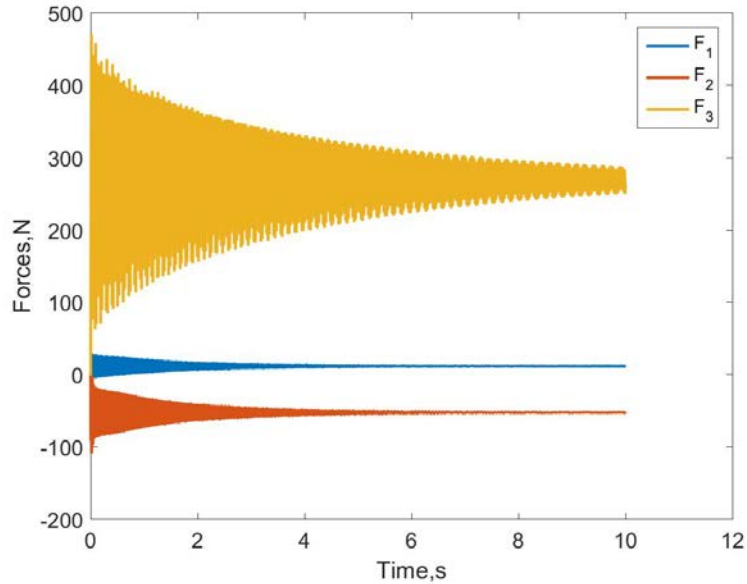


Figure 3.37 Internal forces at the blade root in aerodynamic conditions

3.6 Pulling test results

The manufactured test bed was designed in order to maintain the actuator, the mechanism link and the flap in a vertical position during the experiment; a laser sensor was also exploited to measure the oscillations of the flap. The centrifugal force was recreated through dead weights connected and clamped to the flap thanks to a system of pulleys and wires where the latter were arranged in such a way that the oscillations of the flap would affect the stillness of the dead load applied. Due to the flap

weight of 20 g, the load exerted on the surface will reach the ultimate goal of 40 kg in a gradual way. As expected, in Fig. 3.38 a decrease in the angular displacement could be witnessed.

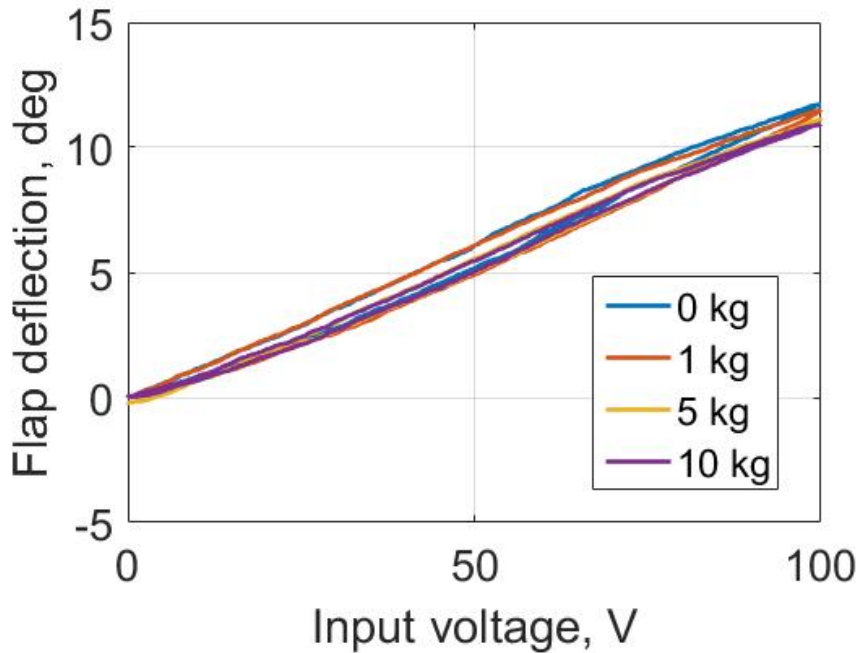


Figure 3.38 Flap deflection under the dead loads

The detail in Fig. 3.39 shows how, compared to the initial maximum deflection of 11.5 degrees, when 10 kg were applied as a dead load, the resultant deflection diminished to 10.9 degrees.

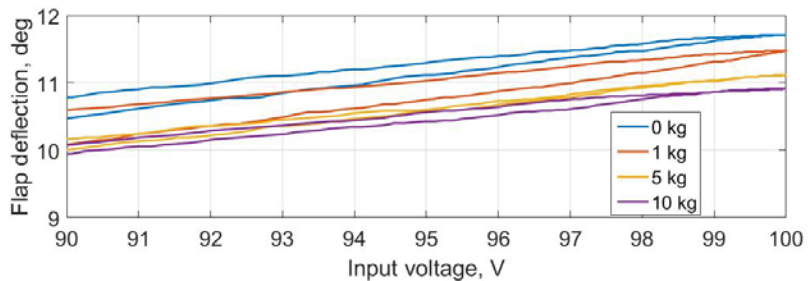


Figure 3.39 Flap deflection under the dead loads [detail]

We also have to consider that, among the different components of the active trailing edge flap, the actuator has the highest mass, being 190 g. Given that the computed load to apply to the device in order to test its strength to centrifugal force is expected to be 400 kg, a pulling test as conducted previously is not possible. As a consequence, an Instron machine, a device able to impose high tensions to the sample, will be exploited; what is more, due to the intrinsic features of a piezoelectric materials which couple mechanical strains with voltage output and vice versa, a dummy actuator, retaining the structural properties of the original one, will be designed and manufactured in order to avoid any possible damage.

IV. CONCLUSION AND FUTURE WORKS

4.1 Conclusion

In this dissertation, the small scaled blade equipped with an active trailing edge flap was analyzed and tested in order to verify its ability to suppress vibratory load generated on the rotor system. Given that the flap will be subjected to forces originating from the aerodynamics, lift, drag and moment coefficients estimations were extracted through a CFD analysis. In particular, so as to verify a smooth and successful operation of the device, the attention was focused over the hinge moment which will counteract the flap oscillation driven by the actuator. The results retrieved from different analyses where the actuation frequency and the airfoil angle of attack varied showed the peak of hinge moment coefficient at 0.17.

Also, a multibody dynamic analysis was implemented to couple the structural properties of the prototype with the aerodynamics generated in a whirl tower; DYMORE was selected as the tool to compute internal forces within the device generated by external loads such as centrifugal force and aerodynamic forces. In addition to that, flap displacement was added to observe its behavior in presence of disturbances. The centrifugal force and the aerodynamic loads measured looked plausible and were also validated through theory formulation and $\pm 4^\circ$ flap oscillation was achieved once the proper input was imposed.

Other than computer based simulation, a practical test was conducted to verify the decrease in oscillation range the flap will be subjected in a rotating environment. As a matter of fact, the centrifugal force acting on the blade will disturb the free movement on the flap and thus, reduce its effective displacement. A set of weights was then applied through a system of wires and pulleys, and once the flap was actuated, the resulting

displacements were measured. From the 11.7° displacement in the unloaded situation, the deflection decreased down to 10.8° when 10 kg were applied. Although it does not correspond to the final objective of 40 kg, the results look promising and we expect an ultimate value still above the $\pm 4^\circ$ minimum requirement.

4.2 Future works

The analyses conducted so far still have room for improvement both in the computer based aspect and in the practical side. The computational fluid dynamic simulation implemented does not take into account pitch rotation of the airfoil as well as possible plunging; these features will be added taking advantage of a further refined dynamic mesh and additional user defined functions able to describe in detail the complete motion of the airfoil. Also, a porous region will be added in the gap between the flap and the main block in order to avoid mass flow and thus perfectly emulate the real aerodynamic conditions. Quality wise, mesh surrounding the flap will be refined and adopt a layout which further decreases numerical error.

Multibody dynamic analysis with DYMORE will be equipped with additional details to better resemble the real case; these consists of the built-in twist angle and an added lifting line along the flap to observe the aerodynamic loads generated over the surface. Once the whole rotor layout will be defined, forward flight condition will be simulated and internal forces as well as external solicitations measured.

The pulling test to verify the flap deflection in rotating environment will be conducted up to its ultimate value of 40 kg; also, in order to decrease the centrifugal force acting on the deflecting surface, the total flap mass will be decreased from the current 20 g to 10 g. An additional verification of the effects of centrifugal force will be conducted on the actuator as well

but, due its relatively high mass, a proper pulling test will be impossible to implement. Being the final load requirement 400 kg, an Instron machine will be exploited and the tension applied to a dummy actuator so as to avoid any damage to the piezoceramic stack due to the force applied.

Finally, a detailed contact analysis will be carried out with NASTRAN to observe the stresses generated within the link mechanism due to the centrifugal force. Each component will be considered and analyzed to verifying whether the occurring stresses pose a risk for structural integrity and excessive wearing during the device actuation.

Reference

- [1] Rita, A., McGarvey, J.H., Jones, R., “Helicopter Rotor Isolation Evaluation Utilizing the Dynamic Antiresonant Vibration Isolator”, Journal of the American Helicopter Society, Volume 23, January 1978.
- [2] Konstanzer, P., Enenkl, B., Aubourg, P., Cranga, P., “Recent Advances in Eurocopter’s Passive and Active Vibration Control”, American Helicopter Society 64th Annual Forum, Montreal, Canada, May, 2008.
- [3] Paselk, Robert A., “Development of an Environmental Design and Test Guide for Army Rotary Wing Aircraft”, Los Angeles Aircraft Division, Rockwell International Corporation, February 1976.
- [4] Vincent, A.H., Lewis Cure, R.W., “Bifilar Vibration Dampers”, patent US 3932060, January 1976.
- [5] Desjardins, R.A., Hooper, W.E., “Antiresonant Rotor Isolation for Vibration Reduction”, Journal of the American Helicopter Society, January 1980.
- [6] Ahci, E., Rupert, P., Straße, W. M., “Structural Design, Optimization and Validation of the Integrated Active Trailing Edge for a Helicopter Rotor Blade”, The American Helicopter Society 64th Annual Forum, Montreal, April 2008.
- [7] Lee, T., Chopra, I., “Design of Piezostack-driven Trailing Edge Flap Actuator for Helicopter Rotors”, Smart Materials and Structures, February 2001.
- [8] Walz, C., Chopra, I., “Design and Testing of a Helicopter Rotor Model with Smart Trailing Edge Flaps”, Structural Dynamics and Materials Conference, Adaptive Structures Forum, April 1994.
- [9] Natarajan, B., “Structural Analysis and Actuation Tests of an Active Trailing-edge Flap (ATF) Blade for Helicopter Vibration Control 2013”, Seoul National University, Master’s Thesis, School of Mechanical and Aerospace Engineering, Seoul National University, Seoul, February 2013.
- [10] Kang, J.P., Eun, W.J., Lim, J.H., Visconti, U., Shin, S.J., “Design Improvement of Smart Active Trailing-edge Flap for Rotating Test”, 56th AIAA/ASCE/AHS/ASC Structures, Structural Dynamics and Materials Conference, Kissimmee, January 2015.
- [11] Mainz, H., van der Wall, B., Leconte, P., Ternoy, F., Mercier des Rochettes, H.,

“ABC Rotor Blades: Design, Manufacturing and Testing”, 31th European Rotorcraft Forum, Florence, September 2005

- [12] Li, L., Padthe, A.K., Friedmann, P.P., Quon, E., Smith, M.J., ”Unsteady Aerodynamics of an Airfoil/Flap Combination on a Helicopter Rotor Using Computational Fluid Dynamics and Approximate Methods”, 65th American Helicopter Society Annual Forum, Grapevine, Texas, May 2009.
- [13] Abbot, I. H., and Von Doenhoff, A. E., *Theory of Wing Sections*, Dover Publications, Inc., New York, 1959.
- [14] Standish, K.J., van Dam, C.P., “Aerodynamic Analysis of Blunt Trailing Edge Airfoils”, *Journal of Solar Energy Engineering*, November 2003.
- [15] Berkman, M.E., Sankar, L.N., Berezin, C.R., Torok, M.S., “Navier-Stokes/Full Potential/Free-Wake Method for Rotor Flows”, *Journal of Aircraft*, September-October 1997.
- [16] Lohner, R., “Finite Elements in CFD: What Lies Ahead”, *International Journal for Numerical Methods in Engineering*, September 1987.
- [17] Pearce, D.G., Stanley, S.A., Martin F.W., Gomez, R.J., Le Beau, G.J., Buning, P.G., Chan, W.M., Chiu, T., Wulf, A., Akdag, V., “Development of a Large Scale Chimera Grid System for the Space Shuttle Launch Vehicle”, 31th Aerospace Sciences Meeting & Exhibit, January 1993.
- [18] Tannehill, J.C., Anderson, D.A., Pletcher, R.H., “*Computational Fluid Mechanics and Heat Transfer*”, Hemisphere Publishing Corporation, 1984.
- [19] Spalart, P., Allmaras, S.R., “A One Equation Turbulence Model for Aerodynamic Flows”, 30th Aerospace Sciences Meeting & Exhibit, January 1992.
- [20] Mavriplis, D.J., “Revisiting the Least-Squares Procedure for Gradient Reconstruction on Unstructured Meshes”, *American Institute of Aeronautics and Astronautics*, 2003.
- [21] Patankar, S., “*Numerical Heat Transfer and Fluid Flow*”, , Hemisphere Publishing Corporation, 1980
- [22] Anonymous, Dymore Solutions, User’s manual.
- [23] Batina, J.T., “Unsteady Euler Algorithm with Unstructured Dynamic Mesh

for Complex-aircraft Aerodynamic Analysis”, American Institute of Aeronautics and Astronautics, 1990.

- [24] Dvorak, G., “Micromechanics of Composite Materials”, Springer Edition, 2002.
- [25] Press, W.H., Teukolsky, S.A., Vetterling, W.T., Flannery, B.P., “Numerical Recipes. The Art of Scientific Computing”, Cambridge University Press, 2007.
- [26] Kang, J.P., ‘Design Improvements of the Smart Active Trailing-edge Flap (ATF) for Rotating Test’, Seoul National University, Master’s Thesis, School of Mechanical and Aerospace Engineering, Seoul National University, Seoul, February 2015.
- [27] Chopra, I., “Recent Progress on the Development of a Smart Rotor System”, Adaptive Structures, Eleventh International Conference, Nagoya, 2000.

국문초록

본 논문은 회전익기의 로터에서 발생하는 진동 하중을 줄이기 위한 연구로 능동형 뒷전 플랩이 설치된 축소형 블레이드, SNUF (Seoul National University Flap) 제작을 위한 여러가지 해석 및 실험에 관한 것이다. 플랩은 압전재료로 제작된 작동기에 의해 구동되며 로터가 발생시키는 주요한 하중(primary disturbances)을 감소시키기 위하여 부차적인 진동을 발생시킨다. CFD 해석을 통하여 플랩의 힌지모멘트를 계산하였고 이를 통하여 목표하는 진동수와 각도로 선택한 작동기에 의해 플랩이 구동할 수 있는지 검증하였다. 작동기의 특성과 힌지모멘트를 비교하여 현재의 작동기로 플랩을 정상적으로 구동할 수 있음을 보일 수 있었다. 더 나아가, 다물체 동역학 해석프로그램인 DYMORE를 이용하여 블레이드에 공력과 원심력이 작용하였을 때 작동기의 힘과 변위의 관계를 반영하여 플랩의 구동 범위가 목표하는 범위를 만족하는지 해석하였다. 프로그램을 이용한 해석 외에도 이론에 의한 정식화 및 현재 시스템의 동역학적 해석을 이용한 검증을 수행하였다. 또한 플랩의 벤치테스트를 수행하여 플랩의 작동 방향의 수직인 방향으로 원심력이 작용할 때 플랩의 구동을 관찰하였다. 지금까지 하중을 아직 실제 작용하는 원심력까지 부과하지는 못했지만 원심력에 의한 하중이 증가함에 따라서 플랩의 작동 범위가 줄어드는 것을 관찰할 수 있었다. 하지만 이 줄어드는 정도는 적어서 목표하는 작동 범위를 만족하였다.

주요어: 지능형 능동 뒷전 플랩(ATF), 압전재료 작동기, 진동 제어, 지능형 로터 블레이드

학번 : 2014-22147



Attribution–NoDerivs 2.0 KOREA

You are free to :

- **Share** — copy and redistribute the material in any medium or format
- for any purpose, even commercially.

Under the following terms :



Attribution — You must give [appropriate credit](#), provide a link to the license, and [indicate if changes were made](#). You may do so in any reasonable manner, but not in any way that suggests the licensor endorses you or your use.



NoDerivatives — If you [remix, transform, or build upon](#) the material, you may not distribute the modified material.

You do not have to comply with the license for elements of the material in the public domain or where your use is permitted by an applicable exception or limitation.

This is a human-readable summary of (and not a substitute for) the [license](#).

[Disclaimer](#) 

공학석사학위논문

Transient Flow Analysis and Static Bench Measurements for an Active Trailing-Edge Flap

회전익기 진동제어를 위한 능동뒷전 플랩의

비정상 유동해석과 테스트 벤치를 이용한

시험

2016년 2월

서울대학교 대학원

기계항공공학부

Umberto Visconti

Transient Flow Analysis and Static Bench Measurements for an Active Trailing-Edge Flap

회전익기 진동제어를 위한 능동뒷전 플랩의 비정상 유동해석과 테스트 벤치를 이용한 시험

지도교수 신 상 준

이 논문을 공학석사 학위논문으로 제출함

2016년 2월

서울대학교 대학원

기계항공공학부

Umberto Visconti

Umberto Visconti의 석사학위논문을 인준함

2016년 2월

위원장 이수근 (인)
부위원장 신상준 (인)
위원 이관홍 (인)

Abstract

In this dissertation, several analyses over SNUF (Seoul National University Flap), a small-scaled prototype equipped with an active trailing edge flap, were conducted in order to achieve vibratory load reduction in the rotor system. The device consists of a piezoelectric actuator driven flap which generates secondary vibrations aimed at dampening the primary disturbances. Predictions of the hinge moment coefficient were retrieved through CFD (computational fluid dynamics) analyses in order to verify the capability of the chosen actuator to ensure a smooth and efficient displacement of the flap and therefore the achievement of the designated objective. The results showed good compromises between the actuator characteristics and the loads generated over the flap surface. Furthermore, a multibody dynamic analysis was implemented with DYMORE to obtain a holistic view of the forces and the displacements acting within the device when external aerodynamic loads and centrifugal force occur. Outcomes from the code were validated with theory formulation and thus are considered a reliable description of the dynamics of the system. In addition to that, a pulling test was conducted so as to observe any likely decrease in the deflection range once the centrifugal force acts in a direction perpendicular to the flap angular displacement. Although the ultimate load applied does not coincide with final objective, the limited shrinkage of the deflection span suggests a definitive result still satisfying the requirements.

Keywords: Active Trailing-edge Flap (ATF), piezoelectric actuator,
vibration control, active rotor blade

Student number: 2014-22147

Table of contents

List of figures	IV
List of tables	VII
I. Introduction	1
1.1 Backgrounds and motivation	1
1.2 Vibrations suppression methods	2
1.3 Previous studies	6
1.4 Objectives and overview of the dissertation	7
II. Theoretical background	10
2.1 Present research review	10
2.2 Computational domain meshing	11
2.3 Solver	15
2.4 Steady case	17

2.5 Transient case	20
2.6 DYMORE model	22
2.7 Micromechanics to estimate the properties of the composite materials used	25
2.8 Model features	27
2.9 Pulling test implementation	31
III. Numerical and experimental results	33
3.1 Steady state results	33
3.2 Transient state results	43
3.3 DYMORE centrifugal load analysis	51
3.4 DYMORE flap deflection analysis	54
3.5 DYMORE aerodynamic loads analysis	56

3.6 Pulling test results	62
IV. Conclusion and future works	65
4.1 Conclusion	65
4.2 Future works	66
Reference	68
국문초록	71

List of Figures

Figure 1. 1 Aerodynamic issues in forward flight-----	2
Figure 1. 2 SARIB system -----	3
Figure 1. 3 ACSR application to Agusta-Westland-----	4
Figure 1. 4 Individual blade control-----	5
Figure 1. 5 Active trailing edge flap -----	6
Figure 1. 6 Previous version of the mesh in use -----	9
Figure 2. 1 Mechanism in use. -----	11
Figure 2. 2 Mesh used by Li et al. (2011)-----	13
Figure 2. 3 Detail of the used mesh. -----	14
Figure 2. 4 Drawing of the mechanism-----	24
Figure 2. 5 DYMORE schematic model -----	24
Figure 2. 6 Relationship among the block force, input voltage, and stroke -----	28
Figure 2. 7 Hinge moment evolution -----	30
Figure 2. 8 Pulling test test-bed-----	32
Figure 3.1 Drag coefficient with no flap deflection-----	34
Figure 3.2 Lift coefficient with no flap deflection -----	34
Figure 3.3 Moment coefficient with no flap deflection. -----	35
Figure 3.4 Drag coefficient comparison-----	36
Figure 3.5 Lift coefficient comparison -----	37

Figure 3.6 Moment coefficient comparison -----	37
Figure 3.7 Refined mesh-coarse mesh comparison for drag -----	39
Figure 3.8 Refined mesh-coarse mesh comparison for lift -----	39
Figure 3.9 Refined mesh-coarse mesh comparison for moment-----	40
Figure 3.10 Absolute difference between the coarse and refined mesh---	41
Figure 3.11 Hinge moment trend according to Walz and Chopra-----	42
Figure 3.12 Hinge moment comparison with 10° flap deflection -----	43
Figure 3.13 Drag coefficient at 2 Hz flap actuation-----	44
Figure 3.14 Lift coefficient at 2 Hz flap actuation -----	44
Figure 3.15 Moment coefficient at 2 Hz flap actuation -----	45
Figure 3.16 Drag coefficient at 20 Hz flap actuation -----	45
Figure 3.17 Lift coefficient at 20 Hz flap actuation-----	46
Figure 3.18 Moment coefficient at 20 Hz flap actuation.-----	46
Figure 3.19 Drag coefficient at 65 Hz flap actuation -----	47
Figure 3.20 Lift coefficient at 65 Hz flap actuation.-----	47
Figure 3.21 Moment coefficient at 65 Hz flap actuation-----	48
Figure 3.22 Hinge moment coefficient at 2 Hz flap actuation -----	49
Figure 3.23 Hinge moment coefficient at 20 Hz flap actuation.-----	50
Figure 3.24 Hinge moment coefficient at 65 Hz flap actuation -----	50
Figure 3.25 Flap deflection as a function of the moment arm length (predicted) -----	51

Figure 3.26 Internal forces at the blade root.-----	53
Figure 3.27 Internal forces at the blade tip -----	54
Figure 3.28 Flap deflection at 2 Hz actuation-----	55
Figure 3.29 Flap deflection at 20 Hz actuation. -----	55
Figure 3.30 Flap deflection at 65 Hz actuation. -----	56
Figure 3.31 Total airloads over a single blade -----	57
Figure 3.32 Airloads at the blade root -----	58
Figure 3.33 Airloads at the blade tip. -----	59
Figure 3.34 Flap deflection at 2 Hz with airloads -----	60
Figure 3.35 Flap deflection at 20 Hz with airloads -----	60
Figure 3.36 Flap deflection at 65 Hz with airloads -----	61
Figure 3.37. Internal forces at the blade root in aerodynamic conditions -----	62
Figure 3.38 Flap deflection under the dead loads -----	63
Figure 3.39 Flap deflection under the dead loads [detail] -----	64

List of Tables

Table 2.1 Material properties-----	27
Table 2.2 Chebyshev coefficients -----	31
Table 3.1 Aerodynamic analysis conditions-----	33

I. INTRODUCTION

1.1 Backgrounds and motivation

Helicopters constitute a versatile means of transportation able to achieve tasks otherwise difficult to accomplish with fixed-wing vehicles such as vertical take-off and hovering. In spite of these unique capabilities, they also encounter different issues, especially in fast forward and descent flight conditions. Among the different causes, the absence of a symmetry axis results in a different flow speed between the advancing and the retreating side of the rotor, as in Fig. 1.1, whereas the perturbations which arise due to the interference among the overlapping blade wakes generate a relevant amount of noise and vibrations [1]. As a consequence, anytime comfort is a major aspect of the mission being conducted, such as VIP flights or non-urgent medical transportation, the proximity of the passengers to the vibrations source and the coincidence of the frequency span generated with human perceivable range negatively affect the flight experience. [2]

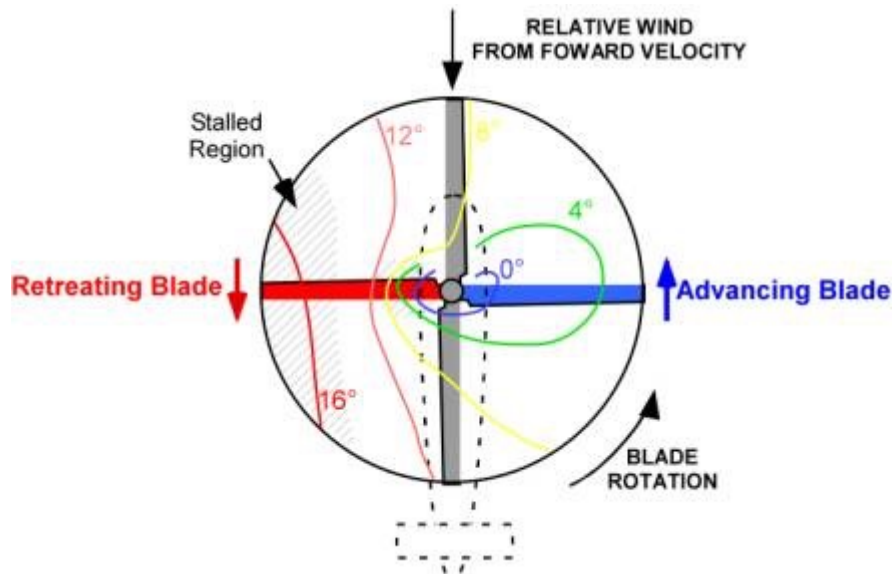


Figure 1.1 Aerodynamic issues in forward flight

1.2 Vibrations suppression methods

The rotor induced vibrations, other than being a nuisance, also pose a harm to structural integrity of the components which may have their lifespan shortened due to the continuous stress they endure [3]. So far, the traditional approach to the issue was represented by several devices placed on the hub and aimed at dampening the transmission of vibrations from the rotor to the fuselage. The most common concept, denominated DAVI, consists of a mass, added to the shaft, whose oscillating movement is amplified thanks to interconnected pins [4] so as to be able to counteract and eliminate external excitations. Further developments include ARIS system and SARIB[®] [2], depicted in Fig. 1.2, which still exploit, in a different way, hydraulic or mechanical system to implement vibration load dampening. All the above solutions, despite succeeding in their goals, showed major disadvantages

such as increased drag, due to the system bulkiness and weight, and single frequency tuning which implies that all the other vibrations flow untouched. In fact, aside from 1/rev frequency, the remaining pN/rev harmonics, where N is the number of blades and p an integer, are not cancelled out but transmitted undampened to the fuselage [5].



Figure 1.2 SARIB system

On the other hand, due to above mentioned limitations, the concept of an active control is increasing its popularity due to a higher adaptability and greater efficiency in reducing the vibrations generated. Active methods are usually classified into two groups: one aims at attenuating the vibration directly in the fuselage while the second attempts to prevent it at the origin.

The former, represented in Fig. 1.3, is denominated Active Control of Structural Response (ACSR) and it is enacted placing vibration sensors in key locations of the fuselage [6]. Once the amount of vibration is sensed, the device will instruct actuators located throughout the structure to generate a specifically designed vibration necessary to alleviate the primary disturbance.



Figure 1.3 ACSR application to Agusta-Westland

The latter instead, focuses its attention on the rotor and it is further divided in two categories. The Higher Harmonic Control (HHC) still takes advantage of sensors distributed on the frame to register the vibrations encountered but then makes use of the non-rotating swashplate to input higher harmonics on the rotor blades; despite proving to be successful, widespread use of this solution is not possible due to weight penalties and the high actuation power required.

On the other hand, Individual Blade Control (IBC), shown in Fig. 1.4, implementation proved to be more successful. The idea still consists of secondary loads generated on purpose to compensate the primary source of vibration; while originally electro-hydraulic systems were exploited, the use of piezo-electric actuators [7] has become more and more common. The major advantage is the possibility to excite the blade at any frequency and thus, be able to erase any vibration, regardless its mode. At first, pitch actuation was applied at the blade root (off-blade actuation) as a substitution of the conventional control rods connected to the swashplate.

After that, thanks to further developments of piezoelectric materials, fibers of the latter were embedded in the blade itself so as to create a morphing structure, denominated Active Twist Rotor (ATR), able to twist along the blade span. Despite the good results achieved during experimentation, the high power required for its implementation plunged its diffusion. Finally, a third solution with low energy requirements and good outputs was conceived: the Active Controlled trailing-edge Flap (ACF). This implementation case consists of a stiff blade equipped with a moving flap driven by a piezoelectric actuator which modifies the aerodynamic of the blade and showed effective vibrations reduction, as portrayed in Fig. 1.5.

Generally, the system includes data acquisition along power transmission; once the sensors report the state of rotor blade, the incoming values are analyzed and a signal is transmitted to the actuators driving the flap which will react in the best possible way to eliminate the produced vibration.

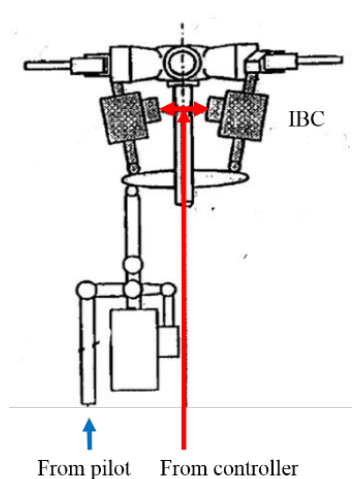


Figure 1.4 Individual blade control

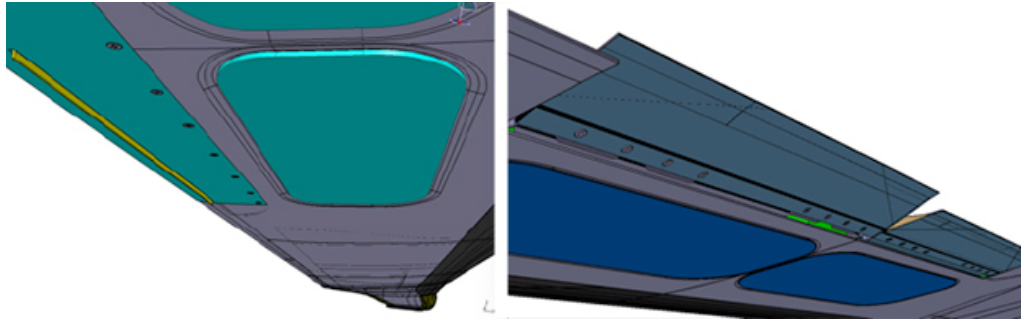


Figure 1.5 Active trailing edge flap (Agusta-Westland)

1.3 Previous studies

ACF is so far one of the most successful solutions adopted for vibrations suppression; a number of different researches have already been conducted, both on small and full scale, and the results obtained proved to be satisfactory. Walz and Chopra [8] conceived a bimorph flap actuation system to be placed within the fixed frame which would deflect and thus move the flap it is connected to. Although no rotating test was conducted, the mechanism in use shows great versatility and, what is more, room for improvement once design is perfected. Konstanzer, Enenkl, Aubourg and Cranga [2] instead applied the active trailing edge flap to a full scale rotor and measured the reduction in vibration caused by 4/rev hub loads. Three identical flap units, driven by two piezo-ceramic actuator each, were installed on all the rotor four blades and sensors were placed to monitor different parameters; actuation of the device on an experimental flight contributed to an overall reduction of vibrations which amounts to 90% of its original value. In conclusion, ACF is a promising technology which already demonstrated its

capabilities and versatility and it is apt to be adopted for a wider range of applications in future.

1.4 Objectives and overview of the dissertation

In spite of the different efforts to dampen the vibrations generated during flight, we are still far from a complete reduction of the disturbances which occur due to the complex dynamics which characterize helicopters. This happened due to the incapability of passive methods to adapt to the different flight conditions which may raise during operations and, as far as active methods are concerned, to the intrinsic difficulties typical of a closed loop actuation which requires perfect feedback to customize the response. On the other hand, the introduction of piezo electric actuators outstandingly improved the results obtained; in fact, the reduced weight coupled with high power density proved to be extremely useful in components such as rotors, whose stability is very sensitive to any additional load. What is more, these devices enable a simplification of the layout of the whole system, whose complexity is still one of the major drawbacks in the full exploitation of active methods.

As consequence, the development of a small-scaled blade equipped with a trailing edge active flap, denominated SNUF, driven by a piezoceramic actuator was conducted in order to be able to dampen the vibratory load. The final implementation will consist of a two blade rotor, each of those equipped with a movable surface placed at 75% of the whole length blade and driven by a CEDRAT actuator.

This dissertation concerning the design improvements is articulated in three fundamental points:

- hinge moment estimation
- implementation of a multibody analysis
- conduction of a pulling test

CFD analysis consists of meshing the chosen NACA 0015 airfoil surroundings in order to simulate the airflow the blade would encounter and to estimate the airloads generated on the surfaces. Unlike the previous design shown in Fig. 1.6, the flap is kept detached from the airfoil main body. Specifically, hinge moment coefficient is the value we mostly focus on so as to evaluate the amount of the pressure distribution over the flap which could obstacle a smooth actuation of the flap.

Multibody dynamic analysis is implemented thanks to the capabilities of DYMORE which couples the structural properties of blade and mechanism link with the external solicitations being the centrifugal force and the aerodynamic loads

Pulling test includes the design and manufacturing of a specifically conceived test bed aimed at the actuation of the flap in a vertical position. This, allows the application on the flap of different sets of weights which simulate the loads generated when the blade rotates; once the flap is actuated, the resulting deflection are measured in order to observe the decrease in deflection range compared to the unloaded situation.

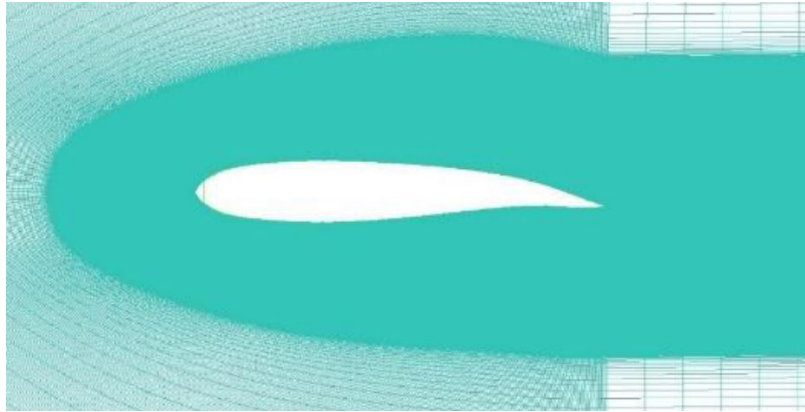


Figure 1.6 Previous version of the mesh in use

II. THEORETICAL BACKGROUND

2.1 Present research review

In the design of the active trailing edge flap, static bench test was thought to be the most important step to be completed during the analysis process of the mechanism but once the first version of the test bed was manufactured, the flap deflection could not meet the requirements [9] probably due to unexpected friction in the link mechanism. The issue was approached increasing the number of actuators which would drive the flap in order to provide the flap with a higher force. Unfortunately, the accumulation of actuators did not concur to a more efficient motion as other factors such as interaction between the actuators and misalignment came into play and reduced the overall capability of the actuators. As a consequence, instead of stacking a higher number of actuators which would affect the overall weight without wreaking benefits on the deflection requirements, the APA 200L piezoelectric actuator in use was substituted.

More importantly, whereas previously blade structural analysis had been completed before choosing the actuator, thus restraining the choice for actuators selection and layout, the implementation flow was inverted and an actuator which could deflect the flap in the whole range required was selected first and then the encompassing blade design, as visible in Fig. 2.1, was conducted.

As a consequence, a new actuator was selected [10], specifically APA 1000L, in order to obtain a sufficient deflection during non-rotating test which would be inevitably reduced [11] once aerodynamics in the whirl tower is added. Also, static load analyses were implemented on the actuator to verify whether it could withstand centrifugal forces and blade design was renewed. Increased size of the newly-selected actuator meant

an increase in length and width of the blade and built-in twist was applied throughout the whole length to enhance structural integrity.

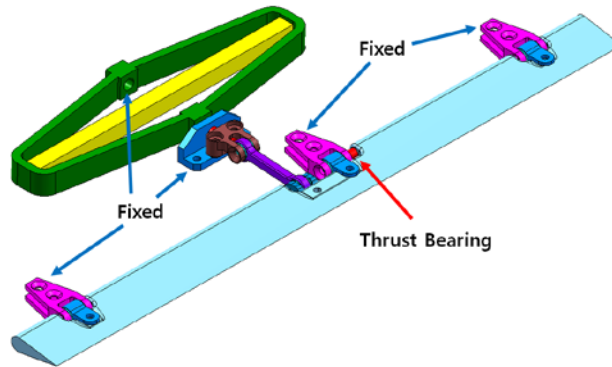


Figure 2.1 Mechanism in use

2.2 Computational domain meshing

A momentous aspect in the design of the ATF is the estimation of the hinge moment generated by external forces. In fact, during the blade rotation a distributed load generates on the flap surface and obstacles the smooth oscillation of the device; thus, the vibrations suppression will only achieved once the mechanism is able to counteract and overcome the aerodynamic load insisting on the flap.

The NACA 0015 airfoil geometry was split into two blocks, as already achieved by Li et al. [12] in Fig. 2.2, to adjust to the requirements for calculation in transient mode; a main block, constituting 80% of the whole length, is kept still and a detached flap, represented in Fig. 2.3, instead deflects according to the imposed function. Slotted flaps, as the configuration is denominated [13] when a gap exists between the main portion and the deflected flap, increase the effectiveness of the airfoil thanks to an increase in camber and chord. Nonetheless, in spite of the

relevant gain in aerodynamic performance, the complex geometry of the layout does not allow a reliable prediction of pressure loads and aerodynamic coefficients are either retrieved experimentally or through CFD simulation.

As in our case experimental measurements were not available, estimation of the load acting on the airfoil was implemented through a computational fluid dynamics analysis: ICEM was chosen as the meshing software and ANSYS FLUENT as the solver. The above analysis was articulated in two different stages: first, static measurements were conducted on the flap deflected by 10° , an angle higher than the expected operating range, to include a safety factor in the sizing of the mechanism link. Secondly, a transient analysis, where the flap actuation frequency spanned from 0 Hz to 65 Hz (2/rev), was enacted to retrieve realistic values of the aerodynamics coefficients occurring during the ATF utilization.

C-shaped computational domain was chosen over O-shaped domain as the sharp trailing edge would force the adjacent triangular elements to have $180 - \frac{\alpha}{2}$ angles, α being the flap internal angle; in such case the enclosed edge is preferred to run parallel to the wall, as it would happen with a C-shaped domain, rather than perpendicular, as in the O-shaped case [14]. What is more, C-shape inherent ability to capture wake makes it a preferential choice when aerodynamic coefficients are needed; still for wake issues, the domain size was set roughly 20 times the airfoil chord to prevent boundaries from influencing the flow in the vicinity of the airfoil [15]. Although the simple geometry does not require a complex meshing layout, triangular unstructured mesh was selected as the most flexible and suitable in case of dynamic mesh, where remeshing and smoothing processes are applied during the computation to maintain high cell quality [16]. In addition to that, hexahedral elements were placed along the airfoil

to better capture and define the boundary layer and to constitute a medium between the physical walls and the triangular mesh. The latter aspect is also the reason why hexahedral cells are present along the outer walls of the domain; also, without this precaution, negative volume issues are bound to occur during the flap actuation. Given that accuracy is only required in the surroundings of the airfoil, a coarse mesh was drawn in the majority of the domain and only refined in proximity of the walls. The total number of elements comprises 8506 triangular cells and 1810 hexahedral prisms arranged in 5 layers; in fact, a higher number of layers would have filled the gap between the airfoil main block and the flap, thus decreasing the quality of computation in a fundamental region for the objectives of the analysis.

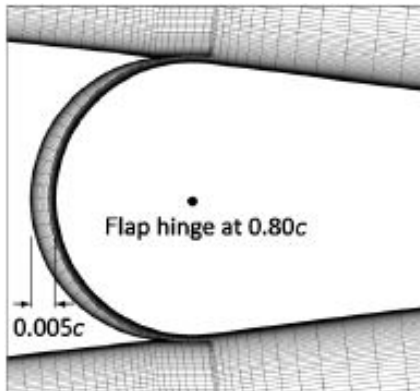


Figure 2.2 Mesh used by Li et al. (2011)

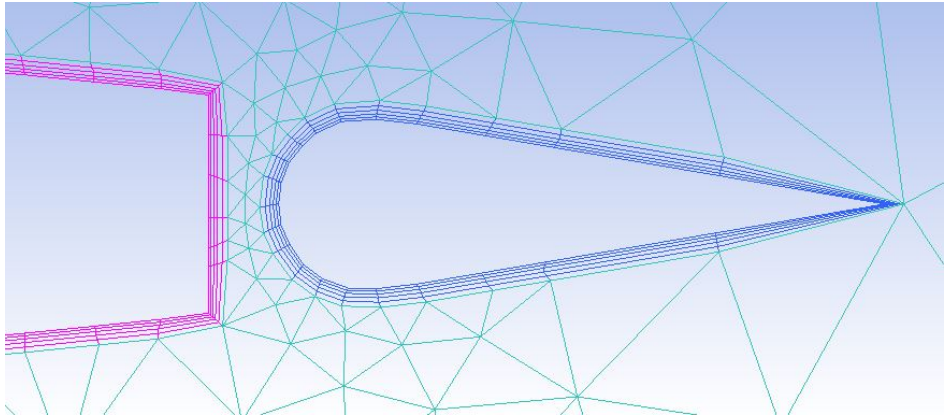


Figure 2.3 Detail of the used mesh

The selected meshing approach, denominated Patch Independent, takes advantage of the Octree method, a top-down approach where the mesh is first generated and then made conformal to the present geometry. This choice allows to start from an extremely coarse web and gradually refine the grid only in the regions requiring a more detailed definition, in our case the flap area and the gap between the latter and the main block of the airfoil [17]. On the contrary, the other available approaches such as Autoblock or Patch Dependent, with the same amount of refinement in the areas of interest, would have generated an excessive number of elements in the whole computational domain. To obtain even and smooth hexahedral elements layers, the quality of the overall mesh has to be improved through alternate cycles of simple and Laplace smoothing, the latter computing the average position of the surrounding nodes to generate a new position of the node of interest. A further step to increase quality of triangular mesh takes advantage of Delaunay circle test: when two cells share a face and the circumcircle of one of the two also encompasses the unshared vertex of the other cell, then faces are swapped [18].

2.3 Solver

ANSYS FLUENT is the solver selected to extract hinge moment and other data from the considered model. Mass, momentum and energy equations are the conservation equations solved by ANSYS FLUENT and involved in the flow which characterizes our model.

Continuity equation in integral form is defined as

$$\frac{\partial}{\partial t} \int_V \rho dV + \oint \rho \mathbf{v} \cdot d\mathbf{A} = 0 \quad (1)$$

Given that no mass is added to the continuous phase, the right term is set to 0.

Momentum equation in integral form is instead defined as

$$\begin{aligned} \frac{\partial}{\partial t} \int_V \rho u dV + \oint [\rho \mathbf{v} u + p \hat{i} - \tau_{xi}] \cdot d\mathbf{A} &= 0 \\ \frac{\partial}{\partial t} \int_V \rho v dV + \oint [\rho \mathbf{v} v + p \hat{j} - \tau_{yi}] \cdot d\mathbf{A} &= 0 \end{aligned} \quad (2)$$

As gravity does not contribute significantly and no external force is applied to our model, no term on the right side of the equation is considered in the computation. On the other hand, due to viscosity, shear stress is part of the flow physics and it is described through the stress tensor as follows

$$\bar{\bar{\tau}} = \mu \left[(\nabla \bar{\mathbf{v}} + \nabla \bar{\mathbf{v}}^T) - \frac{2}{3} \nabla \cdot \bar{\mathbf{v}} \mathbf{I} \right] \quad (3)$$

The choice of ideal compressible fluid case implies the addition of density as a further variable in the model, which means an additional equation, energy conservation equation, is added to the model description:

$$\frac{\partial}{\partial t} \int_V \rho E dV + \oint [\rho \mathbf{v} E + p \mathbf{v} - \tau_{ij} v_j] \cdot d\mathbf{A} = 0 \quad (4)$$

where no heat flux or work done by body forces is considered.

The viscosity model which best fits the situation is the Spalart-Allmaras model [19] which derives from the Boussinesq approach and does not require a burdensome computation when turbulent viscosity is investigated.

$$\begin{aligned} \frac{\partial}{\partial t}(\rho\tilde{\nu}) + \frac{\partial}{\partial x_i}(\rho\tilde{\nu}u_i) = G_\nu + \dots \\ \dots + \frac{1}{\sigma_{\tilde{\nu}}} \left[\frac{\partial}{\partial x_j} \left\{ (\mu + \rho\tilde{\nu}) \frac{\partial \tilde{\nu}}{\partial x_j} \right\} + C_{b2\rho} \left(\frac{\partial \tilde{\nu}}{\partial x_j} \right)^2 \right] - Y_\nu + S_{\tilde{\nu}} \end{aligned} \quad (5)$$

This model, usually exploited for low Reynolds numbers, consists of a single equation describing the transport of kinematic viscosity and it is defined by eight constants.

As mentioned, the flow is described as compressible and therefore it is characterized by total pressure and total temperature as follows

$$\begin{aligned} \frac{p_0}{p} &= \left(1 + \frac{\gamma-1}{2} M^2 \right)^{\frac{\gamma}{\gamma-1}} \\ \frac{T_0}{T} &= 1 + \frac{\gamma-1}{2} M^2 \end{aligned} \quad (6)$$

where pressure specific heat is assumed constant given that the model does not encounter notable temperature variations.

Density is thus computed:

$$\rho = \frac{P_{op} + P}{\frac{R}{M_w} T} \quad (7)$$

The external boundary of the C shaped computational domain is divided in a forward facing half and in a rear facing half. Both are characterized by pressure far field boundary conditions, where the stream is modeled at infinity and the flow direction is changed according to the angle of attack desired for the airfoil. While gauge pressure and temperature are kept at standard conditions, the Mach number is modified to simulate the velocity

of the airfoil section where the active flap is placed. The airfoil main block and the flap are instead considered as wall, which implies non penetrability of mass, momentum and energy flow

$$\mathbf{u} \cdot \mathbf{n} = \nu^B \cdot \mathbf{n} \quad (8)$$

Also, due to viscosity, no-slip condition is implemented and thus, the fluid sticks to the wall.

2.4 Steady case

One of the most important aspects of Navier-Stokes equations is the non-linearity which obstacles any possibility to solve them analytically and forces the application of a computational scheme to the discretized form of the equations into account. During the solution of the problem, the default ANSYS FLUENT process consists of computation of a scalar per each cell and storage of the cell center value; nonetheless, convective terms require the presence of cell face values. As a consequence the generic value at cell face is computed as follows

$$\Phi_f = \Phi + \nabla \Phi \cdot \vec{r} \quad (9)$$

starting from the generic value at cell center.

This approach is especially useful as our computation requires at least second order accuracy for both diffusive and convective terms; while the former does not pose any problem, the latter requires a specific approach which makes use of Taylor series expansion of cell centered value about the cell centroid. Second order accuracy is not strictly necessary in situations where the flow is aligned with the mesh, as a hexahedral mesh, but the choice of a triangular grid makes the use of second order upwind necessary. Its general formulation is as stated

$$\Phi_{f,SOU} = \Phi + \nabla \Phi \cdot \vec{r} \quad (10)$$

Gradient is computed using the Least Squares Cell-Based Gradient evaluation [20] which assumes the solution varies linearly between two cell centers

$$(\nabla\Phi)_{cell0} \cdot \Delta r_1 = (\Phi_{cell1} - \Phi_{cell0}) \quad (11)$$

The overdetermined system which arises from writing an equation for each cell surrounding the first cell is then solved exploiting the Gram-Schmidt process; the resulting weights are then applied to the scalar difference vector.

Discretization of momentum exploits the procedure applied to the generic scalar transport equation, where velocity components u and v , respectively along x and y direction, as we are in a 2D geometry, substitute the generic quantity.

$$\begin{aligned} a_p u &= \sum_{nb} a_{nb} u_{nb} + \sum p_f A \cdot \hat{i} + S \\ a_p v &= \sum_{nb} a_{nb} v_{nb} + \sum p_f A \cdot \hat{j} + S \end{aligned} \quad (12)$$

Discretization of continuity equation is accomplished using the mass flux through the cell face

$$\sum_f^{N_{faces}} J_f A_f = 0 \quad (13)$$

A combination between continuity equation and definition of mass flux is also exploited as a further condition exploited to describe and solve the flow problem into account. The SIMPLE-Consistent scheme (SIMPLEC) [21] applied calculates the new mass flux with a correction applied

$$J_f = J_f^* + d_f (p'_{c0} - p'_{c1}) \quad (14)$$

where coefficient d_f is defined as a function of momentum equation linearized coefficients

$$d_f = \sqrt{a_p - \sum_{nb} a_{nb}} \quad (15)$$

to improve convergence.

A further method to improve convergence during the problem solving is the use of the under relaxation factor which aims at reducing the variation of the generic scalar between one iteration and the following.

$$\Phi = \Phi_{old} + \alpha \Delta \Phi \quad (16)$$

The adjusted value will be then between $\Phi_{i,j}^k$ and $\Phi_{i,j}^{k+1}$.

Although Navier-Stokes equations do not present analytical solution, we can exploit theory to obtain an estimation of the values we will retrieve. This especially happens with hinge moment, where, along with CFD analysis, the algorithm formulated by Walz and Chopra [8] proves to be helpful: nonetheless, as it was originally conceived for a three-dimensional case, we had to simplify it to our two-dimensional model where no loss is considered.

Section hinge moment was defined as:

$$h = \frac{1}{2} \rho (\Omega r)^2 c_f^2 C_h \quad (17)$$

If integrated spanwise it results:

$$H = \int_{R_1}^{R_2} h dr = \int_{R_1}^{R_2} \frac{1}{2} (\Omega r)^2 c_f^2 C_h dr = \frac{1}{2} \rho (\Omega c_f)^2 C_h \frac{1}{3} (R_2^3 - R_1^3) \quad (18)$$

The variables present in the latter equation only depend on geometrical data or environmental conditions; hinge moment coefficient instead has to be defined as the linear combination of lift coefficient and flap deflection variations:

$$C_h = C_l \frac{\partial C_h}{\partial C_l} + \delta \frac{\partial C_h}{\partial C_\delta} = C_{l_\alpha} \alpha_{eff} \frac{\partial C_h}{\partial C_l} + \delta \frac{\partial C_h}{\partial C_\delta} \quad (19)$$

The variation of hinge moment coefficient with respect of the lift

coefficient and the deflection angle can be extracted, as a function of the ratio between airfoil chord and flap chord, as in Abbot and Doenhoff [12].

$$\begin{aligned}
\frac{\partial C_h}{\partial C_l} &= -0.01018 - 0.5494 \left(\frac{c_f}{c} \right) + 1.028 \left(\frac{c_f}{c} \right)^2 + \dots \\
&\dots - 0.9934 \left(\frac{c_f}{c} \right)^3 + 0.2270 \left(\frac{c_f}{c} \right)^4 \\
\frac{\partial C_h}{\partial \delta} &= -0.8469 + 0.9833 \left(\frac{c_f}{c} \right) - 0.07663 \left(\frac{c_f}{c} \right)^2 + \dots \\
&\dots + 0.2567 \left(\frac{c_f}{c} \right)^3 - 0.3205 \left(\frac{c_f}{c} \right)^4
\end{aligned} \tag{20}$$

As a consequence, the hinge moment coefficient can be plotted choosing the angle of attack and the flap deflection angle as parameters.

2.5 Transient case

Along with steady case, a transient simulation was also formulated. This consists of the flap oscillation according to an imposed sinusoidal function where frequency and deflection angle are specified by the user; with respect to the static phase, two major differences can be identified: dynamic mesh and choice of the solver.

As mentioned, during the simulation the flap moves symmetrically in the computational domain and, as a consequence, the surrounding cells warp and nodes move. This process, which may create high instabilities in the computation and unrealistic results [22], only involves triangular elements whereas hexahedral cells will only move without any modification in their shape.

Smoothing action contributes to re-establish the mesh equilibrium state which existed before the motion; specifically, the chosen spring-based

smoothing method works as the node displacement due to the imposed motion created a proportional Hook force

$$\vec{F}_i = \sum_j^{n_i} k_{ij} (\Delta \vec{x}_j - \Delta \vec{x}_i) \quad (21)$$

where the terms in the parentheses refer to the displacement of node i and j respectively. The equilibrium is reached once the net force over a node is null; the iterative equation which represents the summation of all the forces acting on the node results as follows:

$$\Delta \vec{x}_i^{m+1} = \frac{\sum_j^{n_i} k_{ij} \Delta \vec{x}_j^m}{\sum_j^{n_i} k_{ij}} \quad (22)$$

The retrieved displacement indicates the new position of the node.

Along with smoothing process, ANSYS FLUENT also includes a remeshing method which is applied anytime the smoothing iteration deteriorates the original mesh in terms of skewness and quality. This is likely especially when the imposed movement is big compared to grid size as our case where flap trailing edge displacement amounts to 0.041 m while triangular mesh size is as small as 0.0008 m. As a matter of fact, once this option is selected, the user is able to define the maximum and minimum value within which the remeshed elements have to fit in order to be accepted.

Both smoothing and remeshing processes are applied to the fluid region of our domain and the chosen “zone parameters” replicate similar values to the original ones, specifically: 0.0008 m as the minimum length scale, 0.1 m as the maximum length scale and 0.7 as the maximum skewness. A rigid body movement is instead selected for flap and surrounding hexahedral elements, where a sinusoidal function whose gravity center is located at the flap hinge (0.11442 m), is chosen as the user defined function to impose.

Along with dynamic meshes, the other major discrepancy between transient analysis steady state one is the algorithm used in the solver. Pressure-Implicit with Splitting of Operators (PISO) [23] still belongs to the SIMPLE family of algorithms exploited in the steady case but performs two further corrections every time new velocities are calculated. Neighbor correction is also defined as a momentum correction given that the calculations required for SIMPLEC algorithm are executed in the pressure-correction equation so that in few loops the velocity values obtained will better satisfy the continuity and momentum equation. The skewness correction instead, enables easier convergence for highly distorted meshes where the relationship between correction of mass flux and pressure difference correction is not accurate and thus requires more iterative cycles to compute the pressure-correction gradient to be used to calculate mass flux.

2.6 DYMORE model

The fluid dynamics analysis is not sufficient to confirm that the whole mechanism, represented in Fig. 2.4, would work properly instead, aerodynamic loads have to be coupled with structural properties and the layout to verify no major displacements or distortions would occur in the rotating environment.

DYMORE is an open-source finite element analysis tool for non-linear elastic multibody systems developed by Prof. O. Bachau at Georgia Institute of Technology. The elements available in the program include, among the others, beams, rigid bodies and a variety of joints and constraints. In the code, static analysis is first applied in order to solve all the motion equation relative to the system in the case where time derivatives are set to zero, once this stage is completed, the deformed

configuration is computed considering the static load applied. The eigenvalues and eigenvectors which result from the analysis constitute the product of the linearization of the dynamic equations of motion.

The joints exploited in the analysis include the revolute joint, where the two elements connected are only allowed to rotate about a specific axis and forbidden to displace in any direction, and prismatic joint where no rotation is allowed and relative displacement only proceeds along a given axis. Revolute joints are included in the push rod mechanism where the linear motion of the actuator has to be converted in the angular displacement of the flap; the prismatic joint, instead, simulates the contraction and dilation of the piezostack actuator at the base of the link mechanism. Two constraints per each blade are used in the model: one is a zero degree of freedom constraint applied at the root of a beam while the second constraint does not have a direct correspondence in the real model but it is only used to grant a 90 degrees intersection between two rigid bodies in the link mechanism. The blade is composed of four different beams: the first and last section will host the fiberglass roving which runs in the front part, chord-wise, of the blade, the second and third block will instead encompass the titanium block designed to hold the actuator. An associated rigid body is exploited to link the blade with the driving mechanism; the said body is connected on the other side with the prismatic joint pushing a set of two beams interconnected thanks to a revolute joint. The components are linked, through a further revolute joint, to a combination of two rigid bodies the latter of which is connected to the flap. The flap, shown in Fig. 2.5, parallel to the blade and for the time being considered as a rigid body, intersects the mechanism link at half of its length.

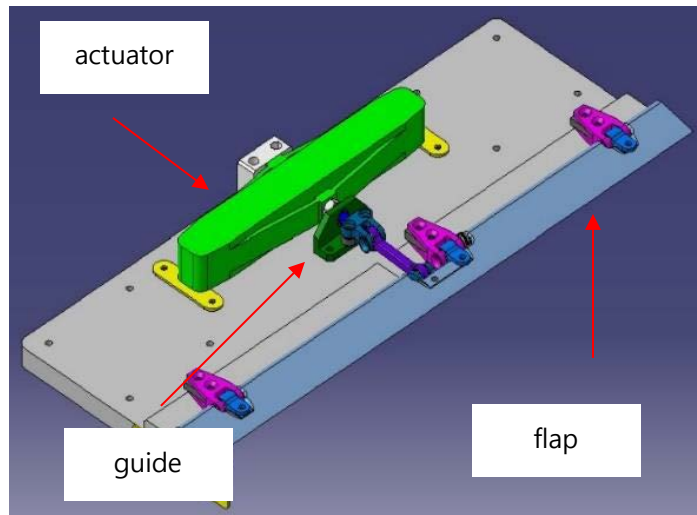


Figure 2.4 Drawing of the mechanism

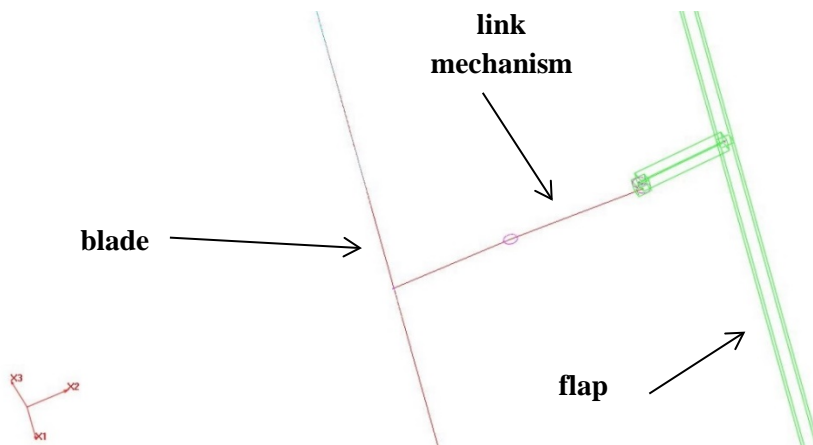


Figure 2.5 DYMORE schematic model

The hub where the two blades connect consists of a revolute joint linked with a vertical shaft clamped to the ground. The said revolute joint is where a rigid rotation is prescribed in order to evaluate the centrifugal load acting on the system.

As already mentioned, within the blade frame we can identify two

different areas: the main one consists of fiber glass roving while the part of the beam parallel to the flap holds within its blade skin a titanium bar placed in the front section chordwise. This means that the structural properties used in the DYMORE model differ whether we consider the roving section or the titanium one.

2.7 Micromechanics to estimate the properties of the composite materials used

While titanium properties, due to its homogeneous nature, are widely available, the same cannot be said for glass roving. Being a composite material, where the glass fibers are reinforced due to the action of a resin matrix, physical properties exhibit different behavior according to the direction the material is tested. As a consequence, the structural properties needed in the following computations have to be purposely calculated based on the percentage amount and the individual properties of the two components.

Micromechanics is a helpful tool which allows to retrieve the final properties taking into account the nature of the composite material constituents and the direction of the loads applied [24]. Once the material geometry is known, we are able to retrieve structural properties of the whole composite material simply exploiting the mechanics of materials approach.

Provided the composite is considered

- macroscopically homogenous
- linear elastic
- initially stress free

The longitudinal modulus results as

$$E_l = V_f E_f + V_m E_m \quad (23)$$

Where E_l is the longitudinal modulus of the composite material whereas V_f and V_m and E_f and E_m are respectively the volume fraction and the longitudinal modulus of the fiber and the matrix.

A similar approach can be exploited when computing the transversal modulus

$$\frac{1}{E_t} = \frac{V_f}{E_{tf}} + \frac{V_m}{E_{tm}} \quad (24)$$

Where E_t is the transversal modulus of the composite material whereas V_f and V_m and E_{tf} and E_{tm} are respectively the volume fraction and the transversal modulus of the fiber and the matrix.

Finally, shear modulus is computed as

$$G = \frac{1}{\frac{V_m}{G_m} + \frac{V_f}{G_f}} \quad (25)$$

Where G_t is the shear modulus of the composite material whereas V_f and V_m and G_f and G_m are respectively the volume fraction and the shear modulus of the fiber and the matrix.

Results from the above computations are described in Table 2.1.

Table 2.1 Material properties

Properties	Titanium	Glass roving
EA (N)	1.978×10^7	8.459×10^6
EI_{flap} (Nm²)	1.876×10^4	8.339×10^3
EI_{lag} (Nm²)	5.292×10^2	4.042×10^2
GJ (Nm²)	7.476×10^2	5.456×10^2
Mass per unit span (kg/m)	9.280×10^{-1}	5.256×10^{-1}

2.8 Model features

The designed model will be equipped with different features able to provide a deeper insight in the behavior of the rotor. In the static analysis, when a prescribed rigid rotation is applied at the rotor hub, blades start rotating about the shaft which is instead rigidly clamped. Such motion will highlight the centrifugal forces acting along the blade and the axial load born at the root will be computed.

Another degree of motion considered in the DYMORE model is the oscillation of flap driven by an external force imposed in the proximity of the prismatic joint. This element allows the displacement of the whole link mechanism without any major influence to the blade; as the prismatic joint dilates and contracts the other components within the flap mechanism will

move accordingly.

The function which is imposed to the flap mechanism is related with the actual movement of the actuator and the input voltage provided to it. Whereas previously [10] no connection was taken into account between the input voltage and block force-stroke relationship which characterizes the actuator, a new revision instead a more detailed connection among the quantities, as displayed in Fig. 2.6.

Variation in the supplied voltage directly affects the actuator performances according to the formula

$$\frac{F}{F_{\max}} + \frac{x}{x_{\max}} = \frac{V}{V_{\max}} \quad (26)$$

Where F is block force, x is the stroke and V is the input voltage.

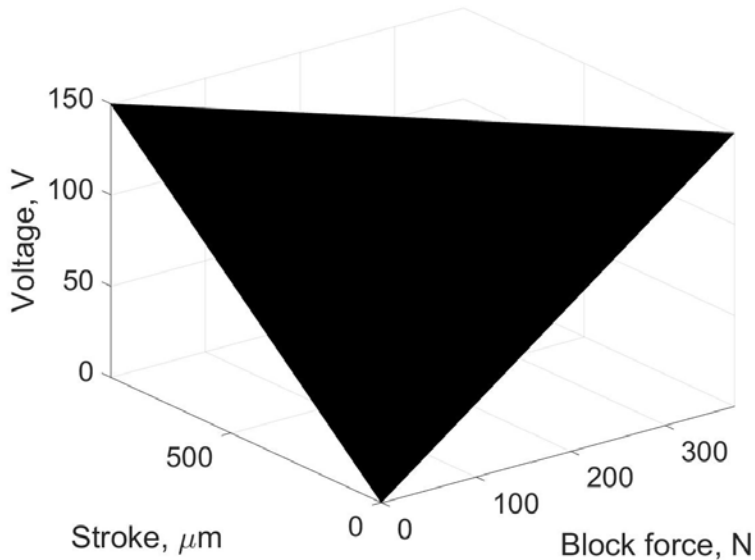


Figure 2.6 Relationship among the block force, input voltage, and stroke

Also, a kinematic equation is formulated in order to describe the flap motion during its actuation.

$$M = -k\vartheta \quad (27)$$

$$F = -\frac{k}{L_2}\vartheta \quad (28)$$

$$x = L_2(\vartheta_0 - \vartheta) \quad (29)$$

Where M and F are respectively the moment and force applied at the flap hinge, ϑ is the angular displacement, L_2 is the moment arm and k the torsional spring stiffness.

The torsional spring applied at the revolute joint aims at simulating the aerodynamic load over the flap. In fact, it works as if a pressure distribution was present over the flap and contrasted the surface movement once the aerodynamic environment is recreated. To determine the stiffness of the torsional spring and thus, the load to apply, ANSYS FLUENT calculations were exploited. The hinge moment coefficient previously extracted was plotted in Fig. 2.7 versus the deflection angle and a hysteresis-like distribution was retrieved.

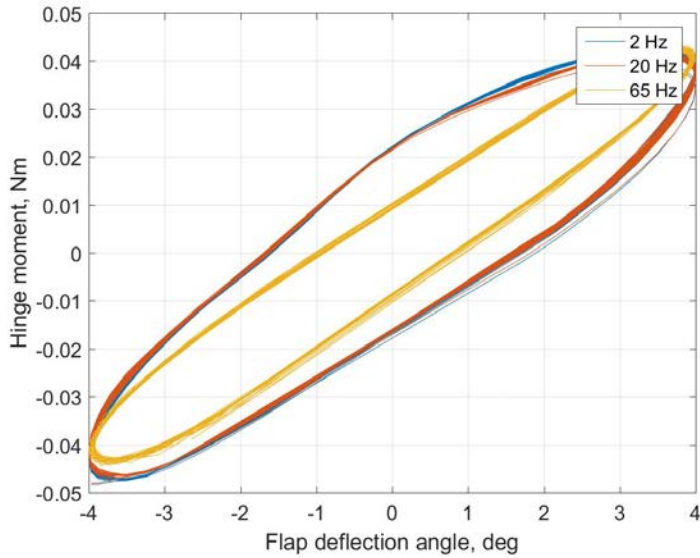


Figure 2.7 Hinge moment evolution

The data distribution can be summarized through a regression line per each of the frequencies considered; as the angle of the attack of the airfoil was 0 degrees for all the measurements, the plot shows a perfect symmetry around the chart origin. Once the analytical formula of the regression line is obtained, slope and y-intercept are first transformed into Chebyshev coefficients [25] and then used to define the stiffness of the torsional spring. Nonetheless, as the hinge moment coefficient does not vary significantly as the actuation frequency grows, springs features visible in Table 2.2, will not differ much one another.

Table 2.2 Chebyshev coefficients

Frequency [Hz]	Zero grade coefficient	First grade coefficient
2	$-3 \cdot 10^{-4}$	0.5815
20	$-2 \cdot 10^{-4}$	0.5734
65	$9 \cdot 10^{-6}$	0.5962

Being all the parameters defined, the final formulation which connects input voltage, block force and stroke results from the combination of eqs. (27) and (30).

$$V = -V_{\max} \left(\frac{k}{L_2 F_{\max}} + \frac{L_2}{x_{\max}} \right) \mathcal{G} + \frac{L_2 V_{\max}}{x_{\max}} \mathcal{G}_0 \quad (30)$$

Other than the prescribed rotations, within DYMORE capabilities, aerodynamic influence can also be observed. As a consequence, a further analysis implemented model focuses on the aerodynamic conditions. Each blade is provided spanwise with a lifting line which is a collection of points, called airstations, measuring different parameters of the incoming flow; for the current analysis a number of 81 equally spaced airstations were exploited.

2.9 Pulling test implementation

The use of the ATF in a rotating environment implies the ability of the whole device to cope with the centrifugal force which springs from the blade rotation. A structural analysis of the actuator by NASTRAN has already been conducted [26] and a strain which amounted to 33.5% of the

allowable was obtained when distance from the rotation center was 1.125 m. Now instead, the designed and manufactured pulling test, displayed in Fig. 2.8, focused on the whole device axial strength as well as the flap deflection in a non-static context. In fact, other than the blade stiffness [27], the outcomes of the described experiment will give an estimation of the flap displacement reduction compared to a static case.

The intrinsic dynamics of the rotor and the friction between the flap and the static section of the blade are two of the elements which contribute to a decrease of the displacement once the rotating conditions are considered. Consequently, the deflection aimed at in the static case should be high enough to guarantee a successful operation of the device and thus an efficient dampening of the vibrations in the final conditions.

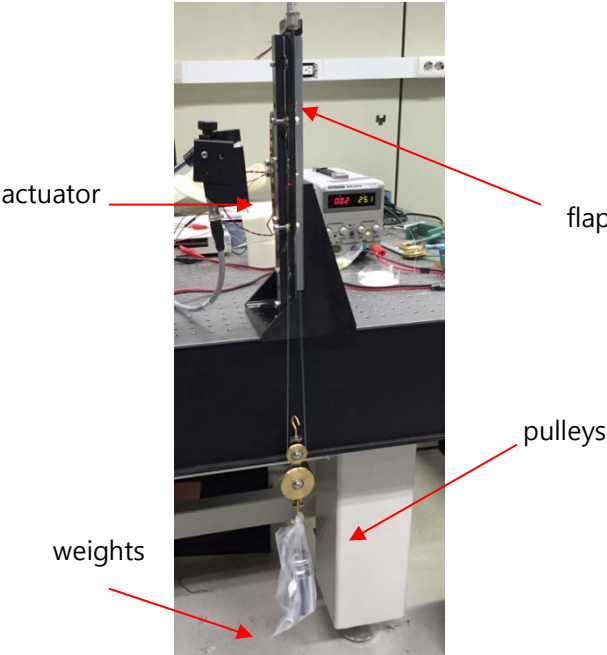


Figure 2.8 Pulling test test-bed

III. NUMERICAL AND EXPERIMENTAL RESULTS

3.1 Steady state results

Once all the parameters listed in Table 3.1 are set, the solution can be thus initialized using the flow values at inlet as the initial guess.

Before implementing the proper analysis, evaluation of lift, drag and moment coefficient were performed for the airfoil without any flap deflection. Data were collected for $[-10^\circ, 10^\circ]$ span and the correspondent curves first constructed as shown in Figs. 3.1, 3.2 and 3.3.

Table 3.1 Aerodynamic analysis conditions

Flap location [m]	1.125
Flap length [m]	0.300
Flap chord [m]	0.023
Mach number	0.45
Fluid density [kg/m^3]	1.125
Temperature [K]	300
Flow condition	Viscous, compressible

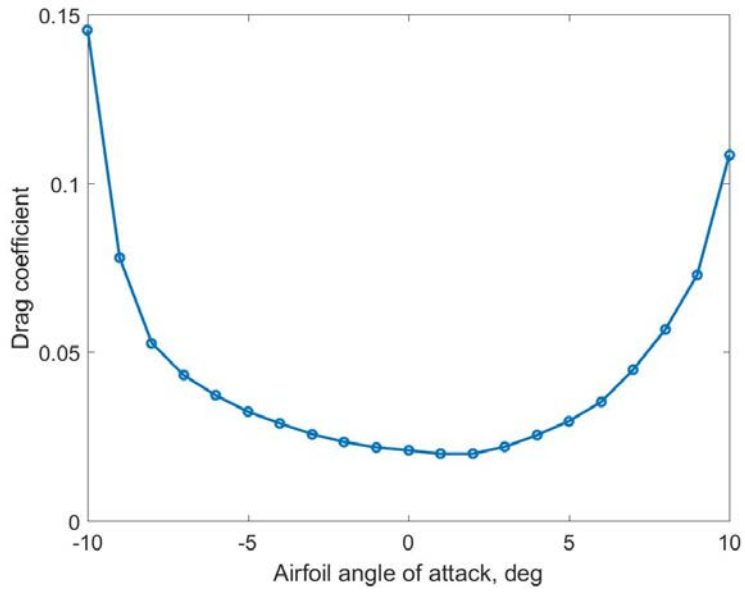


Figure 3.1 Drag coefficient with no flap deflection

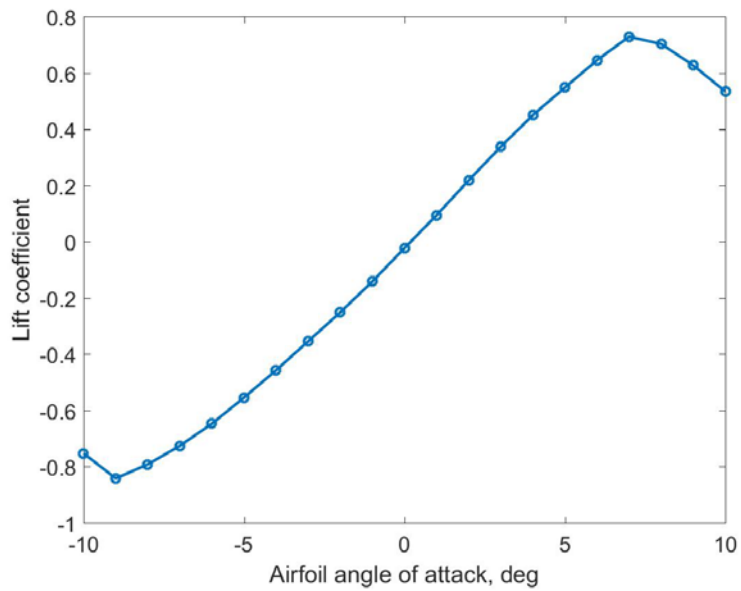


Figure 3.2 Lift coefficient with no flap deflection

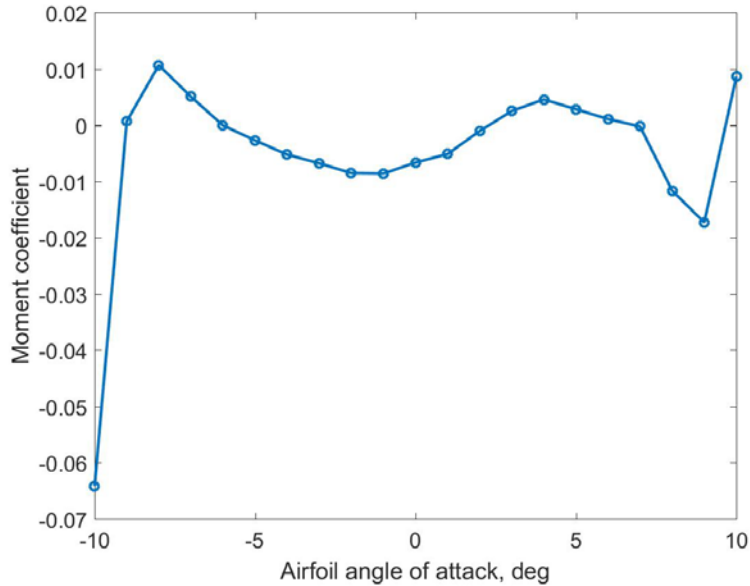


Figure 3.3 Moment coefficient with no flap deflection

As expectable [13], drag coefficient is characterized by symmetrical aspect about the axis passing through 0° , and 10° and -10° are the highest peaks. Lift, instead shows a gradually increasing trend where the stalling point at 9° and -9° are easily visible. Finally, moment coefficient does not have remarkable variation in the range considered although in correspondence of 10° and -10° absolute values start growing.

In the final analysis, the aerodynamic coefficients will not be constant but change as the flap oscillates between 4° and -4° and the resulting pressure distribution will directly act on the linking rod and generate internal forces within the beams constituting the mechanism link. To verify whether the actuator and the device have the necessary strength to sustain and overcome the external forces, a static analysis simulates the flap deflected by 10° and extracts the values of aerodynamic coefficients

visible in Figs. 3.4, 3.5 and 3.6.

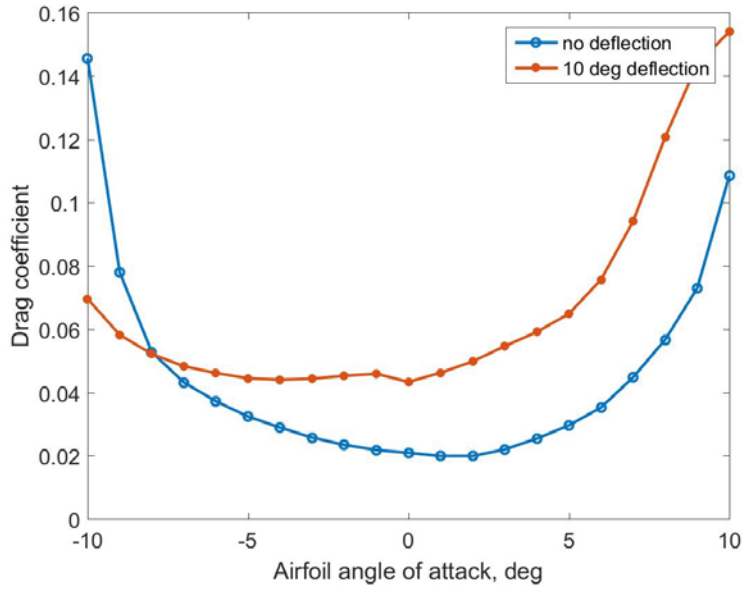


Figure 3.4 Drag coefficient comparison

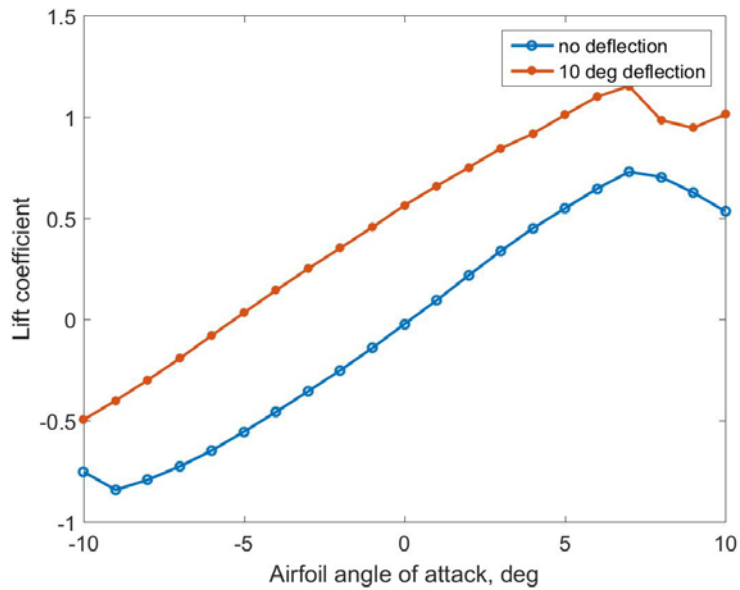


Figure 3.5 Lift coefficient comparison

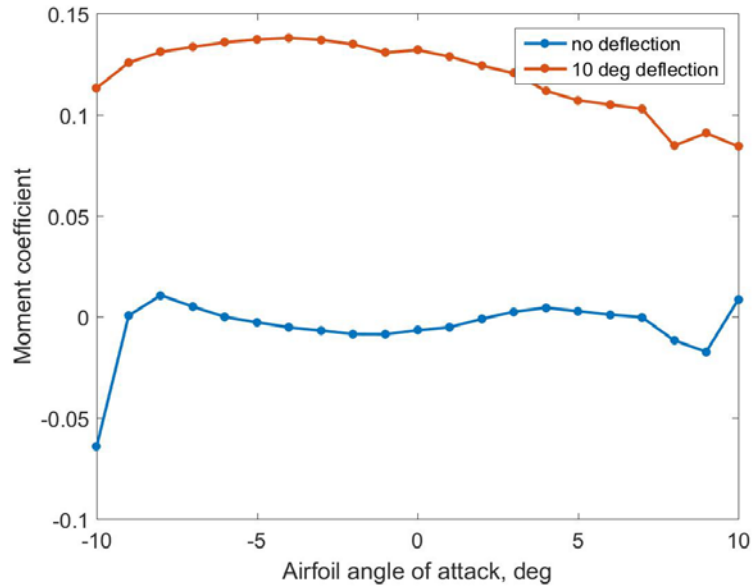


Figure 3.6 Moment coefficient comparison

The comparison between the case with no flap deflection and the case where the flap is deflected by 10° shows a general increase in drag coefficient. This result is due to the fact that the normal surface hit by the flow, with the exception of the -10° configuration, is broader. In that specific case only the main body is hit by the flow while the deflected flap is parallel to the streamlines and does not contribute in terms of frontal area. Results coming from lift coefficient analysis show why moving surface are widely employed: the constant offset visible in the comparison with the non-deflected flap case occurs when the flap deflects and the airfoil chord gets longer resulting in the increase of the lift coefficient. Moment coefficient as well has a positive offset.

The accuracy of the current mesh was questioned comparing the extracted aerodynamic coefficients with results from a similar analysis

where a more refined mesh (2990 hexahedral and 14212 triangular elements) was in use.

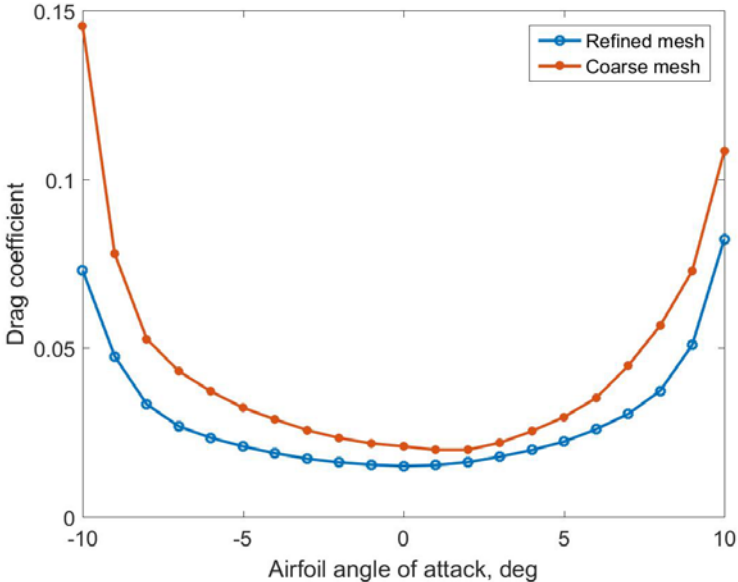


Figure 3.7 Refined mesh-coarse mesh comparison for drag

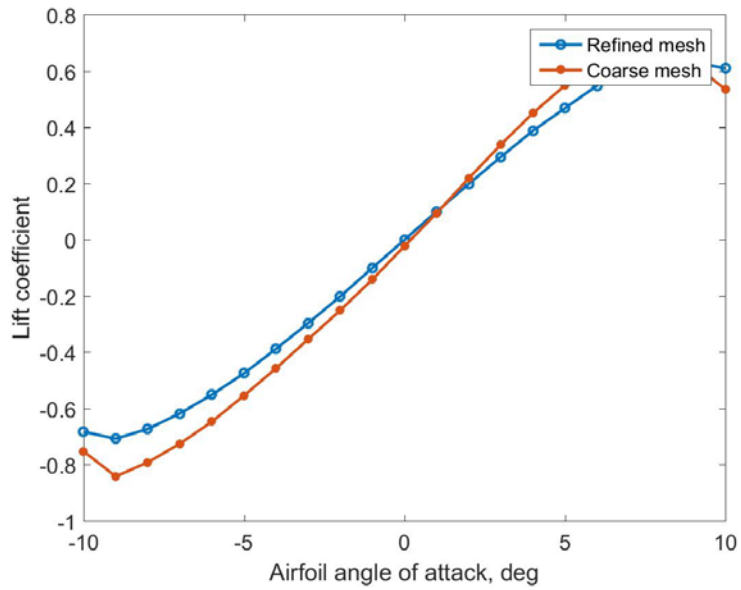


Figure 3.8 Refined mesh-coarse mesh comparison for lift

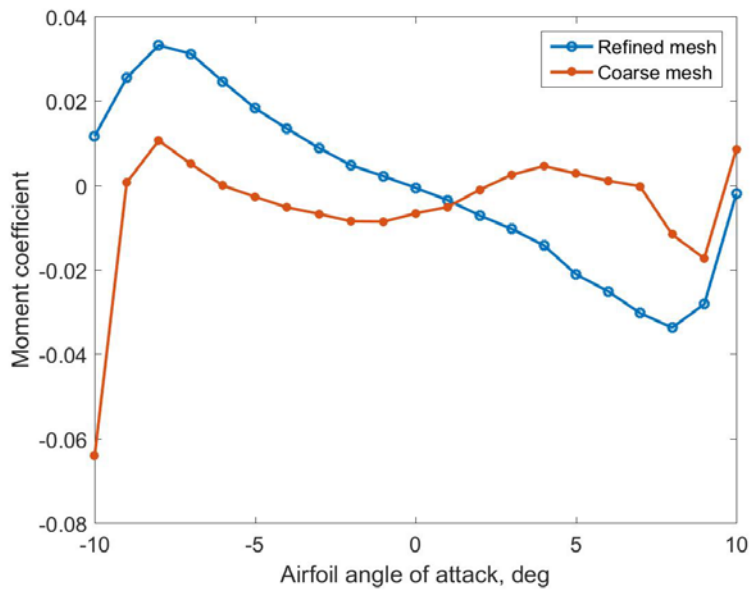


Figure 3.9 Refined mesh-coarse mesh comparison for moment

Although results from both analyses, represented in Figs. 3.7, 3.8 and 3.9, have a strong similarity, refined mesh shows smoother and perfectly symmetric, in drag coefficient case, and antisymmetric, in the case of moment and lift coefficients, trend. As far as values are concerned, the widest gap between the two data sets is seen in the lift coefficient in correspondence of both stalling angles, as also depicted in Fig. 3.9, where flow instability is at its peak.

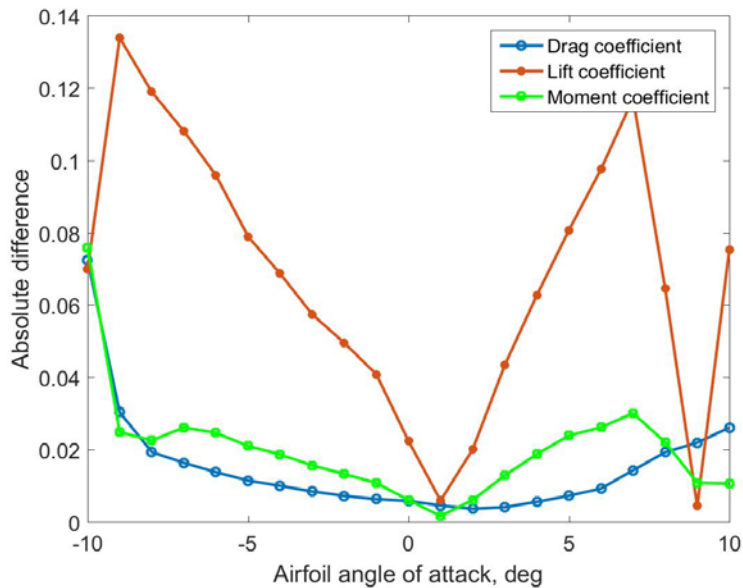


Figure 3.10 Absolute difference between the coarse and refined mesh

Nevertheless, the highest reliability of the results coming from the refined mesh does not justify its use in the actual computation; as a matter of fact, the transient analysis, ultimate goal of our research, already requires a relevant computational cost which would be further aggravated by the increase in the number of nodes.

Static analysis was also exploited to retrieve values for the hinge

moment coefficient so as to compare it with the ideal fluid formulation and evaluate the possible discrepancies.

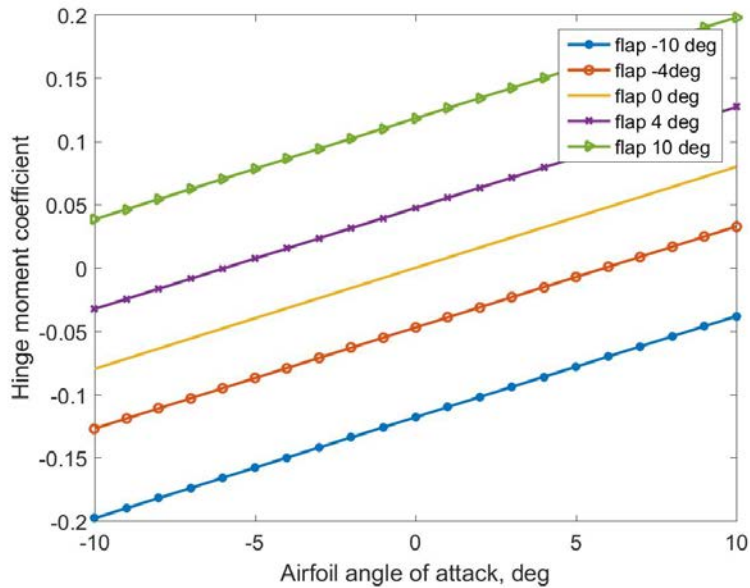


Figure 3.11 Hinge moment trend according to Walz and Chopra [8]

Ideal fluid formulation in Fig. 3.11 shows that as the angle of attack of the airfoil increases, hinge moment coefficient grows due the pressure distribution on the lower surface of the flap which results in a counterclockwise rotation. Moreover, higher flap deflection angles (angles are measured positive when flap deflects downward) imply a further increase in the value of hinge moment coefficient

Specifically, when the prediction of the hinge moment coefficient for 0 degrees of angle of attack is compared with the results extracted from ANSYS FLUENT analysis, a relatively ample discrepancy is observed in Fig. 3.12; this is mostly due to the specific layout of the airfoil considered in the CFD analysis where the single slot is responsible for phenomena

extremely difficult to model. Nevertheless, as the static analysis is conducted at a deflection angle outside the expected range simply to estimate the highest values which could be encountered, the results obtained in ANSYS FLUENT are chosen in light of a more conservative approach.

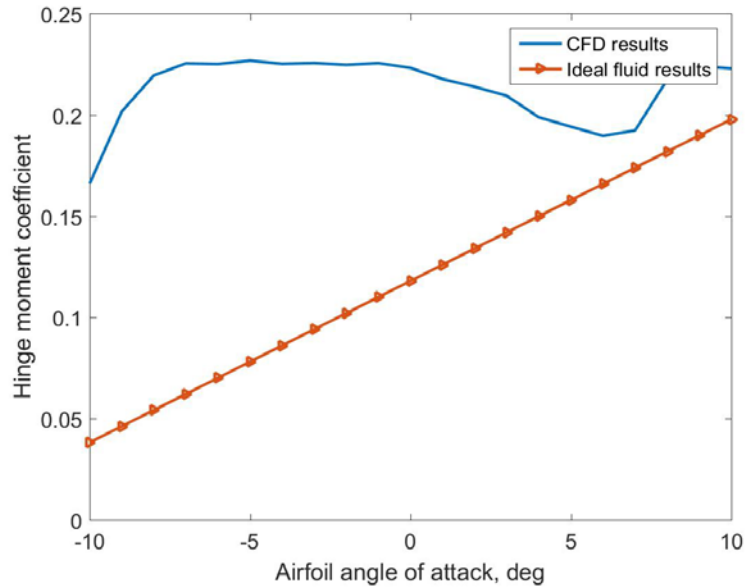


Figure 3.12 Hinge moment comparison with 10° flap deflection

3.2 Transient state results

In transient analysis aerodynamic coefficients are measured for different angles of attack, to observe the range of oscillation, and for different frequencies of actuation of the flap. The outcomes are plotted in Figs. 3.13-3.21.

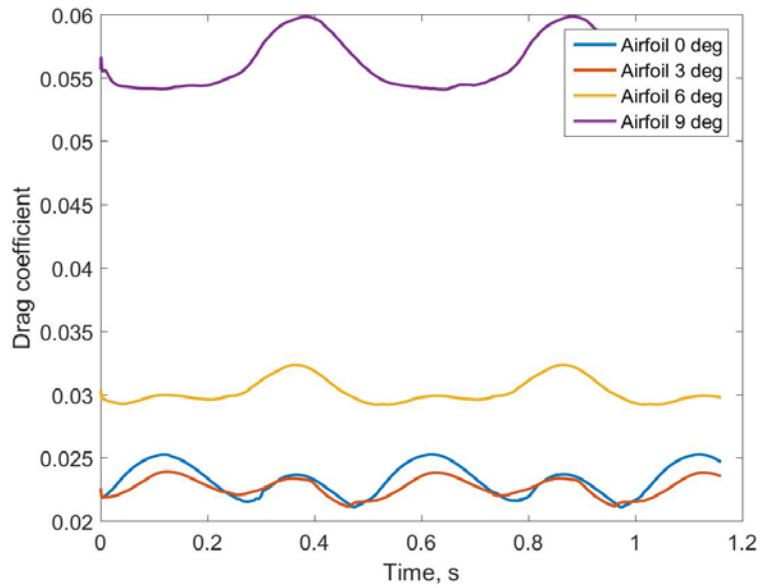


Figure 3.13 Drag coefficient at 2 Hz flap actuation

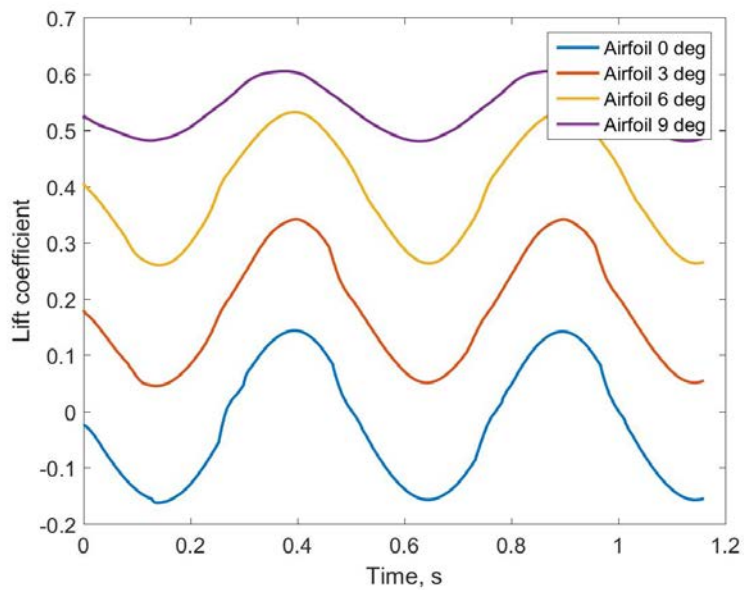


Figure 3.14 Lift coefficient at 2 Hz flap actuation

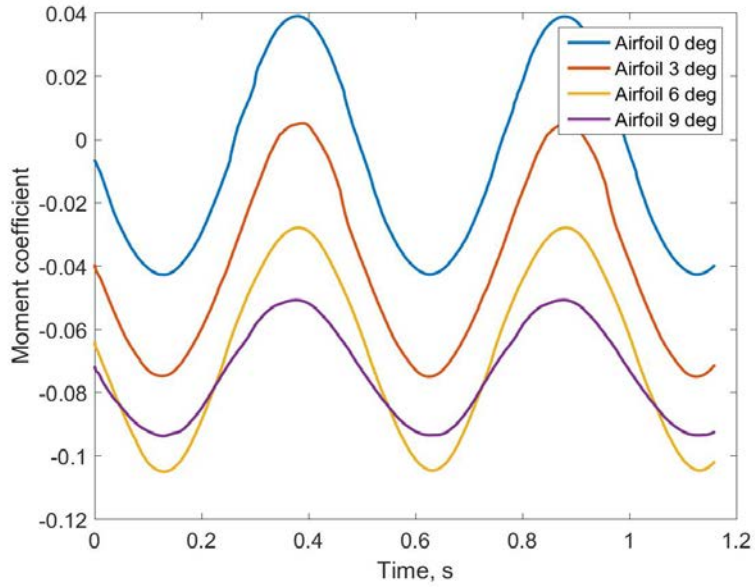


Figure 3.15 Moment coefficient at 2 Hz flap actuation

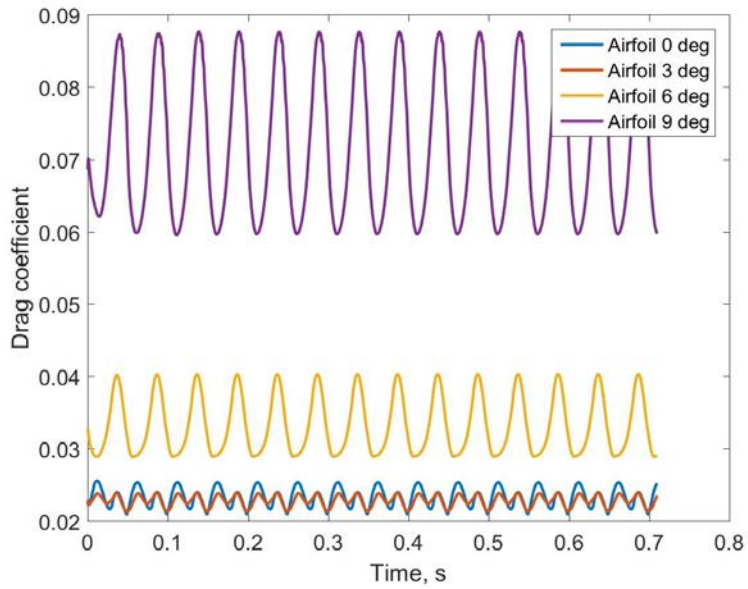


Figure 3.16 Drag coefficient at 20 Hz flap actuation

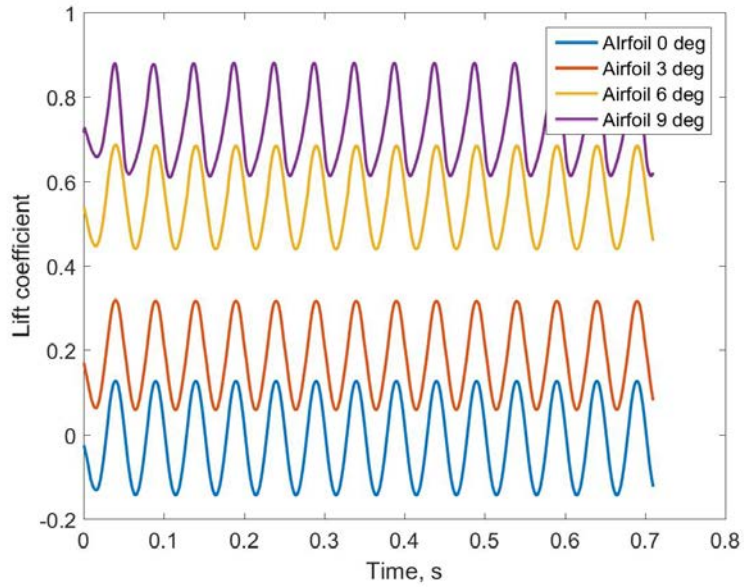


Figure 3.17 Lift coefficient at 20 Hz flap actuation

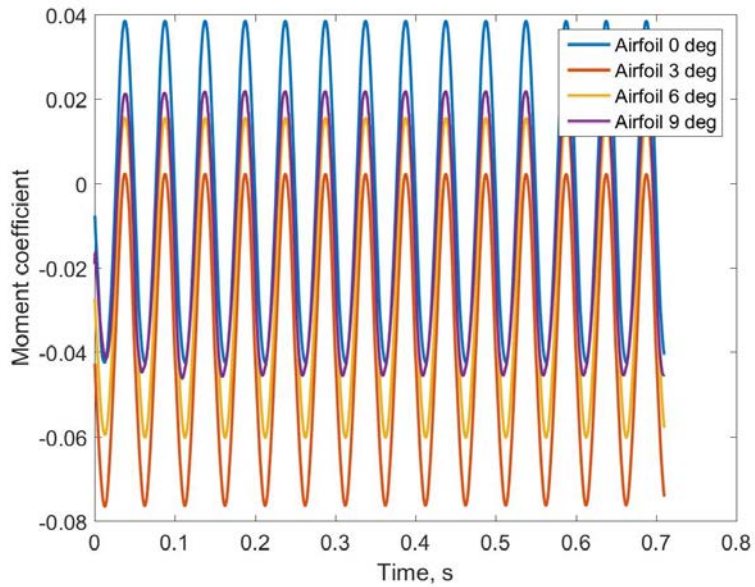


Figure 3.18 Moment coefficient at 20 Hz flap actuation

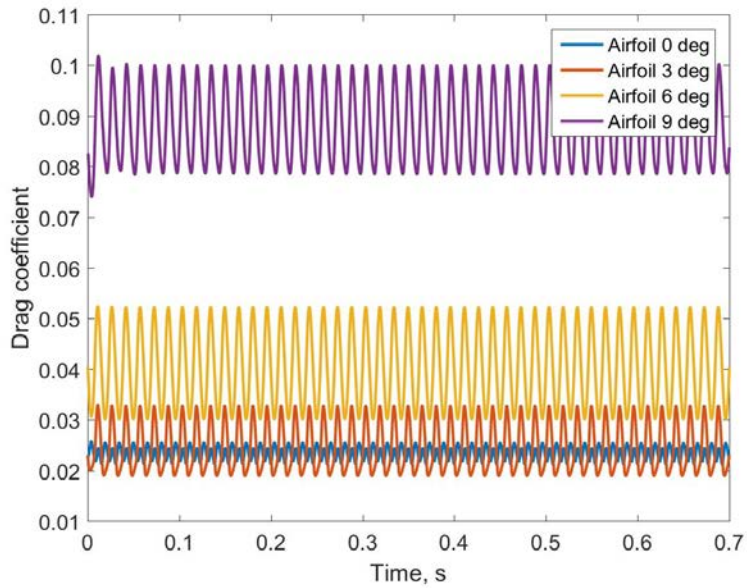


Figure 3.19 Drag coefficient at 65 Hz flap actuation

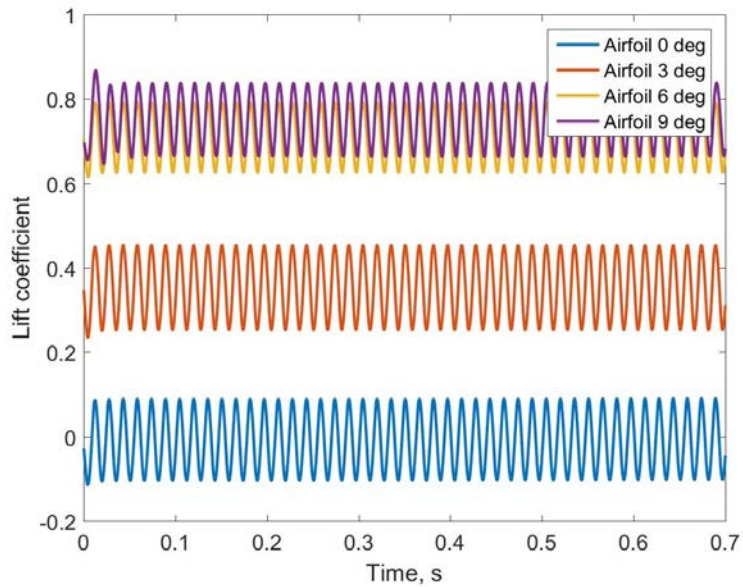


Figure 3.20 Lift coefficient at 65 Hz flap actuation

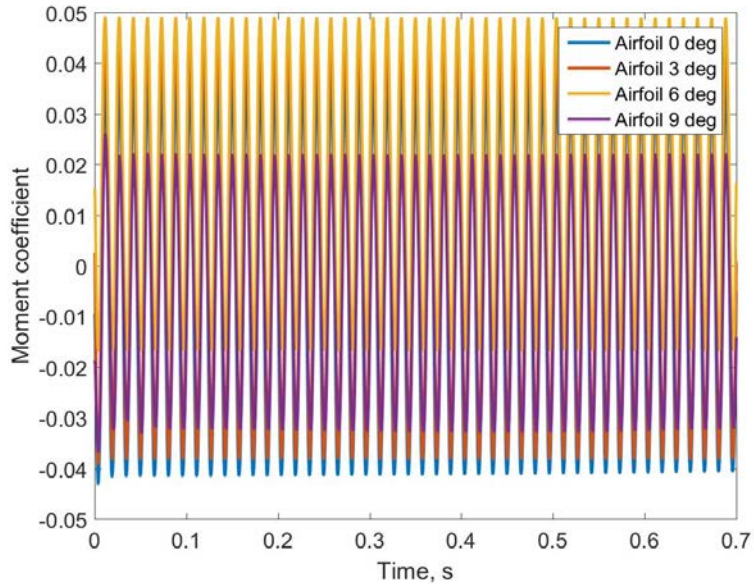


Figure 3.21 Moment coefficient at 65 Hz flap actuation

As visible in the different figures, while the frequency changes, aerodynamic coefficients do not encounter any radical modification. This result should be expected given that the lift, moment and drag coefficient values do not have any connection with the frequency of actuation of the flap and no significant loss due to fluid movement occurs. Nonetheless, discrepancies are observed between analyses where the angle of attack was equal but a different frequency of actuation was imposed: this is probably due to numerical mistakes which originate from the coarse mesh and critical areas such as the trailing edge and the slot.

Lift coefficient increases regularly as the angle of attack grows although overlapping between the graphs is visible in the surroundings of the stall angle. On the contrary, drag coefficient values overlap for smaller angles of attack and steeply grows up to 0.09 when deflection reaches 9 degrees; drag coefficient is also characterized by the increase of oscillation range

due to the projection of the flap with respect to relative wind: the growing angle of attack sums up to the deflection angle and this results in a broader spectrum of drag coefficient value.

Finally, moment coefficient does not show any remarkable trend and, regardless of the angle of attack, oscillates within a limited range.

At last, the main objective of the CFD analysis, the hinge moment, is retrieved in Figs. 3.22, 3.23, and 3.24 simply considering the moment balance about the flap hinge placed at 0.11442 m from the leading edge. As observed with pitch moment, there no definite connection between the hinge moment values and the angle of attack growth, at least in the range examined. Nonetheless, given that the range of oscillation for all the frequencies remains constant, we can conclude that no major energy losses occur during flap actuation despite the viscosity of the fluid.

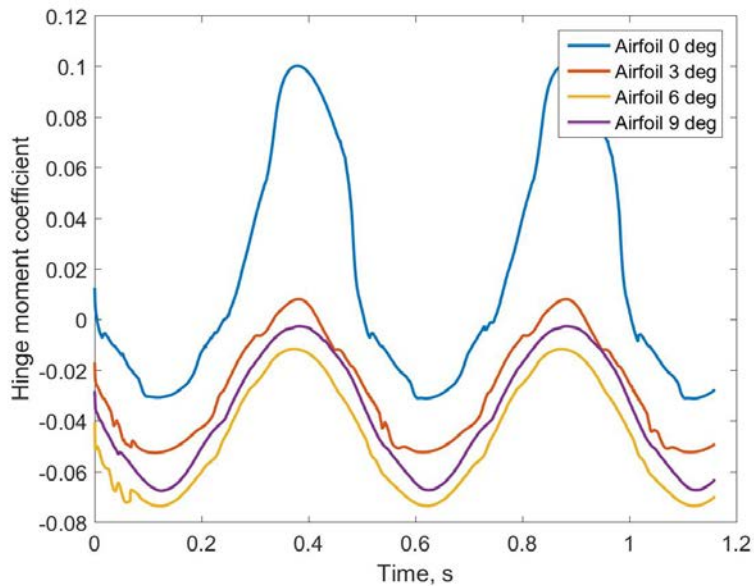


Figure 3.22 Hinge moment coefficient at 2 Hz flap actuation

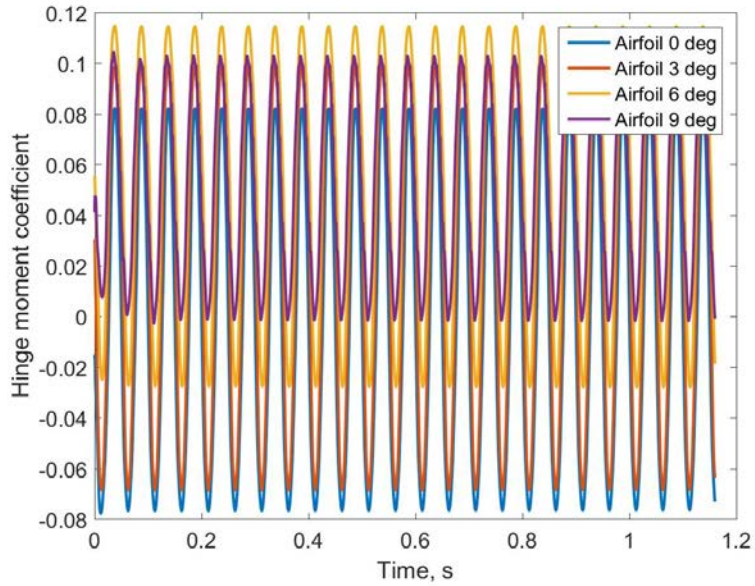


Figure 3.23 Hinge moment coefficient at 20 Hz flap actuation

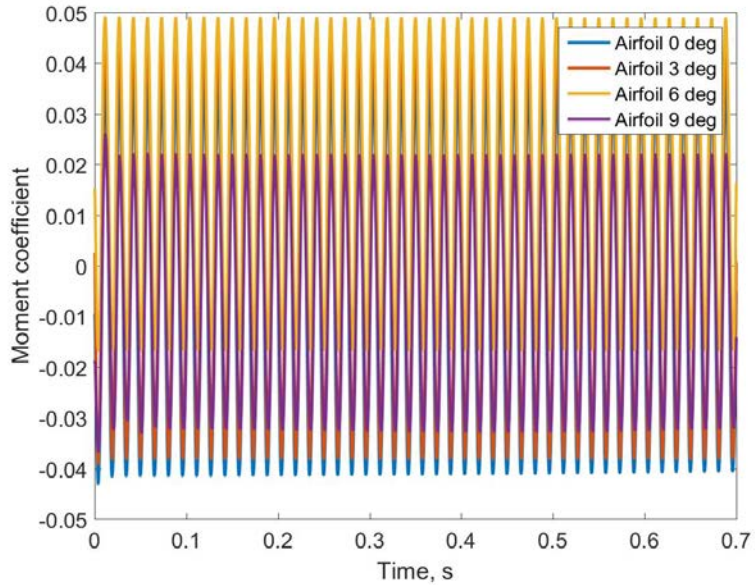


Figure 3.24 Hinge moment coefficient at 65 Hz flap actuation

In the light of the hinge moment acting on the flap during the transient

analysis, in Fig. 3.25 the deflection angle was evaluated in terms of the available moment arm length was evaluated and showed that when aerodynamic conditions are applied, despite the hinge moment acting over the flap which moves at 20 Hz, the minimum requirement of 4° flap deflection is still achievable.

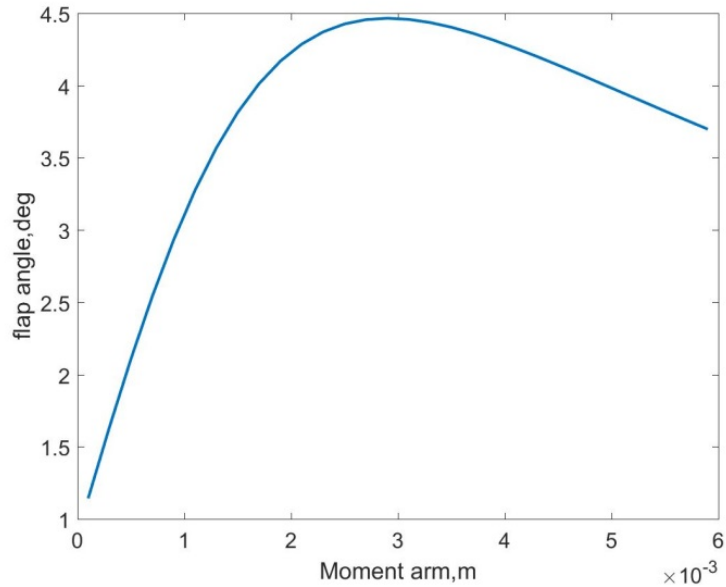


Figure 3.25 Flap deflection as a function of the moment arm length (predicted)

3.3 DYMORE centrifugal load analysis

The first analysis conducted focuses on the centrifugal acceleration which will occur once the system starts rotating. In order to validate the model accuracy, theory formulations is also considered using the following data: blade length of 1.5 m and specific mass which is 0.928 kg/m for the titanium bar and 0.527 kg/m for the glass roving. When the rotor moves at 172 rad/s the total force at blade root is:

$$\begin{aligned}
\int_{root}^{tip} dF &= m_{glass} \int_{section1} da + m_{glass} \int_{section2} da + \dots \\
&\dots + m_{titanium} \int_{section3} da + m_{titanium} \int_{section4} da = \\
&m_{glass} \omega^2 \int_{section1} dr + m_{glass} \omega^2 \int_{section2} dr + \dots \\
&\dots + m_{titanium} \omega^2 \int_{section3} dr + m_{titanium} \omega^2 \int_{section4} dr \approx 13,000N
\end{aligned}
\tag{31}$$

As visible in Fig. 3.26, once the rotor reaches the full speed, the axial force acting along the blade registered by DYMORE model accounts only for slightly more than 15,000 N; the discrepancy with the theory formulation is justifiable by the beam elasticity which subtracts part of the axial solicitation. Also, the part of the link mechanism designed as rigid body is not accounted by DYMORE given that only beams are considered as objects with mass. Once both aspects are taken into account, the discrepancy between DYMORE model and theory application will be reduced considerably.

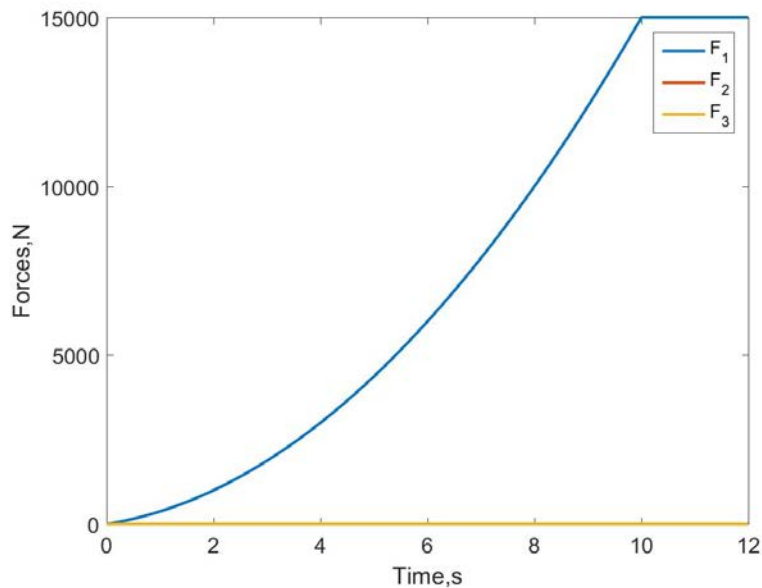


Figure 3.26 Internal forces at the blade root

Confirmation of the DYMORE model is guaranteed when the same analysis is conducted instead at the blade tip in Fig. 3.27 Due to the fact that no constraints are applied on this extremity, no internal forces should be registered when the only external solicitation consists of the prescribed rigid rotation.

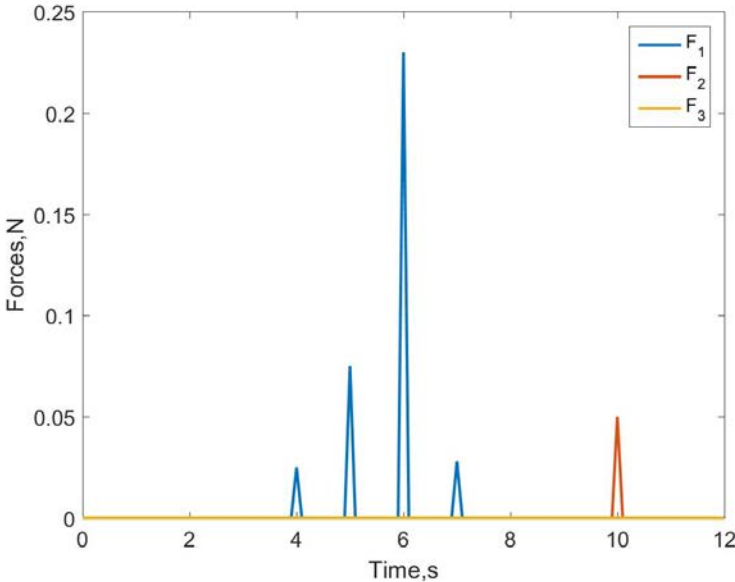


Figure 3.27 Internal forces at the blade tip

As a consequence, the only forces sensed at the blade tip, whose values are infinitely smaller than what registered at the blade root, derive from numerical inaccuracies and do not have any physical origin.

3.4 DYMORE flap deflection analysis

Given that the relationship among block-force, actuator stroke and input voltage has already been defined, the function corresponding to the desired output is then inserted in DYMORE static model as results in Figs. 3.28, 3.29 and 3.30.

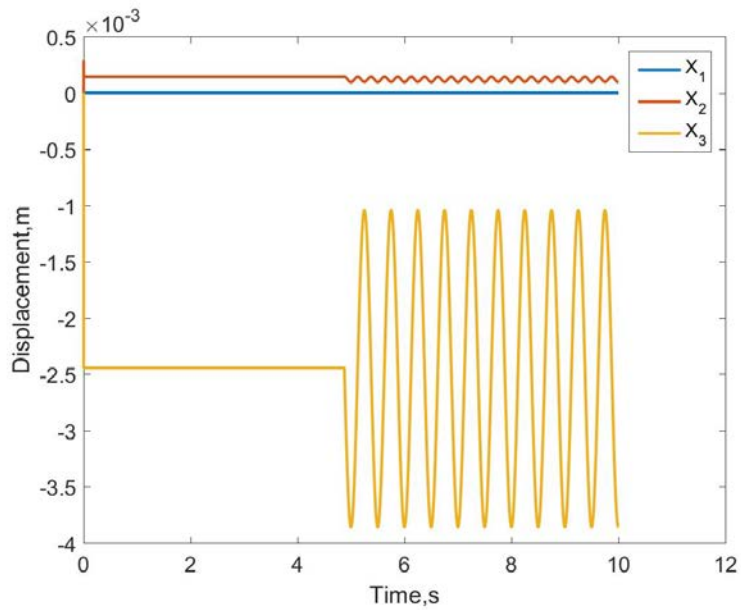


Figure 3.28 Flap deflection at 2 Hz actuation

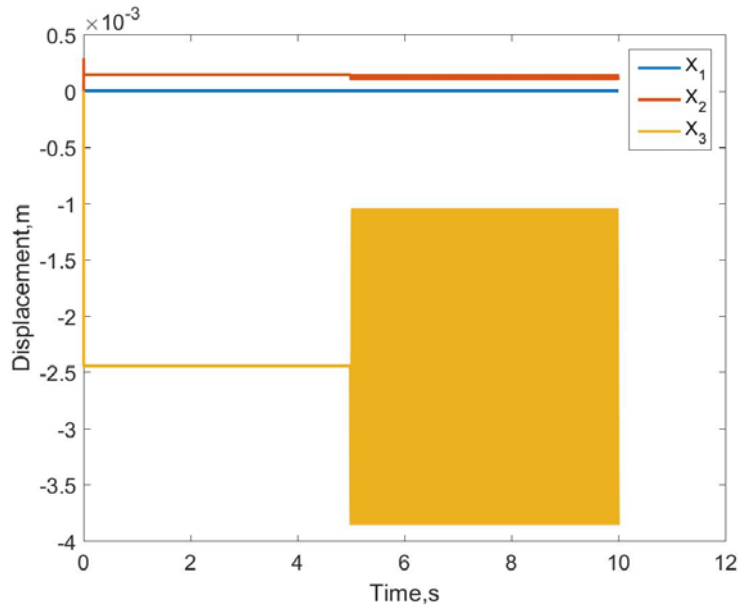


Figure 3.29 Flap deflection at 20 Hz actuation

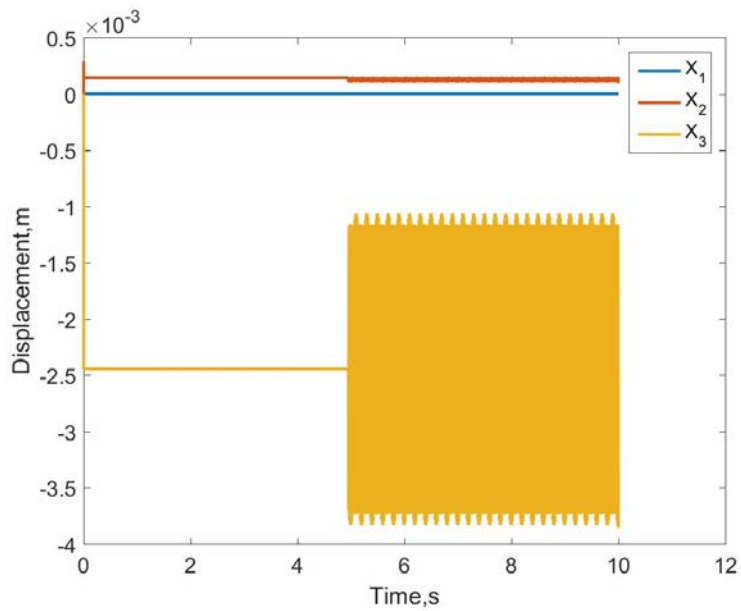


Figure 3.30 Flap deflection at 65 Hz actuation

From the geometry configuration we know that the flap chord length is 0.0203 m and observing the results from DYMORE we can determine that, despite the elasticity of the beams within the mechanism link, the vertical displacement of the flap corresponds to an angular rotation of $\pm 4^\circ$.

3.5 DYMORE aerodynamic loads analysis

Aerodynamic conditions have to be evaluated so as to complement what extracted from ANSYS FLUENT and, at the same time, obtain a more global description of the fluid flow all over the blade. A first analysis is conducted in hover conditions and with no flap displacement. The aerodynamic data considered consist of 272 rad/s rotation and 81 stations equally spaced along the single lifting line which spans from the blade root at 7.62×10^{-2} m from the hub to the blade tip at 1.5 m distance from the rotating center.

The total airloads acting on the single blade are shown in Fig. 3.31.

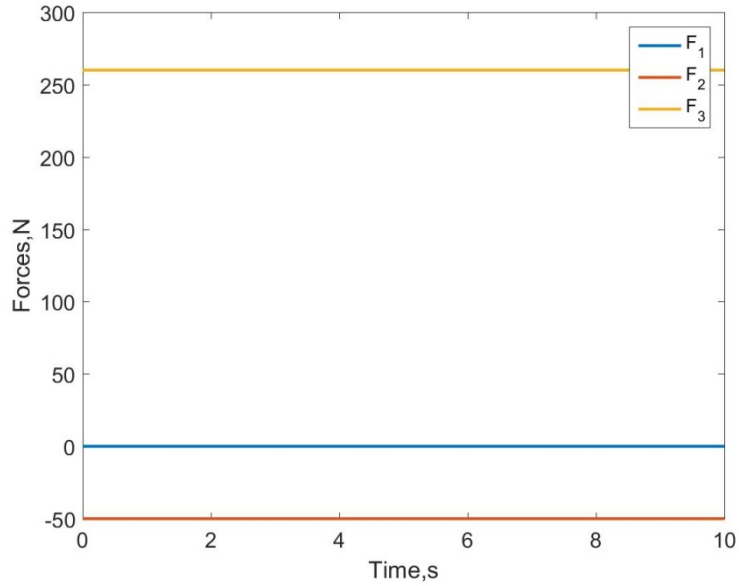


Figure 3.31 Total airloads over a single blade

While no axial load due to aerodynamic forces is observed, the effects of the lift and the drag are visible. In order to validate the results, theoretical approach is exploited.

If we consider the infinitesimal lift as

$$dL = \frac{1}{2} \rho v^2 c c_L dr = \frac{1}{2} \rho \omega^2 c c_L r^2 dr \quad (32)$$

And standard air density at 1.225 kg/m^3 and lift coefficient at 0.1, we obtain:

$$L = \frac{1}{2} \rho \omega^2 c c_L \frac{r^3}{3} = 275 \text{ N} \quad (33)$$

If reference frame is taken into account, same validation is possible for drag force.

$$dD = \frac{1}{2} \rho v^2 c c_D dr = \frac{1}{2} \rho \omega^2 c c_D r^2 dr \quad (34)$$

$$D = \frac{1}{2} \rho \omega^2 c c_D \frac{r^3}{3} = 50N \quad (35)$$

Values of the airloads at the single airstation can be retrieved as well; in the case of the airstation placed at the blade root results are as portrayed in Fig. 3.32.

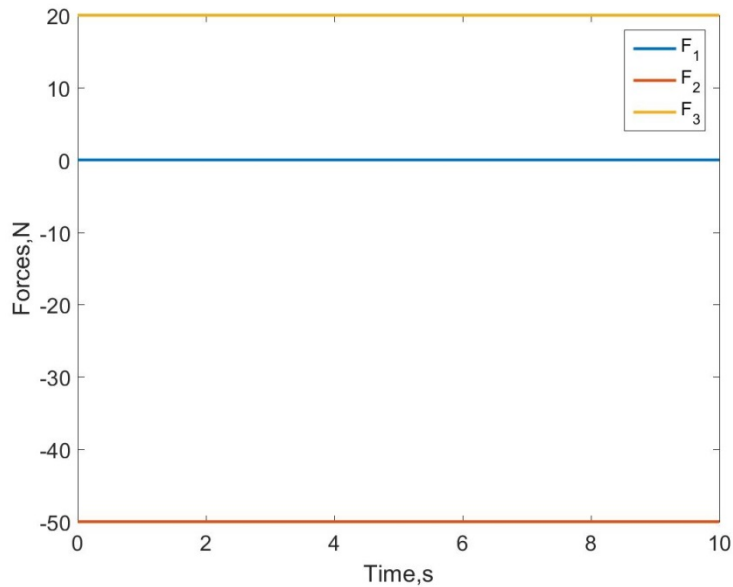


Figure 3.32 Airloads at the blade root

If instead, data from the airstation at the blade tip are observed, we notice in Fig. 3.33 a relevant increase in sectional lift and null values of drag.

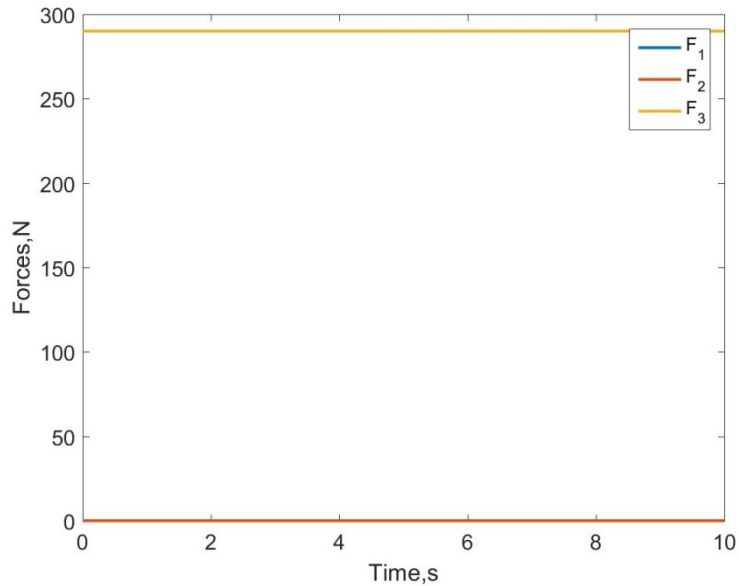


Figure 3.33 Airloads at the blade tip

The final analysis aerodynamic conditions are superimposed over the flap deflection movement imposed and the resulting outcomes are obtained. Centrifugal force instead, is not considered given that in dynamic analysis, implemented to observe aerodynamic loads, it is ignored [25].

Among the different results, the focus was on the flap displacement so as to verify whether any particular event would occur due to the influence of the aerodynamic loads. The actuation frequency imposed, as in the previous static case, amounted to 2 Hz, 20 Hz and 65 Hz.

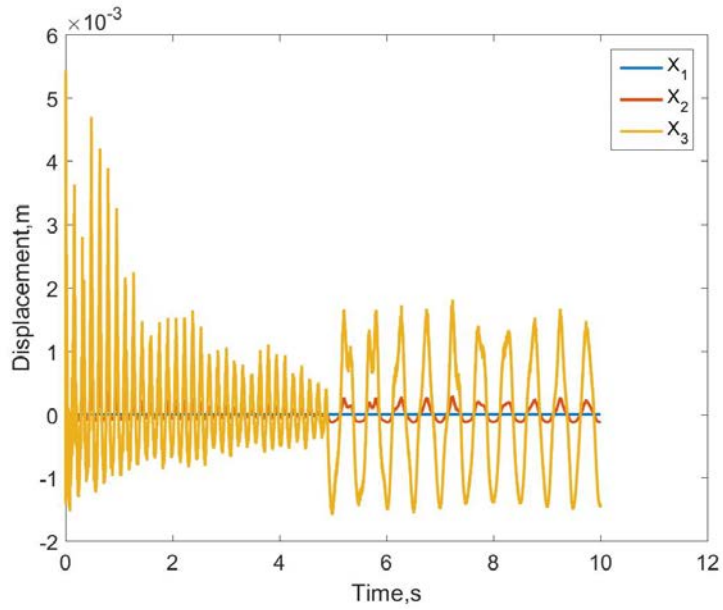


Figure 3.34 Flap deflection at 2 Hz with airloads

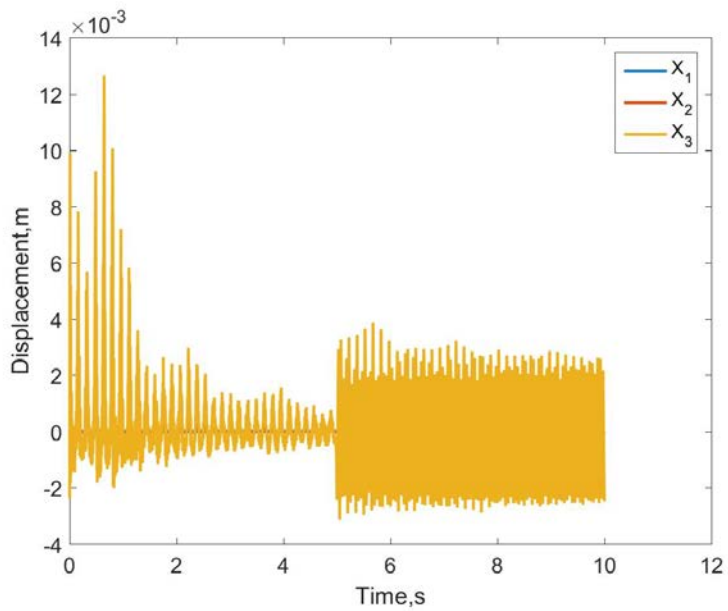


Figure 3.35 Flap deflection at 20 Hz with airloads

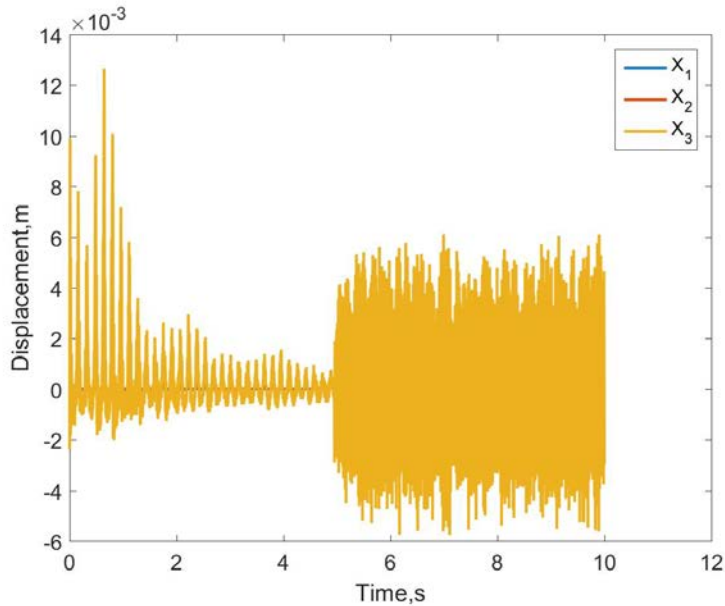


Figure 3.36 Flap deflection at 65 Hz with airloads

As visible in Figs. 3.34, 3.35 and 3.36, dynamic conditions along with the influence of aerodynamic loads, although not directly on the flap as it lacks of any airstation, worsen the definition of a smooth trend in the oscillation. Nonetheless, throughout the actuation period the range remains constant and no obvious divergence is visible. The angular displacement measured in the case where only flap oscillation occurred showed a rotation of $\pm 4^\circ$; when the same approach is repeated we observe that for 2 Hz actuation the deflection angle amounts to $\pm 4,2^\circ$ but at 65 Hz actuation the value skyrockets to $\pm 12^\circ$. Therefore, aerodynamic conditions play a major role in the definition and smoothness of the flap movement. On the other hand, disturbances occurring in this situation have a decreasing evolution and we can expect they will shrink to negligible values in a relatively short period of time. As an example, we observe in Fig. 3.37 the

converging evolution to which the internal forces at the blade root are subjected.

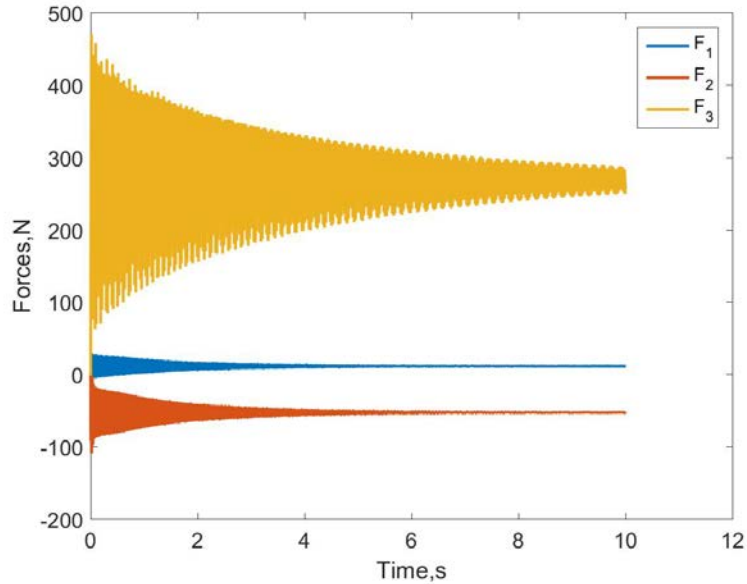


Figure 3.37 Internal forces at the blade root in aerodynamic conditions

3.6 Pulling test results

The manufactured test bed was designed in order to maintain the actuator, the mechanism link and the flap in a vertical position during the experiment; a laser sensor was also exploited to measure the oscillations of the flap. The centrifugal force was recreated through dead weights connected and clamped to the flap thanks to a system of pulleys and wires where the latter were arranged in such a way that the oscillations of the flap would affect the stillness of the dead load applied. Due to the flap

weight of 20 g, the load exerted on the surface will reach the ultimate goal of 40 kg in a gradual way. As expected, in Fig. 3.38 a decrease in the angular displacement could be witnessed.

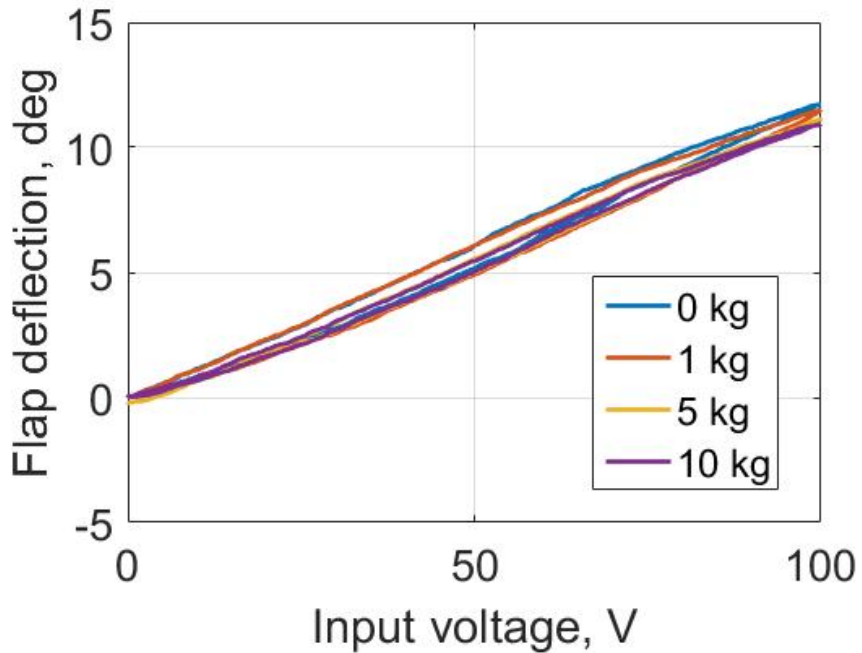


Figure 3.38 Flap deflection under the dead loads

The detail in Fig. 3.39 shows how, compared to the initial maximum deflection of 11.5 degrees, when 10 kg were applied as a dead load, the resultant deflection diminished to 10.9 degrees.

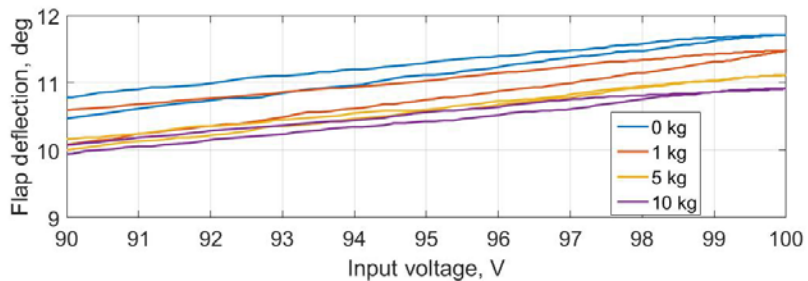


Figure 3.39 Flap deflection under the dead loads [detail]

We also have to consider that, among the different components of the active trailing edge flap, the actuator has the highest mass, being 190 g. Given that the computed load to apply to the device in order to test its strength to centrifugal force is expected to be 400 kg, a pulling test as conducted previously is not possible. As a consequence, an Instron machine, a device able to impose high tensions to the sample, will be exploited; what is more, due to the intrinsic features of a piezoelectric materials which couple mechanical strains with voltage output and vice versa, a dummy actuator, retaining the structural properties of the original one, will be designed and manufactured in order to avoid any possible damage.

IV. CONCLUSION AND FUTURE WORKS

4.1 Conclusion

In this dissertation, the small scaled blade equipped with an active trailing edge flap was analyzed and tested in order to verify its ability to suppress vibratory load generated on the rotor system. Given that the flap will be subjected to forces originating from the aerodynamics, lift, drag and moment coefficients estimations were extracted through a CFD analysis. In particular, so as to verify a smooth and successful operation of the device, the attention was focused over the hinge moment which will counteract the flap oscillation driven by the actuator. The results retrieved from different analyses where the actuation frequency and the airfoil angle of attack varied showed the peak of hinge moment coefficient at 0.17.

Also, a multibody dynamic analysis was implemented to couple the structural properties of the prototype with the aerodynamics generated in a whirl tower; DYMORE was selected as the tool to compute internal forces within the device generated by external loads such as centrifugal force and aerodynamic forces. In addition to that, flap displacement was added to observe its behavior in presence of disturbances. The centrifugal force and the aerodynamic loads measured looked plausible and were also validated through theory formulation and $\pm 4^\circ$ flap oscillation was achieved once the proper input was imposed.

Other than computer based simulation, a practical test was conducted to verify the decrease in oscillation range the flap will be subjected in a rotating environment. As a matter of fact, the centrifugal force acting on the blade will disturb the free movement on the flap and thus, reduce its effective displacement. A set of weights was then applied through a system of wires and pulleys, and once the flap was actuated, the resulting

displacements were measured. From the 11.7° displacement in the unloaded situation, the deflection decreased down to 10.8° when 10 kg were applied. Although it does not correspond to the final objective of 40 kg, the results look promising and we expect an ultimate value still above the $\pm 4^\circ$ minimum requirement.

4.2 Future works

The analyses conducted so far still have room for improvement both in the computer based aspect and in the practical side. The computational fluid dynamic simulation implemented does not take into account pitch rotation of the airfoil as well as possible plunging; these features will be added taking advantage of a further refined dynamic mesh and additional user defined functions able to describe in detail the complete motion of the airfoil. Also, a porous region will be added in the gap between the flap and the main block in order to avoid mass flow and thus perfectly emulate the real aerodynamic conditions. Quality wise, mesh surrounding the flap will be refined and adopt a layout which further decreases numerical error.

Multibody dynamic analysis with DYMORE will be equipped with additional details to better resemble the real case; these consists of the built-in twist angle and an added lifting line along the flap to observe the aerodynamic loads generated over the surface. Once the whole rotor layout will be defined, forward flight condition will be simulated and internal forces as well as external solicitations measured.

The pulling test to verify the flap deflection in rotating environment will be conducted up to its ultimate value of 40 kg; also, in order to decrease the centrifugal force acting on the deflecting surface, the total flap mass will be decreased from the current 20 g to 10 g. An additional verification of the effects of centrifugal force will be conducted on the actuator as well

but, due its relatively high mass, a proper pulling test will be impossible to implement. Being the final load requirement 400 kg, an Instron machine will be exploited and the tension applied to a dummy actuator so as to avoid any damage to the piezoceramic stack due to the force applied.

Finally, a detailed contact analysis will be carried out with NASTRAN to observe the stresses generated within the link mechanism due to the centrifugal force. Each component will be considered and analyzed to verifying whether the occurring stresses pose a risk for structural integrity and excessive wearing during the device actuation.

Reference

- [1] Rita, A., McGarvey, J.H., Jones, R., “Helicopter Rotor Isolation Evaluation Utilizing the Dynamic Antiresonant Vibration Isolator”, Journal of the American Helicopter Society, Volume 23, January 1978.
- [2] Konstanzer, P., Enenkl, B., Aubourg, P., Cranga, P., “Recent Advances in Eurocopter’s Passive and Active Vibration Control”, American Helicopter Society 64th Annual Forum, Montreal, Canada, May, 2008.
- [3] Paselk, Robert A., “Development of an Environmental Design and Test Guide for Army Rotary Wing Aircraft”, Los Angeles Aircraft Division, Rockwell International Corporation, February 1976.
- [4] Vincent, A.H., Lewis Cure, R.W., “Bifilar Vibration Dampers”, patent US 3932060, January 1976.
- [5] Desjardins, R.A., Hooper, W.E., “Antiresonant Rotor Isolation for Vibration Reduction”, Journal of the American Helicopter Society, January 1980.
- [6] Ahci, E., Rupert, P., Straße, W. M., “Structural Design, Optimization and Validation of the Integrated Active Trailing Edge for a Helicopter Rotor Blade”, The American Helicopter Society 64th Annual Forum, Montreal, April 2008.
- [7] Lee, T., Chopra, I., “Design of Piezostack-driven Trailing Edge Flap Actuator for Helicopter Rotors”, Smart Materials and Structures, February 2001.
- [8] Walz, C., Chopra, I., “Design and Testing of a Helicopter Rotor Model with Smart Trailing Edge Flaps”, Structural Dynamics and Materials Conference, Adaptive Structures Forum, April 1994.
- [9] Natarajan, B., “Structural Analysis and Actuation Tests of an Active Trailing-edge Flap (ATF) Blade for Helicopter Vibration Control 2013”, Seoul National University, Master’s Thesis, School of Mechanical and Aerospace Engineering, Seoul National University, Seoul, February 2013.
- [10] Kang, J.P., Eun, W.J., Lim, J.H., Visconti, U., Shin, S.J., “Design Improvement of Smart Active Trailing-edge Flap for Rotating Test”, 56th AIAA/ASCE/AHS/ASC Structures, Structural Dynamics and Materials Conference, Kissimmee, January 2015.
- [11] Mainz, H., van der Wall, B., Leconte, P., Ternoy, F., Mercier des Rochettes, H.,

“ABC Rotor Blades: Design, Manufacturing and Testing”, 31th European Rotorcraft Forum, Florence, September 2005

- [12] Li, L., Padthe, A.K., Friedmann, P.P., Quon, E., Smith, M.J., ”Unsteady Aerodynamics of an Airfoil/Flap Combination on a Helicopter Rotor Using Computational Fluid Dynamics and Approximate Methods”, 65th American Helicopter Society Annual Forum, Grapevine, Texas, May 2009.
- [13] Abbot, I. H., and Von Doenhoff, A. E., *Theory of Wing Sections*, Dover Publications, Inc., New York, 1959.
- [14] Standish, K.J., van Dam, C.P., “Aerodynamic Analysis of Blunt Trailing Edge Airfoils”, *Journal of Solar Energy Engineering*, November 2003.
- [15] Berkman, M.E., Sankar, L.N., Berezin, C.R., Torok, M.S., “Navier-Stokes/Full Potential/Free-Wake Method for Rotor Flows”, *Journal of Aircraft*, September-October 1997.
- [16] Lohner, R., “Finite Elements in CFD: What Lies Ahead”, *International Journal for Numerical Methods in Engineering*, September 1987.
- [17] Pearce, D.G., Stanley, S.A., Martin F.W., Gomez, R.J., Le Beau, G.J., Buning, P.G., Chan, W.M., Chiu, T., Wulf, A., Akdag, V., “Development of a Large Scale Chimera Grid System for the Space Shuttle Launch Vehicle”, 31th Aerospace Sciences Meeting & Exhibit, January 1993.
- [18] Tannehill, J.C., Anderson, D.A., Pletcher, R.H., “*Computational Fluid Mechanics and Heat Transfer*”, Hemisphere Publishing Corporation, 1984.
- [19] Spalart, P., Allmaras, S.R., “A One Equation Turbulence Model for Aerodynamic Flows”, 30th Aerospace Sciences Meeting & Exhibit, January 1992.
- [20] Mavriplis, D.J., “Revisiting the Least-Squares Procedure for Gradient Reconstruction on Unstructured Meshes”, *American Institute of Aeronautics and Astronautics*, 2003.
- [21] Patankar, S., “*Numerical Heat Transfer and Fluid Flow*”, , Hemisphere Publishing Corporation, 1980
- [22] Anonymous, Dymore Solutions, User’s manual.
- [23] Batina, J.T., “Unsteady Euler Algorithm with Unstructured Dynamic Mesh

for Complex-aircraft Aerodynamic Analysis”, American Institute of Aeronautics and Astronautics, 1990.

- [24] Dvorak, G., “Micromechanics of Composite Materials”, Springer Edition, 2002.
- [25] Press, W.H., Teukolsky, S.A., Vetterling, W.T., Flannery, B.P., “Numerical Recipes. The Art of Scientific Computing”, Cambridge University Press, 2007.
- [26] Kang, J.P., ‘Design Improvements of the Smart Active Trailing-edge Flap (ATF) for Rotating Test’, Seoul National University, Master’s Thesis, School of Mechanical and Aerospace Engineering, Seoul National University, Seoul, February 2015.
- [27] Chopra, I., “Recent Progress on the Development of a Smart Rotor System”, Adaptive Structures, Eleventh International Conference, Nagoya, 2000.

국문초록

본 논문은 회전익기의 로터에서 발생하는 진동 하중을 줄이기 위한 연구로 능동형 뒷전 플랩이 설치된 축소형 블레이드, SNUF (Seoul National University Flap) 제작을 위한 여러가지 해석 및 실험에 관한 것이다. 플랩은 압전재료로 제작된 작동기에 의해 구동되며 로터가 발생시키는 주요한 하중(primary disturbances)을 감소시키기 위하여 부차적인 진동을 발생시킨다. CFD 해석을 통하여 플랩의 힌지모멘트를 계산하였고 이를 통하여 목표하는 진동수와 각도로 선택한 작동기에 의해 플랩이 구동할 수 있는지 검증하였다. 작동기의 특성과 힌지모멘트를 비교하여 현재의 작동기로 플랩을 정상적으로 구동할 수 있음을 보일 수 있었다. 더 나아가, 다물체 동역학 해석프로그램인 DYMORE를 이용하여 블레이드에 공력과 원심력이 작용하였을 때 작동기의 힘과 변위의 관계를 반영하여 플랩의 구동 범위가 목표하는 범위를 만족하는지 해석하였다. 프로그램을 이용한 해석 외에도 이론에 의한 정식화 및 현재 시스템의 동역학적 해석을 이용한 검증을 수행하였다. 또한 플랩의 벤치테스트를 수행하여 플랩의 작동 방향의 수직인 방향으로 원심력이 작용할 때 플랩의 구동을 관찰하였다. 지금까지 하중을 아직 실제 작용하는 원심력까지 부과하지는 못했지만 원심력에 의한 하중이 증가함에 따라서 플랩의 작동 범위가 줄어드는 것을 관찰할 수 있었다. 하지만 이 줄어드는 정도는 적어서 목표하는 작동 범위를 만족하였다.

주요어: 지능형 능동 뒷전 플랩(ATF), 압전재료 작동기, 진동 제어, 지능형 로터 블레이드

학번 : 2014-22147